UNIVERSITY OF OKLAHOMA

GRADUATE COLLEGE

ADDITIVE MANUFACTURING AND SYNTHESIS OF ADVANCED ANTIBACTERIAL AND SENSING PHOTOCURABLE POLYMER NANOCOMPOSITES

A DISSERTATION

SUBMITTED TO THE GRADUATE FACULTY

in partial fulfillment of the requirements for the

Degree of

DOCTOR OF PHILOSOPHY

By

CHRISTOPHER BILLINGS
Norman, Oklahoma
2023

Downloaded from SHAREOK. Persistent Handle URL: https://hdl.handle.net/11244/338825

ADDITIVE MANUFACTURING AND SYNTHESIS OF ADVANCED ANTIBACTERIAL

AND SENSING PHOTOCURABLE POLYMER NANOCOMPOSITES

A DISSERTATION APPROVED FOR THE
SCHOOL OF AEROSPACE AND MECHANICAL ENGINEERING

BY THE COMMITTEE CONSISTING OF

Dr. Yingtao Liu, Chair

Dr. Mrinal C. Saha, Co-Chair

Dr. Jivtesh Garg

Dr. Shivakumar Raman

© Copyright by CHRISTOPHER BILLINGS 2023

All Rights Reserved.

DEDICATION

I would like to dedicate this dissertation to my family; my father, Rod, my mother, Angela, my brother Nicholas, and my fiancé Ashley. Without your constant support, encouragement, and belief in me, I would never have been able to achieve all of the goals and dreams I have set forth.

ACKNOWLEDGEMENTS

To begin, I would like to state my sincerest appreciation and gratitude to my mentor and professor, Dr. Yingtao Liu, for guiding me and pushing me to excel in everything I do. I have had an incredible opportunity to meet and work with a talented group of people while at the University of Oklahoma, which none of would be possible without Dr. Liu. You have strived to make each step of my journey possible and enjoyable while pushing me to be my best every step of the way. I also would like to acknowledge the great input and guidance provided to me by my academic committee. My Co-advisor Dr. Mrinal C. Saha, has provided excellent input over the years that have helped shape my research and drive me to really understand the finer details. I would also like to thank my other committee members, Dr. Jivtesh Garg and Dr. Shivakumar Raman, for their support and generous feedback. My research is only possible thanks to the support around me, and the team at OU has been foundational in ensuring that I can always work at the top level of what I am capable of. I would like to thank all of the team members that I have had the pleasure of working with through the years under Dr. Liu's guidance, including Blake Herren, Peter Sandell, Lane Taylor, Alene Basmadjian, and Benjamin Sherwood. You all have been a wonder to work with and made my time at OU fly by. I would like to thank Jimmy Cannon for providing guidance and insight over the years and always keeping me humble whenever I had another crazy idea. Lastly, I would like to thank my family for their unfaltering support and encouragement. Thank you, Ashley Chick, for always being there to push me and help me through the ups and downs. Thank you, Angela and Rod, for always checking up on me and ensuring that I could make graduate school my first priority, and thank you, Nicholas, for giving me time to laugh and for late-night conversations to keep me going.

TABLE OF CONTENTS

DEDICATION IV

ACKNOWLEDGEMENTS V

LIST OF FIGURES X

LIST OF TABLES XV

ABSTRACT XVI

CHAPTER 1: INTRODUCTION 1

1.1 Photocurable Nanocomposites 1

1.2 Antibacterial Nanoparticles 4

1.3 Use of Carbon Nanotubes in Resistive Sensors 7

1.4 Use of Carbon Nanotubes for Structural Reinforcement 9

1.5 Objectives and Scope of Work 10

CHAPTER 2: LOW-CONCENTRATION ANTIBACTERIAL NANOCOMPOSITES 12

2.1 Introduction 12

2.2 Manufacturing Methods and Materials 12

2.2.1 Nanocomposite Synthesis 13

2.3 Results and Discussion 19

2.3.1 Tensile Tests 19

2.3.2 Abrasion and Water Contact Testing 24

2.3.3 SEM Imaging 29

2.3.4 Proposed Applications 30

CHAPTER 3: HIGH-CONCENTRATION ZINC OXIDE ANTIBACTERIAL NANOCOMPOSITES 32

3.1 Introduction 32

3.2 Materials and Methods 32

3.3 Results and Discussion 37

3.3.1 Tensile Test Results 37

3.3.2 Water Contact Analysis 40

3.3.3 SEM Analysis 41

3.4 Conclusions 45

CHAPTER 4: HIGH-CONCENTRATION TITANIUM DIOXIDE ANTIBACTERIAL NANOCOMPOSITES 47

4.1 Introduction 47

4.2 Methods and Materials 48

4.3 Results and Discussion 52

4.3.1 Tensile Testing Results 52

4.3.2 Digital Image Correlation 55

4.3.3 Water Contact Angle 57

4.3.4 Glass Transition Temperature 58

4.3.5 Abrasion Resistance 59

4.3.6 High Magnification Imagery 61
4.4 Conclusions 65
CHAPTER 5: FLEXIBLE CNT NANOCOMPOSITES 66
5.1 Introduction 66
5.2 Materials and Methods 66
5.3 Results and Discussion 68
5.3.1 Tensile and Strain 69
5.3.2 Fatigue 70
5.3.3 Resistance Mapping 71
5.3.4 Viscosity 72
5.3.5 Glass Transition Temperature 74
5.3.6 High Magnification Imagery 76
5.4 Practical Applications 78
5.5 Conclusions 79
CHAPTER 6: STRUCTURAL REINFORCED CNT NANOCOMPOSITES 81
6.1 Introduction and Objectives 81
6.2 Methods and Materials 82
6.3 Results and Discussion 84
6.3.1 Manufacturing 84
6.3.2 Tensile Test Results 88

6.4 Conclusions 93

CHAPTER 7: FUTURE WORK AND CONCLUSIONS 94

7.1 Conclusions 94

7.1.1 AM Manufacturing of Antibacterial Photopolymers 94

7.1.2 CNT Reinforced Photopoymers 95

7.1.3 Key Parameters in Producing Mechanically Strong Parts 96

7.2 Future Work 99

APPENDIX – SUPPORTING INFORMATION 102

REFERENCES 114

LIST OF FIGURES

Figure 1: Manufacturing Process of Low-Concentration Antibacterial Nanocomposites 16

Figure 2: a.) Finished Printed Parts. b.) Inverted Manufacturing Process Utilizing an MSLA Printer. c.) Parts Being Prepared for Printing in Slicing Software with Supports 18

Figure 3: Young's Modulus and Ultimate Tensile Strength Bar Graphs Comparing the Resin Control and Nanocomposites 20

Figure 4: Young's Modulus and Ultimate Tensile Strength Bar Graphs Comparing the ABS Control and Nanocomposites. 21

Figure 5: (A.) Abrasion Testing Procedure for All Samples. (B.) Abrasion Testing Results Compared Across 5 Minutes of Abrasion. 24

Figure 6: (A.) Control Resin Water Contact Angles. (B.) TiO_2 Resin Nanocomposite Water Contact Angles (C.) ZnO Resin Nanocomposite Water Contact Angles (D.) Bar Graph of All Resin Water Contact Angles 26

Figure 7: (A.) Control ABS Water Contact Angles. (B.) TiO_2 ABS Nanocomposite Water Contact Angles (C.) ZnO ABS Nanocomposite Water Contact Angles (D.) Bar Graph of All ABS Water Contact Angles 27

Figure 8: Water Absorption Percentage Over Time. 28

Figure 9: (A.) SEM Imagery of TiO_2 Particles in A Resin Sample. (B.) SEM Imagery of ZnO Particles in A Resin Sample. 29

Figure 10: The Manufacturing Process for ZnO Nanocomposite Resin. 34

Figure 11: (A) Average Ultimate Tensile Stress with Error Bars Representing Standard Deviation. (B) Average Modulus with Error Bars Representing Standard Deviation. (C) Average Maximum Strain with Error Bars Representing Standard Deviation. 38

Figure 12: (A) Water Contact Angle of The Control Sample. (B) The Water Contact Angle of the 5% ZnO Sample 41
Figure 13: (A) SEM Backscatter Imagery Of 2.5% ZnO Sample. (B) Particle Analysis Using ImageJ Demonstrating Surface Agglomerations. 42
Figure 14: (A) SEM Backscatter Imagery Of 1% ZnO Sample with EDS Inspection Points at Markers. (B) EDS Analysis Of 5% ZnO Sample Validating Voids and ZnO Agglomerations. .. 43
Figure 15: (A) Optical Microscope Image of Fracture Point Of 7.5% Sample (B) Optical Microscope Image of Fracture Due to Voids On 7.5% Sample 44
Figure 16: The Manufacturing Process of TiO_2 Nanocomposite Tensile Samples..... 50
Figure 17: Elastic Region of All Samples. A.) Elastic Region of Control Samples. B.) Elastic Region Of 2.5% Concentration Samples. C.) Elastic Region Of 5% Samples. D.) Elastic Region Of 7.5% Of Samples 54
Figure 18: A.) Digital Image Correlation of Transverse Displacement Of 2.5% TiO_2 Sample. B.) Digital Image Correlation of Transverse Displacement Of 5% TiO_2 Sample. 56
Figure 19: a.) Control Water Contact Angle. b.) 2.5% TiO_2 Water Contact Angle. c.) 5% TiO_2 Water Contact Angle. d.) 7.5% TiO_2 Water Contact Angle 57
Figure 20: Glass Transition Temperature of Control Resin..... 59
Figure 21: Abrasion Comparison of Control and TiO_2 Samples 60
Figure 22: A.) SEM Image Of 5% TiO_2 Sample Using ETD Detector. B.) SEM Image Of 7.5% TiO_2 Using a Backscatter Detector. C.) Surface Topography Map Of 5% TiO_2 Sample. D.) Optical Microscope Image of Surface Features Of 5% TiO_2 Sample..... 61

Figure 23: a.) Tensile test results of ASTM D638 Type V samples with standard deviation plotted. b.) The maximum elongation of the sample before failure. c.) The Young's modulus of each sample 69
Figure 24: a.) Resistance of sample over time. b.) The stress of the sample over time c.) Stress-strain curve of a sample of all 250 cycles. 70
Figure 25: a.) Several cycles at 70% strain. b.) Raw data of resistance at multiple different strain values. c.) Smoothed data with local extrema automatically detected. 71
Figure 26: The viscosity of resin material as it is heated to printing temperature. 73
Figure 27: Normalized heat flow compared to temperature with glass transition temperature determined using a half-height midpoint calculation..... 75
Figure 28: a.) 2500x magnification of as printed surface with CNT dispersed throughout. b.) The 3D model generated of the sample demonstrating surface finish 76
Figure 29: a.) High magnification stitched image of CNT tear out across sample fracture. b.) 3D model of the sample fracture plane. 77
Figure 30: a.) Raw data from the resistance meter. b.) The Matlab modified data with key points automatically determined. c.)Finger under extension with a mounted sensor. d.) Finger under flexion with a mounted sensor. 78
Figure 31: Rate of cure of commercially available TR300 resin. 86
Figure 32: a.) 1 wt% samples with 60 seconds of in-situ pre- and post-curing. b.) 0.5 wt% samples with 60 seconds of in-situ cure pre-post curing. 87
Figure 33: 1 wt% samples with 180 seconds of in-situ pre- and post-curing. b.) 0.5 wt% samples with 180 seconds of in-situ cure pre-post curing. 88

Figure 34: Digital Image Correlation displaying strain across a 0.5 wt% ASTM D638 Type V sample. 92
Figure 35: a.) Cutaway of soft robotic finger system with internal cavities and dynamic wall thickness. b.) Full render of finished CNT embedded print. 100
Figure 36: A custom recoating system designed for MSLA and DLP printing systems for use with high-concentration nanoparticles. 101
Figure 37: Calibration Test of Virgin Resin on MSLA Printer 102
Figure 38: a.) Virgin translucent resin during batch printing on MSLA printer. b.) Zinc Oxide reinforced nanocomposite during batch printing on MSLA printer. 103
Figure 39: a.) Custom heated in-situ manufacturing enclosure system. b.) High-temperature underwater post-curing system. 104
Figure 40: a.) Custom machined fixturing for machining off bottom layers of samples. b.) CNC machining of the samples using custom toolpaths and flood coolant to negate any chipping or stress concentrations. 105
Figure 41: a.) Rate of cure testing apparatus with removable sample trays. b.) Live measurement of the reflected UV light and the temperature of the resin. 105
Figure 42: Run 1 of CNT Manufacturing Test. a.) Tensile test results of the specimens. b.) A stress strain curve of all three specimens. c.) Modulus of all specimens. d.) Amount of elongation or strain before break. 106
Figure 43: Run 2 of CNT Manufacturing Test. a.) Tensile test results of the specimens. b.) A stress strain curve of all three specimens. c.) Modulus of all specimens. d.) Amount of elongation or strain before break. 107

Figure 44: Run 3 of CNT Manufacturing Test. a.) Tensile test results of the specimens. b.) A stress strain curve of all three specimens. c.) Modulus of all specimens. d.) Amount of elongation or strain before break. 108
Figure 45: Run 4 of CNT Manufacturing Test. a.) Tensile test results of the specimens. b.) A stress strain curve of all three specimens. c.) Modulus of all specimens. d.) Amount of elongation or strain before break. 109
Figure 46: Run 5 of CNT Manufacturing Test. a.) Tensile test results of the specimens. b.) A stress strain curve of all three specimens. c.) Modulus of all specimens. d.) Amount of elongation or strain before break. 110
Figure 47: Run 6 of CNT Manufacturing Test. a.) Tensile test results of the specimens. b.) A stress strain curve of all three specimens. c.) Modulus of all specimens. d.) Amount of elongation or strain before break. 111
Figure 48: Run 7 of CNT Manufacturing Test. a.) Tensile test results of the specimens. b.) A stress strain curve of all three specimens. c.) Modulus of all specimens. d.) Amount of elongation or strain before break. 112
Figure 49: Run 8 of CNT Manufacturing Test. a.) Tensile test results of the specimens. b.) A stress strain curve of all three specimens. c.) Modulus of all specimens. d.) Amount of elongation or strain before break. 113

LIST OF TABLES

Table 1: Cure Settings for All Different Novel Nanocomposites 36

Table 2: Stress, Strain, And Modulus Data for All Samples, Including Standard Deviation 39

Table 3: Tensile Test Results for All Nanocomposites and Controls 52

Table 4: TR300 Mechanical and Thermal Properties 83

Table 5: Manufacturing specifications for each different nanocomposite sample set 83

Table 6: Average mechanical characteristics of each run 89

ABSTRACT

This work covers the synthesis, manufacturing techniques, and characterization of several novel nanocomposites produced with direct light processing-based additive manufacturing systems. Custom thermodynamic and UV control systems are implemented for photocurable resin systems to synthesize and manufacture up to 14 novel nanocomposites. These novel nanocomposites are synthesized to improve tensile strength, wear resistance, water contact angle, antibacterial resistance, and heat dispersion. Low-cost market-available printing systems are utilized with custom-designed enclosures and monitoring devices to allow printing with novel nanocomposites. This research discusses the advanced properties offered by each nanocomposite utilizing titanium dioxide and zinc oxide in weight concentrations as high as 7.5%. Carbon nanotubes (CNT) are also utilized in weight concentrations of up to 1%. A total of 5 different base resins are tested to demonstrate the effect of different oligomers and monomers on creating a matrix suited for nanocomposite addition. Secondary functions such as strain sensing are evaluated for human motion detection utilizing custom printed sensors, and ultimate tensile strength increases of over 200% are observed. The base matrix strength is improved with CNT concentrations as low as 0.5%. Wear resistance is documented to improve by over 15% in titanium dioxide and zinc oxide samples at 7.5% weight concentrations. Optimization studies are performed to determine the cure rate and in situ curing characteristics' effect on final part strength for CNT nanocomposites. Lastly, CNT alignment is explored through modification of printing parameters and resin viscosity curves to aid in part strength. This work demonstrates the ability to manufacture nanocomposite-reinforced parts that exhibit significantly improved physical, thermal, electrical, and antibacterial properties at high fidelity on low-cost hardware ideal for the medical, automotive, and aerospace sectors.

CHAPTER 1: INTRODUCTION

1.1 Photocurable Nanocomposites

Additive manufacturing (AM) has played a significant role in polymer and composite manufacturing for broad biomedical and public health applications in recent years[1-4]. Due to the broad array of AM manufacturing techniques, such as fused deposition modeling and direct ink writing, traditional biocompatible polymers and composites can be rapidly converted into novel devices and products to enhance medical treatment and public health[5]. Additionally, integrating AM technologies with novel polymers and nanomaterials with beneficial functionalities has opened new directions for developing cutting-edge devices, sensors, and tools that may revolutionize medical treatment and prevent infectious diseases.

Photocurable-based AM is a unique manufacturing option due to the high product quality and low processing temperature. These AM systems are usually referred to as stereolithography (SLA) and digital light processing (DLP) and use an ultraviolet light source to cure photopolymers layer by layer with high spatial resolution and surface quality[6, 7]. This feature allows photopolymerization-based AM systems to create parts with almost perfect microstructures, which is rare for other AM processes, such as fused deposition modeling. In addition, the build plate is the only moving part in these machines traveling in the Z direction. This mechanically simple design allows for precise process control and optimization during AM for various photocurable polymers and nanoparticle-reinforced composites.

This research focuses on utilizing stereolithography technology with novel nanocomposites to produce enhanced composites applicable to the medical field. Extensive research has been conducted utilizing SLA-based manufacturing to prove its effectiveness in the medical field[8-10]. Most prominently is its use in the dental industry to create items such as

retainers and dentures[8]. While these systems allow researchers and doctors to utilize the advantage of one-off manufacturing, they often use materials that suffer from other disadvantages. A solution proposed for this problem is to create a nanocomposite resin that can be manufactured in off-the-shelf systems that offers improved characteristics for the end use case. Specifically, looking into chemical advantages such as antibacterial properties would greatly increase the value proposition for these technologies. A nanoparticle that has been studied to offer these properties is titanium dioxide.

Stereolithography (SLA) based manufacturing is capable through several techniques, including laser, LCD blocking, and direct light projection. These technologies offer different advantages, such as plane resolution, cost, output power, and printing speed. Nanocomposite fabrication has been proven possible using these technologies to produce significantly stronger parts[11, 12]. There is well-documented research using nanoparticles, such as carbon nanotubes (CNT), silicon dioxide, and carbon black[11, 13, 14]. A masked LCD-based printer was utilized as it offered a low entry cost along with open-source hardware.

Additionally, it provides very fast printing compared to other technologies, such as laser-based systems, as it can cure an entire layer simultaneously. While these masked stereolithography (MSLA) printers do not offer the same trueness as commercial-grade SLA printers, they do not suffer from decreased precision with changes in layer height and still fall within many medical threshold values[9, 10]. Multiple studies have used low-cost MSLA printers to prototype functional composites and microfluidic chips[15, 16].

Composites have been successfully produced utilizing AM techniques, including fused deposition modeling, direct ink writing, selective laser sintering, direct ink writing, and stereolithography (SLA)[17-20]. SLA-based manufacturing produces high-resolution parts capable

of withstanding various environmental factors due to its photopolymerization process, where the chemicals crosslink to produce the final part[21]. These benefits create a strong case for experimenting with high-resolution nanocomposites that offer beneficial functionality. The nature of photopolymerization does not require high temperatures compared to other AM processes and, therefore, allows for a wider variety of reinforcements. Additionally, the resolution of this manufacturing process is often under 25 microns[21]. This high resolution, paired with a wide range of compatible fillers, creates an ideal environment for producing medical prototypes, geometry-restricted parts, and parts with opacity requirements that cannot be traditionally manufactured.

The process of manufacturing composites often entails a high-cost and time-intensive process, reducing its applicability to widespread industry adoption[22]. However, a solution to these issues has presented itself in recent years with the advent of nanoparticle composite manufacturing in processes such as injection molding. These processes utilize nanoparticles' mechanical advantages to create isotropic composites when manufactured under different conditions[23]. Similarly, AM has introduced other composite fillers within its realm of production to improve part characteristics.

Production of composites in AM is limited to very few specialty machines. It has been well-accepted that one of the best ways to incorporate composites into AM is by introducing composite resins[24]. The primary benefit of this composite type is that it often requires little to no modification of the printing system. Additionally, the use of resins allows for printing at high resolutions to rival the quality of traditional manufacturing. The disadvantage is that many resins suffer from limited mechanical performance and are produced at high viscosity, making it

challenging to introduce a fiber composite into the matrix[2]. Currently, researchers are working to help develop smart materials and characterize novel resins to solve this gap[25].

1.2 Antibacterial Nanoparticles

Through independent research studies, zinc oxide (ZnO) and titanium oxide (TiO_2) have been proven to prevent bacteria growth in E. coli colonies and even show promising results in killing the COVID-19 virus[3-5]. Extensive research has also been completed regarding antibacterial properties' effectiveness based on nanoparticle size. These studies concluded that the smaller the particle size, the greater effectiveness at stunting bacteria growth[6, 8]. Because of this, two different nanoparticles were used in this study to demonstrate the differences in composite properties. Both particles are on the smaller range of available nanocomposites, so they should be best effective against today's bacterial threats. The antibacterial properties of these nanoparticles have also been shown to be most effective when exposed to light[26]. Translucent base resins were used to help transmit light to the particles on all surfaces and internal cavities.

To maximize the applications of this high-resolution AM technology, it is critical to add a reinforcement that offers beneficial functions. Zinc oxide nanoparticles have been widely applied due to their controllable nanostructures, morphology, synthesis methods, and even antibacterial properties[27-31]. Extensive research has been performed on the antibacterial effects of ZnO as nanoparticle sizing changes[32]. These studies have focused on the effect of nanoparticle size on antibacterial effectiveness, demonstrating that a decrease in particle size leads to an increase in anti-bacterial activity[6, 7, 33, 34]. These studies help guide future use of the material and highlight the importance of proper dispersion of ZnO when being implemented for its antibacterial properties.

Previous work with these nanoparticles has shown that TiO_2 has been used in nanocomposite structures successfully and was a strong candidate for resin printing[35]. These materials have also proven to be explicitly biosafe when exposed to UV light which is used as the curing agent[36, 37]. In addition, nanofilms have been used in the medical field to prevent bacteria buildup on different medical tools [38, 39]. These previous findings reinforce the research on medical applications of 3D-printed nanocomposites.

The antibacterial properties have been well documented, and research has shown that it is effective against many items, such as the SARS-CoV-2 virus[3]. The ZnO used in many of these studies also demonstrated a positive correlation between UV light exposure and antibacterial performance[36]. These results provide a foundation for utilizing the ZnO as a filler in a UV-activated photopolymer, as the ZnO should not be harmed in the manufacturing process.

A concern when utilizing ZnO in a photocurable resin is the UV absorbance characteristics of the material. Research has shown that ZnO is naturally UV absorbent and increasingly absorbent at 15-40 nm[40, 41]. This creates a problem when compounded with the antibacterial effectiveness increasing as particle size decreases. When ZnO was introduced into other thermosets, such as epoxy nanocomposites, studies found that it had an adverse effect on cure time and overall cure strength[42]. Properly adjusting post-curing time and in-process cure time will be required to overcome the UV absorption caused by the ZnO. Studies done on control resins have demonstrated that the post-curing of the material has a significant effect on the strength but does not affect the middle layers, and therefore attention to the in-process curing will be critical[43].

With the production of antibacterial parts, it will be important to characterize the wettability properly. Parts that harbor moisture will lead to more significant issues relating to

bacterial growth, so a low wettability would be desired. As the novel nanocomposite will functionally always have a ZnO coating, the surface energy of the ZnO will play a prominent role in the final part's wettability. Studies performed on ZnO's wettability have shown that it can be highly hydrophobic under the correct conditions[44, 45]. Therefore, integrating and activating the ZnO through UV exposure will be essential to achieve the desired characteristics.

Increasing the strength of a composite will often increase the material's wear resistance. A study on the wear resistance of resin printing found that it was similar to the bulk materials obtained during traditional manufacturing, so any improvements would be advantageous [46]. Previous work on this topic with several different matrix materials demonstrated an increase in wear resistance when ZnO nanoparticles were introduced at concentrations of 1%[16]. However, these results rely heavily on reducing voids in the final printed part.

Titanium dioxide is chosen as the filler material as it offers several advantages, including increased strength, antibacterial properties, and improved surface properties[5, 8, 26, 47, 48]. The nanoparticle is also easy to source, low-cost, and widely used in industry. As a result, TiO_2 can be found in many commercial products, such as sunscreens, food, and beauty products[49-51]. Along with these attributes, TiO_2 nanoparticles are spherical, reducing many issues associated with the dispersion and mixing of low-viscosity nanocomposites.

When creating a nanocomposite for MSLA-based manufacturing, many considerations include final viscosity, shear strength, rate of cure, and ultraviolet (UV) absorbance. Research conducted on the UV absorbance of TiO_2 has documented its ability to create an oxidative effect[52]. Research has also demonstrated that the effectiveness of TiO_2 as an antibacterial agent increases when exposed to light in the ultraviolet spectrum[53]. However, while its effectiveness increases with exposure to UV light, it also acts as a UV blocker which causes manufacturing

concerns[49, 54]. As the manufacturing process is based on UV-curable resin properly hardening at each layer, the UV-blocking properties could cause issues with higher concentrations of nanoparticle loading. Successful studies have incorporated TiO_2 into UV-curable medical resins at extremely low concentrations[8].

1.3 Use of Carbon Nanotubes in Resistive Sensors

The utilization of AM to fabricate advanced replacement parts and solutions for the medical, aerospace, and automotive industries has allowed for more functional designs and improved final solutions. However, the main barriers to entry over the last several decades have been the high entry cost, low part resolution, and limited material properties and functions. The advent of entry-level manufacturing solutions to this space has allowed for the more widespread adoption of these technologies, but the other two barriers often still exist. To combat these barriers, researchers are working to find solutions to these issues through various avenues, including novel composites, unique manufacturing techniques, and custom software solutions[16, 55, 56].

Photocurable thermoset manufacturing allows for increased part resolution compared to other AM processes and therefore is a strong candidate for the medical field. Additionally, research groups have utilized medical grade and biocompatible resins as base matrix materials to synthesize novel nanocomposites for the medical field [57-59]. Previous research has demonstrated the ability to add antibacterial functional properties to base photocurable resin matrices through nanoparticles in low-weight concentrations[16, 60]. These studies aimed to maximize the material's physical strength through nanoparticle addition while increasing bacteria resistance using TiO_2 and ZnO nanoparticles. However, the disadvantage to this approach was that the large

nanoparticle density and low aspect ratio limited the strength of the final composite compared to other nanoparticles, such as CNT.

The utilization of CNTs in thermoset composites is well documented in research as they offer improved mechanical and electrical properties[61-64]. The use of CNTs in the dental industry has improved mechanical properties and met medical requirements[65]. Additionally, they have demonstrated the ability to produce flexible strain sensors when paired with a flexible matrix in a traditional thermoset[66-69]. However, studies have also demonstrated the ability to utilize CNTs in photocurable thermosets in AM-based processes [70-73]. Other nanoparticles have also demonstrated the ability to exhibit a piezoelectric response when added to a thermoset such as copper, silver, carbon, and polyvinylidene fluoride[74-76]. These nanoparticles were not selected as they did not offer the increased durability and toughness expected from CNTs.

Using photocurable matrix materials allows for intricate part design but introduces several challenges, including the degree of cure, part strength, manufacturing conditions, and post-processing concerns. Variables such as post-curing temperature control and time can have a significant impact on a part's final strength and function [77, 78]. The degree of cure is largely dependent on in-situ curing settings and temperature, where increased chamber temp has been shown to increase green part mechanical properties due to a higher degree of cure[79]. These variables create a complex manufacturing environment that must be replicated for repeatable results.

The final requirement for repeatable specimen manufacturing is consistent CNT dispersion in the given matrix material. Different mixing methods exist, such as sonication, planetary, and microfluidizers. Using planetary shear mixing and microfluidizer in tandem allows for ideal dispersion compared to other pairings or mixing methods[80]. Other studies have

also demonstrated that pairing planetary shear mixing with in-situ polymerization leads to improved CNT dispersion compared to traditional methods[81]. Lastly, non-destructive evaluation techniques studying the thermal properties of CNT nanocomposites have proven that mixing in a planetary shear mixer has led to improved results[82]. These findings aided the decision to utilize a planetary shear mixer as the nanocomposite synthesis tool of choice.

1.4 Use of Carbon Nanotubes for Structural Reinforcement

Carbon nanotubes offer one of the best strength-to-weight ratios in the nanocomposite world. Proper bonding with a polymer matrix can increase the new nanocomposite strength to 16 times stronger than the original material[83]. A large part of the ability of a CNT to reinforce a polymer matrix is its ability to bond with the matrix material. This often comes down to the interface layer between the CNT and matrix. This often limits the amount of CNTs that can be added before the new nanocomposite starts to deteriorate in strength instead of strength. One study has found that this limit is around 2% CNT by weight for textile-based composites [84].

To help aid in this issue of CNT bonding, research groups often functionalize the CNTs with different materials[85]. Another research group has determined that using solvents often negatively affects the material's interfacial layer, decreasing part strength[86]. Often solvents are utilized to help disperse the CNTs in a higher-viscosity material such as PDMS. As the resins used for this work have a much lower viscosity, it would be beneficial to disperse the CNT directly into the solvent to reduce possible interfacial layer bonding issues.

As the chemical makeup of the resin will not be modified during this phase of testing, keeping the viscosity of the material within a usable range will be required. One study has successfully utilized CNT concentrations of 0.5 wt% [87]. This study also analyzes the cure rate

and notes that it has a linear relationship with the CNT concentration. Not only does the rate of cure of the material decrease with the addition of CNT, but the maximum layer thickness also decreases due to the UV absorbance of the CNT. The addition of CNT in concentrations as low as 0.5 wt% can lower the maximum curing thickness of a photopolymer by as much as 10x going from 1000 microns to just under 100 microns[88].

These conditions create several challenges to utilizing CNT as a filler material for a photocurable matrix as it directly counteracts the mechanism utilized in curing the matrix material. The solution to these obstacles often includes greatly increasing cure times and raising temperatures during curing. CNTs also act as thermal conductors, so they more effectively transfer thermal energy during exothermic curing. Not only does this aid in more even thermal stability during the curing process, but it also often increases the final part's thermal properties. One study found up to a 10° C increase in glass transition temperatures with concentrations as low as 0.75 wt% of CNTs [89].

1.5 Objectives and Scope of Work

The work portrayed in this dissertation aims to aid in the knowledge of high-speed AM of photocurable nanocomposites. A total of 14 different novel nanocomposites are discussed in this report, with each designed to help solve a problem through the addition of functions through nanoparticles. Where applicable, these nanocomposites' synthesis, manufacturing, and testing will be documented, including their mechanical, thermal, and electrical properties. The first portion of this work focuses on utilizing antibacterial nanoparticles of TiO_2 and ZnO to reinforce photocurable resins while providing antibacterial functions. Manufacturability utilizing commercial printers is focused on along with the synthesis and curing conditions of each proposed nanocomposite. The second portion of this work utilizes CNTs to produce flexible

conductive sensors and mechanically improved thermosets. The flexible sensors are characterized by maximum strain, electrical conductance, and thermal resistance. A novel application is designed for human motion detection utilizing this nanocomposite. Lastly, a series of experiments is designed to aid in optimizing the manufacturing of CNT-reinforced photocurable nanocomposites by studying key manufacturing characteristics deemed critical to strong mechanical results. These tests resulted in the proposed nanocomposite being 225% stronger than the base matrix material.

The four main objectives of this research are as follows:

I Determine how to quickly synthesize nanocomposites out of commercially available photocurable resins.

II Investigate the ability to introduce antibacterial nanoparticles into a photocurable matrix manufactured on commercially available machines.

III Characterize the key components in photocurable AM manufacturing that affect the mechanical properties of the final part.

IV Apply the above results to manufacture advanced CNT nanocomposites with strain gauge response and greatly increased mechanical results.

CHAPTER 2: LOW-CONCENTRATION ANTIBACTERIAL NANOCOMPOSITES

2.1 Introduction

This study aims to utilize commercially available equipment and photocurable resins to manufacture low-concentration novel antibacterial AM parts. Photocurable resin materials have often been used coating-based utilizing additives to provide additional functions [90-92]. These coatings have offered improved benefits such as hydrophobicity and UV resistance to the base material. Utilizing these nanoparticles and resins as a nanocomposite that can be completely additively manufactured would retain a base part demonstrating these properties throughout its entire service life.

The barrier to entry of AM has been reduced in recent years as the cost of entry has lowered to less than $500 for an entire manufacturing setup. This study's printer and post-processing equipment are at the lowest end of the spectrum and will be a strong proving point for future studies. This work will help characterize two different matrix materials and antibacterial additives when used at low wt% concentrations. It will study the materials' interactions and any effects on mechanical strength. A small study on surface alterations will also be conducted. To finalize, SEM imagery will be conducted to determine the dispersion and study the interphase layer of the materials.

2.2 Manufacturing Methods and Materials

The printer for this study was an Anycubic Photon with a build volume of 115mm x 65mm x 155mm. This printer has a xy-plane resolution of 47μ and a z-axis resolution of 25μ. The printer utilizes a color LCD panel to mask off LEDs emitting light in the 405nm wavelength.

This printer output 0.658 mW/cm^2 of energy throughout the entire build surface. No physical modifications to the printer were made. Elegoo Mars produced the two used resins: a standard LCD UV-curing photopolymer rapid resin and an ABS-Like LCD UV-curing photopolymer rapid resin. The two nanoparticles selected were TiO_2 and ZnO from Sky Spring Nanomaterials in the 10-30 nm range. An Instron 5969 was used with a 5kN load cell for tensile testing. Abrasion tests were completed using a Struers LaboPol-5 with a LaboForce-3 head attachment. A grinding disc with an aluminum oxide abrasive sized at 50μ, or a 240-grit pad, was used as the grinding medium.

2.2.1 Nanocomposite Synthesis

To synthesize the nanocomposite resin, several steps were followed to help increase printability. Initially, the ability of the nanocomposite to cure required testing as the addition of a non-curable agent leads to reduced bonding and light transmission throughout the print. The virgin materials were transparent and therefore allowed complete UV penetration for the entirety of the layer. Adding the nanoparticles reduced the material's opacity requiring a modification in the printing settings. The software for preparing prints, Chitubox, allowed modification of all printing steps. The criteria used to determine successful prints included the ability for the print to reliably adhere to the build plate and for the printer to have a minimal loss in part resolution. Additional criteria included reasonable manufacturing time, consistent cure times for each layer, and no requirement for external heating. The addition of the nanoparticle to the resin created two issues. The first issue was that as the nanoparticle percentage increased, the viscosity of the novel composite also increased. This directly affects the printer's ability to reset between layers, allowing for even nanoparticle dispersion. The second issue was that as the nanoparticle percentage increased, the ability of the printer to cure each layer adequately decreased. The

modified parameters were the number of initial layers, the initial layer cure time, the remaining layer cure time, and the initial Z distance. The first issue was addressed using different concentrations of nanoparticles to test for proper return flow into the recess created due to the curing part. This is directly related to the material's viscosity and the nanoparticle's effect on viscosity at different weight concentrations. As the printer finishes a layer, the build plate rises above, releasing the part from the fluorinated ethylene propylene (FEP) sheet to allow the new resin to flow into the recess. The time could be adjusted through software but was left constant to keep print times at a reasonable speed. This mandated that the novel resin retain similar viscosity values to the virgin material for initial testing. Increasing this time would also create issues with particle settlement. Results showed that concentrations up to 5% could adequately fill the void in the time provided. Concentrations above 5%wt lead to a substantial increase in viscosity and reductions in transparency. To address the second issue of the reduced bonding between the resin and the build plate, the initial z height was decreased to create a thinner composite layer between the FEP sheet and the aluminum build plate. This helped ensure the resin was forced into the build plate's micro-abrasions, increasing build plate adhesion. This also reduced the amount of resin that required curing on the first layer.

Along with this change, the initial layer curing time was doubled from 60 seconds to 120 seconds. An increased cure time would help improve the consistency of the cure across the layers. A total of 5 bottom layers were used for the prints. Lastly, the cure time for the remaining layers was increased from 8 seconds to 15 seconds. With these settings in place, varying concentrations of nanoparticles were added to the composite for testing. Adequate bonding and detail retention were easily held at a 1% nanoparticle addition. At around 2.5% addition, failed prints began to arise due to a failure in bonding the first layer. The failure in bonding was due to

the decreased amount of resin and build plate interface, as the nanoparticle now accounted for a significant portion of the surface area of the new part.

Different mixing methods were employed to introduce the nanoparticles to the matrix resins. First was a process of hand mixing the two components for five minutes with a stir rod. The second was to shake the mixture in a closed bottle until no visible particles could be identified. The last method was to use a stirring plate. Hand mixing was an effective procedure but required careful inspection of the mixture as it was poured into the printer to ensure it was homogenous without clumping formation. Filters with pore diameters of less than 1 mm could be employed to help ensure no large particles are introduced into the printing vat, leading to print failures. The second method provided greater homogeneity throughout the mixture due to the forces involved in the mixing process and the ability to change the direction of the fluid flow within the mixing chamber. The last method provided similar results to the first, as the stirring plate would often have difficulty mixing the resin at speeds above 100 rpm due to the high viscosity of the mixture. The resins mixed in the enclosed bottle also showed less particle settlement. A proper mixture would suspend particles for up to 6 hours of printing without needing to be remixed. Therefore, an enclosed centrifugal mixer is the best machine for synthesizing the nanocomposite resin. The entire manufacturing process for the resin and part is depicted in Figure 1.

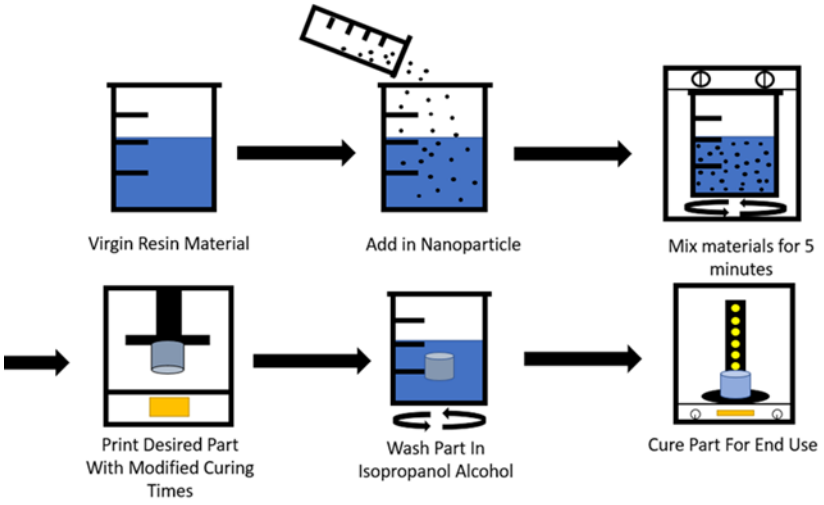


Figure 1: Manufacturing Process of Low-Concentration Antibacterial Nanocomposites

Other essential concerns with using a non-homogenous nanocomposite included particle settlement over time. As the only motion during the print was the build plate repeatedly raising and lowering, the nanoparticles would begin to settle over time as their density was higher than that of the resin matrix. This issue was most noticeable at higher particle concentrations and would cause layer adhesion issues during the print as the particles settled and increased the relative concentration at that layer. There were several approaches used to remedy this issue. The first approach was to start with a minimal amount of nanoparticle addition, as previously discussed, as this would help ensure proper distribution throughout the matrix material. The second and more proactive step was to pause the print on the hour and remix the composite by hand. This was done in the printer with a plastic scraper so as not to damage the FEP sheet. Finally, removing the resin vat could cause alignment issues with the printer, and therefore the mixing was performed inside the vat with the build plate raised to the maximum Z height.

After removal from the build plate, all parts were put into an isopropyl alcohol bath on a stirring plate for a minimum of six minutes. This allowed the isopropyl alcohol to dissolve any remaining uncured resin on the parts, which is critical to retaining high part resolution during the final stage. After thoroughly cleaning, the part was put into a UV chamber for at least 4 minutes. Again, time was added based on the appearance of the part until a flat matte sheen was achieved.

To demonstrate the 3D printability of the novel nanocomposite, several complex parts were printed and assembled. As shown in Figure 37, a calibration print was printed to ensure the printer was performing as expected. The first of the three primary tests consisted of a chess rook with intricate detail to observe the nanocomposite resin's ability to maintain surface details and internal geometries within a single part. Secondly, a large pipe fitting was printed to successfully show the material's ability to be used in fluid flow systems. Lastly, a prosthetic finger was printed to illustrate a biomedical application directly. All these parts can be seen in Figure 2. Along with these prints, over 30 tensile test specimens were printed.

The pipe fitting was printed to showcase the part's ability to be used in a fluid flow system. As discussed later, the low water absorption of these novel resins over time allows for part adaptation into fluid environments where antibacterial properties are beneficial. Many parts of the healthcare industry are often in contact with different types of fluids and must be meticulously cleaned as a moist environment breeds bacteria. The fittings successfully printed here showcase the ability to produce complex part geometries that would help lead to less turbulent flow within a system. This would be incredibly beneficial when working with fluid systems where turbulent flow that traps air bubbles is undesirable. Additionally, the nature of the material would lead to fewer concerns for contamination and longer implementation cycles before cleaning or replacement. As these parts can be produced in mere hours for a fraction of

the cost of most medical equipment, the viability of this technology in medical environments increases.

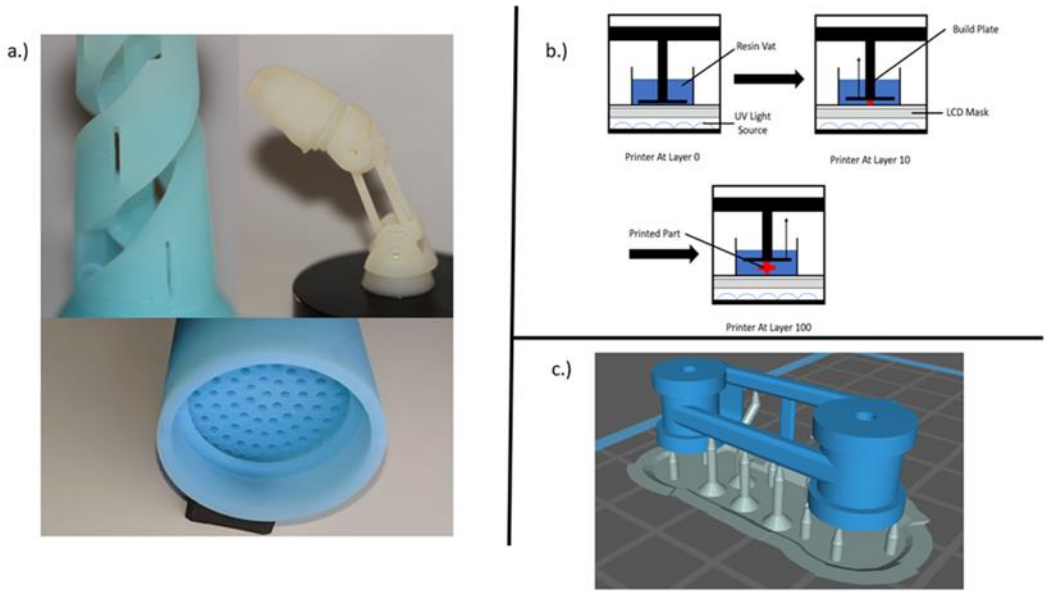


Figure 2: a.) Finished Printed Parts. b.) Inverted Manufacturing Process Utilizing an MSLA Printer. c.) Parts Being Prepared for Printing in Slicing Software with Supports

Lastly, a working prosthetic finger designed by Danger Creations was printed to show the opportunities this technology provides. The part has many intricate details and moving parts that perfectly interface together. The prosthetic finger can be manufactured in under 2 hours. This technology allows for weight optimization of medical apparatuses, which is impossible with other manufacturing techniques. Since weight is a critical factor in user experience and comfort, customizable options like these are consumer-oriented. Because the novel nanocomposite was developed explicitly for use in digital light processing machines, the design freedom given to medical engineers is greatly expanded. In addition, the material cost for this finger was just 18 cents for the nanoparticles and resin material. Given a uniform dispersion, a low concentration of

nanoparticles leads to a low-cost nanocomposite. Pairing a low-cost nanocomposite with AM technology provides the best solution for corporations needing intricate one-off parts. Due to eliminating expensive machinery and custom molding, this technology offers an unparalleled cost advantage for the healthcare industry. This drastic reduction in cost and manufacturing time will revolutionize the medical industry if implemented on a per-hospital level, all while delivering better care.

2.3 Results and Discussion

Tensile testing was performed using the ASTM D638 bar type IV standard to verify uniformity between prints and the effect of the nanoparticle on the physical characteristics of the base resin materials. The specimens were 70 mm long, maximizing the available build plate area. In addition, this was done to highlight lower tensile stress values if there were nonuniformity throughout the material. This required multiple prints for each data set, and therefore, the standard deviation is likely present due to an unoptimized mixing procedure during this testing.

2.3.1 Tensile Tests

The first data set analyzed was the difference in the tensile strength of the ABS-like and control resin. Testing showed that both materials performed similarly, with the base resin just edging out the ABS-like material in terms of tensile stress by 1.42 MPa. This equates to just a 6.8% increase in tensile strength for the base resin. Regarding strain, both materials showed nearly identical maximum strain values of 0.075. The main difference between the two resins is that the standard deviation for the ABS-like photopolymer was lower at a value of 1.636 MPa compared to the base resin standard deviation of 2.856 MPa. This increase in deviation is likely the cause for the slightly higher average tensile stress seen in the resin samples.

At a 1% addition of nanoparticles by weight, the base resin demonstrated a significant increase in tensile strength and Young's Modulus over the control. Both the ZnO and TiO_2 had a positive effect on the material's physical tensile strength. The ZnO led to an average tensile stress of 33.696 MPa, and the TiO_2 led to an average tensile stress of 29.533 MPa. Along with this, the average maximum strain reduced significantly in both samples. Up to an 88% increase in modulus was observed for the ZnO specimens, as depicted in Figure 3. The ZnO sample was reduced to a maximum strain value of 0.036, and the TiO_2 sample was reduced to 0.026. Thus, the base resin material was a strong candidate for a nanocomposite matrix as the tensile strength increased by 42.2% and the maximum strain reduced by at least 50%.

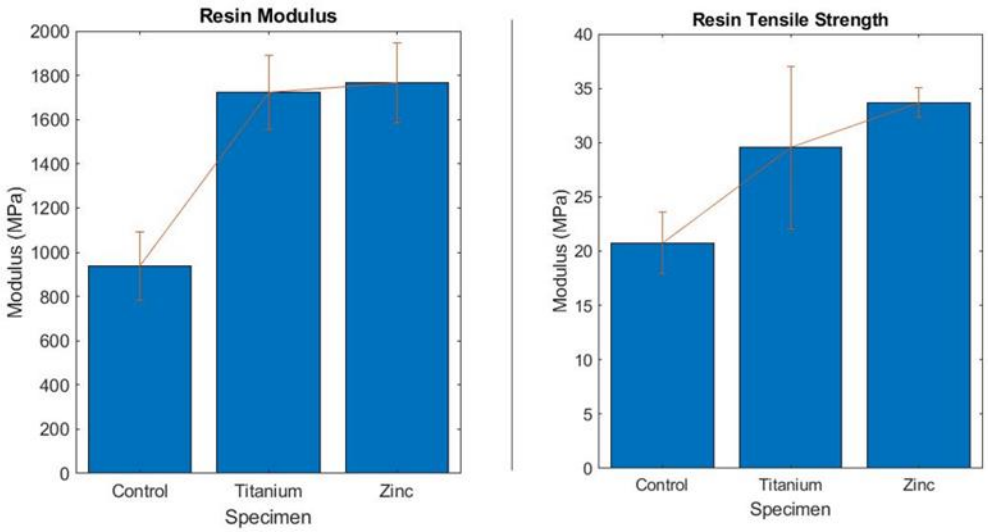


Figure 3: Young's Modulus and Ultimate Tensile Strength Bar Graphs Comparing the Resin Control and Nanocomposites

The control base resin was completely translucent in color and therefore was a prime candidate for nanoparticle addition. The manufacturer's lack of additives ensured that maximum light transmittance when adding nanoparticle additives could be achieved. Many manufacturers

rate translucent resins as a slower curing resin as they take longer to absorb UV light than their colored counterparts. The added nanoparticles in this study acted as a base resin colorant, leading to favorable results when analyzing cure parameters.

The ABS-like resin showed a negative correlation with the addition of nanoparticles. Both the ZnO and TiO_2 decreased the tensile strength of the specimens, as depicted in Figure 4. The ZnO led to a 15.1% decrease in tensile strength, while the TiO_2 led to a 12.98% decrease. The modulus was reduced by 1.7% for the titanium samples and 4.4% for the zinc. The maximum strain reduction was only 41% for the ZnO and 42% for the TiO_2. One improvement of the novel nanocomposite is reducing the standard deviation of between 1.03 MPa to 0.81 MPa compared to the ABS-like resin.

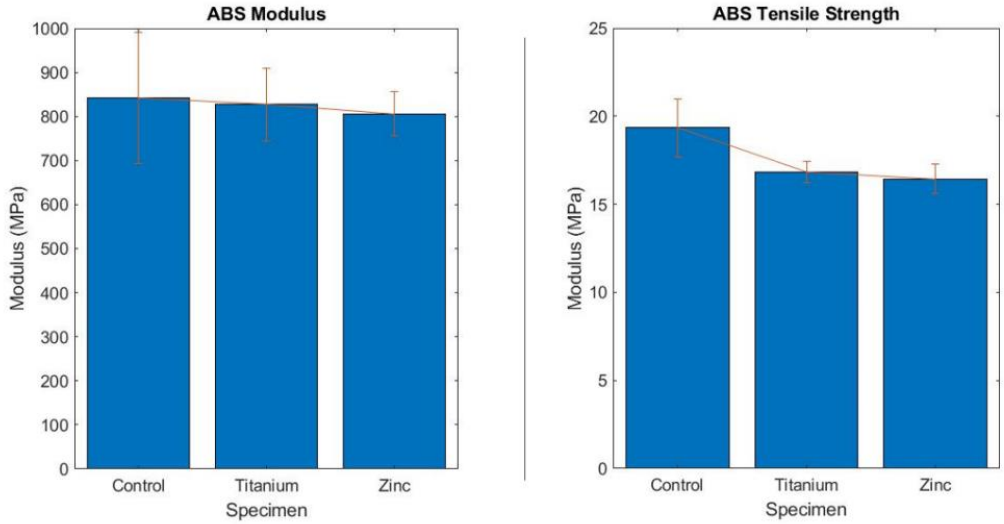


Figure 4: Young's Modulus and Ultimate Tensile Strength Bar Graphs Comparing the ABS Control and Nanocomposites.

Unlike the base resin, the ABS-like resin had a colorant or additive applied by the manufacturer, making the material less translucent and opaque. While the material should have

been well suited for nanoparticle addition at low concentrations, this additive appears to have negatively impacted the material's ability to bond with the selected nanoparticles. As these additives are intended to reduce the modulus of the material, it is believed that the material is now deforming around the nanoparticles during high tensile loading.

Tensile testing results have shown two interesting critical differences between the novel nanocomposites. The first noticeable data point is the similarities between the factory resin materials when looking solely at tensile strength. The average tensile strength between the two materials differed by only 7%. Along with this, the maximum strain before failure differed by only 0.27%. The standard deviation for the base resin was noticeably higher at a value of 2.856, leading to a 95% statistical confidence interval that both samples' mean tensile stress values are within the same range. This data shows that both factory materials are physically no different when applying a tensile force and analyzing ultimate tensile strength.

The addition of the nanoparticles to both matrix resin materials is where the data started to differ drastically. The nanocomposite addition reduced the properties of the ABS-like photopolymer in every test performed, whereas it improved the properties in every test for the resin material. The only exception to this was the water contact angle. As seen in the tensile test in Figure 18, the lower physical properties were not caused by anomalies during the printing process, as each part failed at similar yield strengths. In addition, the lowest standard deviation of all sample tests was in both ABS nanocomposite resins. This leads to the inference that the ABS-like resin's chemical makeup was not a strong candidate for nanoparticle addition. The probable cause is that during the curing process, the adhesion of the ABS-like resin and the nanoparticle was less than ideal. The lower results could be a side effect of micro-fractures caused by an incomplete bond between the nanoparticle and matrix. The only test where the nanoparticle

addition had a minimal effect was within the ZnO ABS nanocomposite abrasion sample. The reduction in abrasion was within the margin of error for having the same properties as the factory ABS-like matrix. The ZnO ABS nanocomposite did not follow a linear abrasion profile like all other samples. There were points during the testing where substantially more or less material was removed. This means that the mixture of the two materials throughout the test pieces was not perfectly homogenous and varied based on layer depth. There could be several reasons for this phenomenon: particle settlement, clumping, and uneven disruption of the mixture from the build plate. The TiO_2 ABS-like nanocomposite did not follow this same path and performed far worse than the factory ABS-like resin, similar to the tensile tests. Although the titanium did perform worse, it did follow a linear path concerning time, as expected in an abrasion test. Because of this, a more uniform mixture can be inferred. This was the cause for the higher tensile stress and lower standard deviation compared to its ZnO ABS-like counterpart. The physical difference in size between the two nanoparticles was, at most, 20 nanometers but only about 10-15 nanometers on average. The density difference of 1.38 g*cm-3 between the two nanoparticles contributes to the compatibility with the ABS-like resin. As the ZnO has a higher density, less material would be added per gram than the TiO_2, reducing physical attributes.

Although the ABS-like material did not beneficially pair with the nanoparticles, the base resin did. The resin material significantly improved all physical properties when paired with a nanoparticle and still reattained great printing attributes. The first noticeable difference in the tensile testing data is the increased tensile testing strength in the ZnO nanocomposite. Although the ZnO nanoparticles performed worse than the TiO_2 when looking at the ABS-like samples, the opposite appears to happen here with the base resin. The ZnO showed a 38.4% improvement in tensile strength and a 52% decrease in maximum strain. This result is expected as the

nanocomposite has created a much more rigid part that can withstand higher stresses as the nanoparticle helps disperse the load.

2.3.2 Abrasion and Water Contact Testing

The abrasion testing was conducted under a constant water stream and at a pressure of 15.9 KPa. The grinding disc was aluminum oxide with 50-micron-sized abrasives. The disc was rotated at 100 rpm, and the head holding the sample was rotated at 250 rpm. Each sample was put through the grinding process for 5 minutes at 30-second intervals. The procedure is depicted in Figure 5.

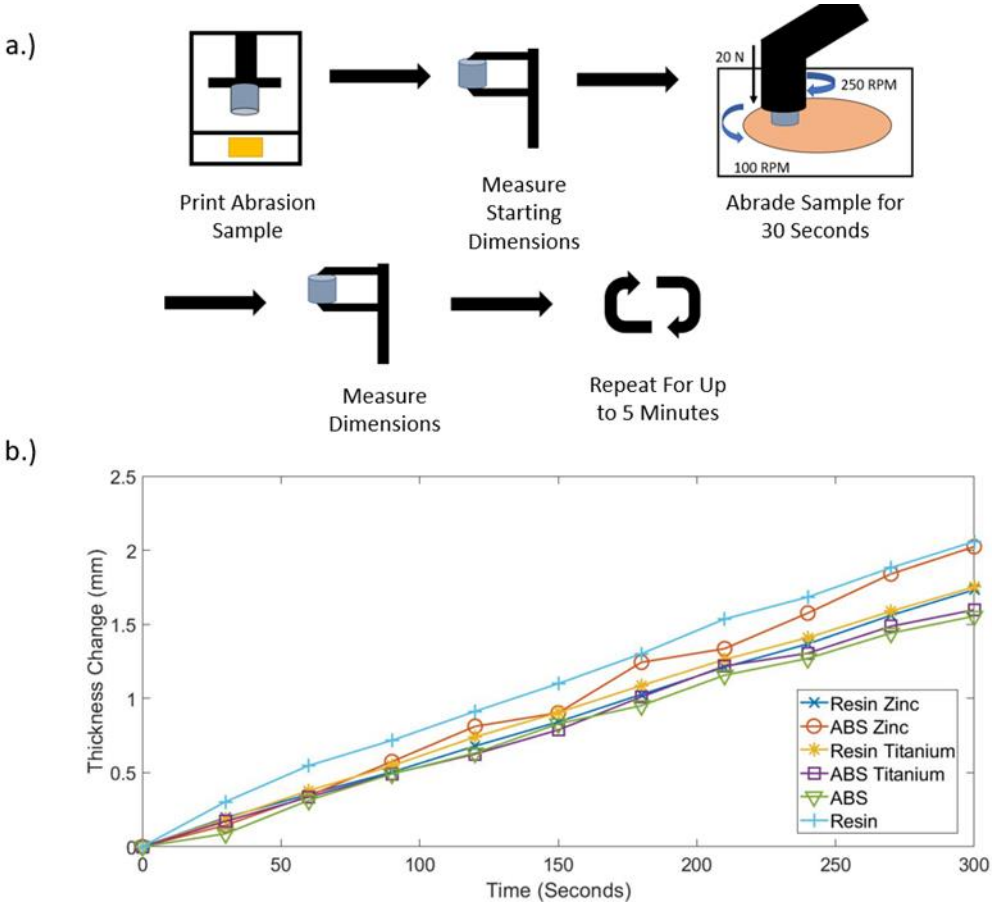


Figure 5: (A.) Abrasion Testing Procedure for All Samples. (B.) Abrasion Testing Results Compared Across 5 Minutes of Abrasion.

Starting with the control resins, the ABS-like resin had the least material degradation of all samples at just 1.55 mm. Comparatively, the non-ABS resin had the highest material degradation at 2.059 mm. These tests are equivalent to dragging a part over 471 meters of abrasive material with 15.9 KPa of pressure. This equated to over 300 meters of abrasion per millimeter of thickness change for the ABS-like photopolymer and over 225 meters for the resin.

The nanocomposite samples fell between the above two base samples, with the most notable distinction being the added abrasion resistance in the resin samples. Both resin nanocomposites performed very similarly, with a thickness reduction of 1.733 mm for the ZnO resin nanocomposite and 1.752 mm for the TiO_2 resin nanocomposite. These samples show a 15.8% increase in abrasion resistance compared to the non-modified material. In contrast, both ABS-like resin nanocomposites showed a decrease in abrasion resistance. The ABS ZnO nanocomposite performed the second worst with a thickness change of 2.024 mm. The ABS TiO_2 sample showed a degradation of 1.598 mm, which is still slightly better than all other non-ABS tests.

The difference between the two materials becomes apparent in analyzing the abrasion data. The factory ABS-like photopolymer outperforms all other tested materials and has a 24.7% increase in abrasion resistance compared to the factory resin. This difference constitutes the main design point behind the ABS-like material when printing end-use functional parts. This increased abrasion resistance also makes the material a strong candidate for implementation where low stresses will be seen, but high traffic is expected.

These results reinforce a superior bond between the base resin and the nanoparticles compared to the ABS-like resin. ZnO did not outperform TiO_2 in abrasion testing, though, as the type of degradation the part is experiencing will likely not increase from one nanoparticle to the

next. The increase in abrasion resistance for both resin nanocomposites was not only an improved property but also an improvement in abrasion consistency. Out of all abrasion tests performed, the resin nanocomposites demonstrated the most linear degradation curve with respect to time. This further promotes the theory that there was improved bonding with the base resin and excellent homogeneity.

The last two physical tests performed were water contact angle and absorption tests. These tests were performed to characterize the material's ability to be used in wet environments for extended periods. The water contact angle measurements were completed for all six specimens using ImageJ software's drop snake analysis[93]. The factory resin showed an average contact angle of 68.8 degrees. All water contact angle tests were performed on the printed surface with no post-printing alterations. The TiO_2 was observed to reduce the water contact angle to an average of 52.85 degrees. This reduction was also seen in the ZnO nanocomposite but to a lesser degree achieving an average contact angle of 60.85. As shown in Figure 6, the TiO_2 nanocomposite had the lowest water contact angle across all tests for the resin matrix.

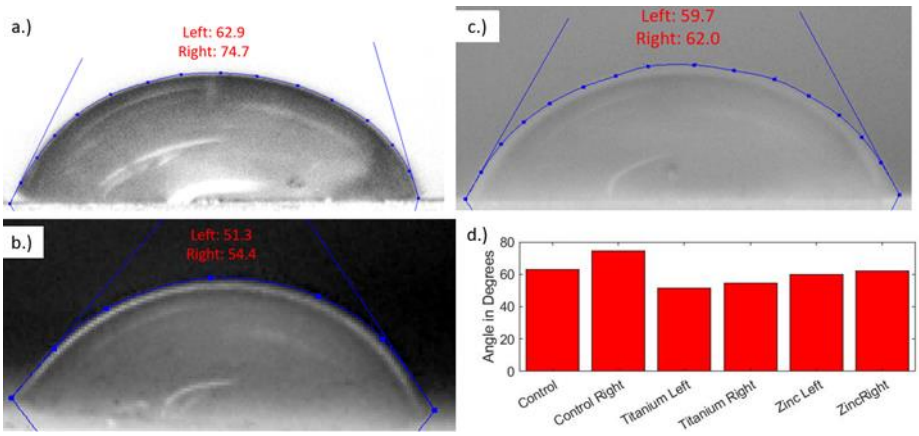


Figure 6: (A.) Control Resin Water Contact Angles. (B.) TiO_2 Resin Nanocomposite Water Contact Angles (C.) ZnO Resin Nanocomposite Water Contact Angles (D.) Bar Graph of All Resin Water Contact Angles

The ABS matrix performed similarly but with higher overall values for all tests. The control contact angle was 16.1% higher at an average of 79.9 degrees. This larger contact angle affected nanocomposites similarly, with average contact angles of 60.5 and 71.7 degrees for TiO_2 and ZnO nanocomposites, respectively. As observed in the resin specimens, the TiO_2 also demonstrated the lowest water contact angle overall for the ABS matrix material, with all data shown in Figure 7.

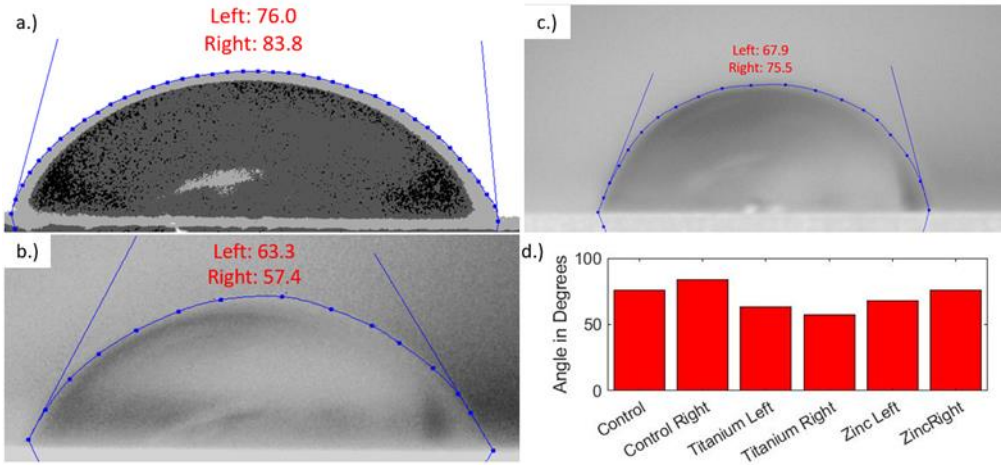


Figure 7: (A.) Control ABS Water Contact Angles. (B.) TiO_2 ABS Nanocomposite Water Contact Angles (C.) ZnO ABS Nanocomposite Water Contact Angles (D.) Bar Graph of All ABS Water Contact Angles

Since the parts demonstrate hydrophilic properties, it is vital to ensure that the water absorption of the material is relatively low to ensure that they can still be applicable in wet environments. Water absorption testing performed followed ASTM D570 for plastics. The tests were performed for over 20 days, and the maximum water absorption rate recorded was 4% by weight—the absorption rate plateaued at day 15 following a logarithmic curve, as shown in Figure 8. Within the first 24 hours, the samples saw a 1.39% gain in weight and a 1.73% gain

over the first seven days. After six months of continued submersion, the specimens were checked and saw no increase past the 4% observed in the first 15 days. Specimens were left at room temperature for all tests.

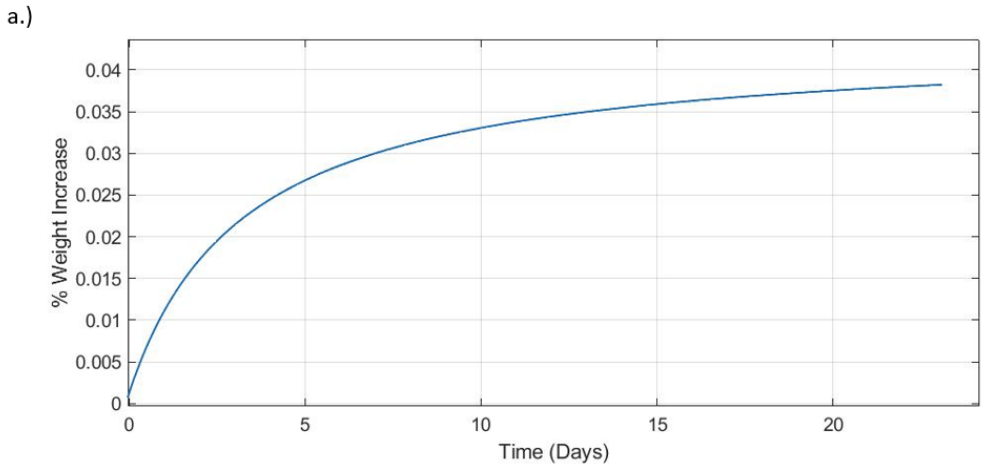


Figure 8: Water Absorption Percentage Over Time.

Water contact testing demonstrated little effect on the surface of the materials. TiO_2 was used as previous studies have shown that it tends to create hydrophobic surfaces after exposure to the sun[94]. As all testing was done indoors and long-term sun exposure was not tested, these attributes were not observed on our samples. The water absorption testing did produce results as expected for polymer-based materials and would, therefore, not be a barrier for fluid implementation. Further research into surface modification through sun exposure of TiO_2 specimens would help provide more supporting evidence for the fluid system involvement of parts.

2.3.3 SEM Imaging

SEM provided validation of a homogenous dispersion across the surface of the printed pieces. An even dispersion with little clumping is required to observe antibacterial traits on the surface of the prints. The SEM images provided in Figure 9 show TiO_2 and ZnO on the surface of the resin matrix. Both images were taken from parts produced on the printer with no modification except for sputter coating, which is required for the SEM process. The nanoparticles can be seen circled in red on each image below. Again, minimal clumping was observed, and the dispersion was excellent across the inspected image.

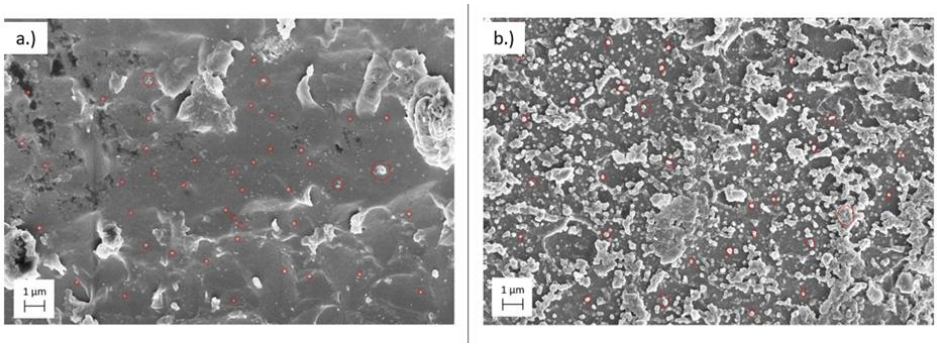


Figure 9: (A.) SEM Imagery of TiO_2 Particles in A Resin Sample. (B.) SEM Imagery of ZnO Particles in A Resin Sample.

SEM proved that a sufficient dispersion was achieved with minimal clumping. As these parts are printed layer by layer, the SEM imagery shows the first and last layer of the print depending on the side it was taken. This reinforces the data that particle settlement was not an issue during printing. This also shows that new nanoparticles will be continuously exposed to the surface as the part wears down to keep the part's antibacterial properties active.

2.3.4 Proposed Applications

The critical discovery within this work is the rapid synthesis and production of antibacterial parts using 3D printing technologies. The ability for non-specialists to produce custom parts in under several hours specifically designed for the medical field will help speed up the adoption of 3D printing in the medical sector. In addition, the materials used are easy to handle and store while only requiring basic safety measures such as nitrile gloves and eye protection. Therefore, hospitals will not require specialized training and facilities for implementation. Photocurable-based AM has already proven to be one of the best-suited technologies for the healthcare industry[95-98]. LCD-based printing systems also offer a significant advantage in processing speed as entire layers can be cured at once compared to more expensive SLA machines [98]. The most notable example was the prosthetic finger, as all pieces were printed on one build plate.

Due to the high accuracy possible with these machines, it is straightforward to manufacture parts that interface together[99]. The prosthetic finger example can be assembled in minutes and is easily sized for anyone. The design freedoms available when using AM are widely known, but implementing these machines into end-use cases has been problematic due to the array of downsides of this new technology. As documented here, photocurable 3D printing paired with novel nanocomposites suffers from very few disadvantages that other 3D printing technologies suffer. The part's physical properties are entirely suitable for biomedical uses, the accuracy and resolution are well within desired tolerances, and the ease of manufacturing allows for trouble-free manufacturing.

Resins' unique printing ability allows a part to be printed with no visible layer lines. For example, a design of a 3D chess rook was printed in an ABS ZnO nanocomposite to showcase

the intricate detail that this novel resin can uphold while still being fully functional. As the printing process is done layer by layer, intricate details such as internal features can be produced, as seen by the internal staircase on the rook. The other benefit is that large hollow cavities can be drained of resin during washing and cured empty to reduce overall weight. This leads to design freedom not abundantly found in composite manufacturing and, most importantly, not easily implemented in traditional manufacturing.

CHAPTER 3: HIGH-CONCENTRATION ZINC OXIDE ANTIBACTERIAL NANOCOMPOSITES

3.1 Introduction

With the promising results from the low-concentration studies presented in the previous chapter, it was decided to utilize ZnO as a nanocomposite additive but in higher wt% concentrations. As the base resin material performed favorably to nanoparticle addition, that material was retained for this study. Several changes were made to the methods to help solve issues with agglomerations and uneven mixing, such as including a planetary ball mixing system and increased mixing times. Additionally, a new printer was sourced that offered higher energy transfer to the print to allow for faster print times. At this point, research also began studying the effects of thermally controlling and modifying different parts of the manufacturing process.

This study aimed to develop a manufacturing method allowing small spherical-shaped nanoparticles to be added to base resin materials and manufactured in commercially available machines. This study will help further develop important manufacturing characteristics that influence final part strength and manufacturability. The insights gained from these results will be further used to refine the manufacturing settings for high-concentration nanoparticle resins.

3.2 Materials and Methods

The AM system utilized to produce the samples was an Elegoo Mars 2 Pro masked stereolithography (MSLA) printer. MSLA curing systems often suffer from light leaks around the LCD. Therefore, a monochrome LCD is implemented in the Mars 2 Pro to increase light transmission and help with the above issues. The base matrix material was a standard photopolymer from Elegoo in grey coloring. The resin comprises epoxy resins, hexamethylene

diacrylate, N-glycine, and hydroxy cyclohexyl phenyl ketone. This was chosen due to the low viscosity of the material relative to other low-cost options and the quick cure times when paired with their respective machine.

The nanoparticle of choice was ZnO, sized between 10-30 nanometers from US Research Nanomaterials Inc. Zinc oxide was chosen due to its antibacterial properties, use in human-safe products, and low cost. In addition, the part will require complete dispersion of the nanoparticle throughout to exhibit antibacterial properties; therefore, several different concentrations were tested to analyze the particle's effect on the part's physical properties.

To fabricate the novel nanocomposite slurry, the nanoparticle was added to the matrix resin in the following weight concentrations: 1%, 2.5%, 5%, and 7.5%. The nanoparticle was dispersed throughout the matrix material through a high-speed centrifugal mixer to reduce agglomeration, as demonstrated through SEM in Figures 27 and 28. An AR-100 Thinky mixer was used at 5 minutes of mixing and 2 minutes of degassing for all mixtures utilizing a centrifugal process for air removal. This process also heated the material due to the process's friction and decreased the viscosity of the final mixture. This aided in reducing trapped air molecules when transferring the mixture to the printing vat. Once loaded into the printer, the custom print settings were uploaded, and the print was started. After 10 minutes of printing, the print was paused to ensure the part had adequately adhered to the build plate. If so, the print was left to resume to completion and removed for post-cleaning and curing. The entire process is depicted in Figure 10 below of the fabrication and manufacturing of the novel resin material.

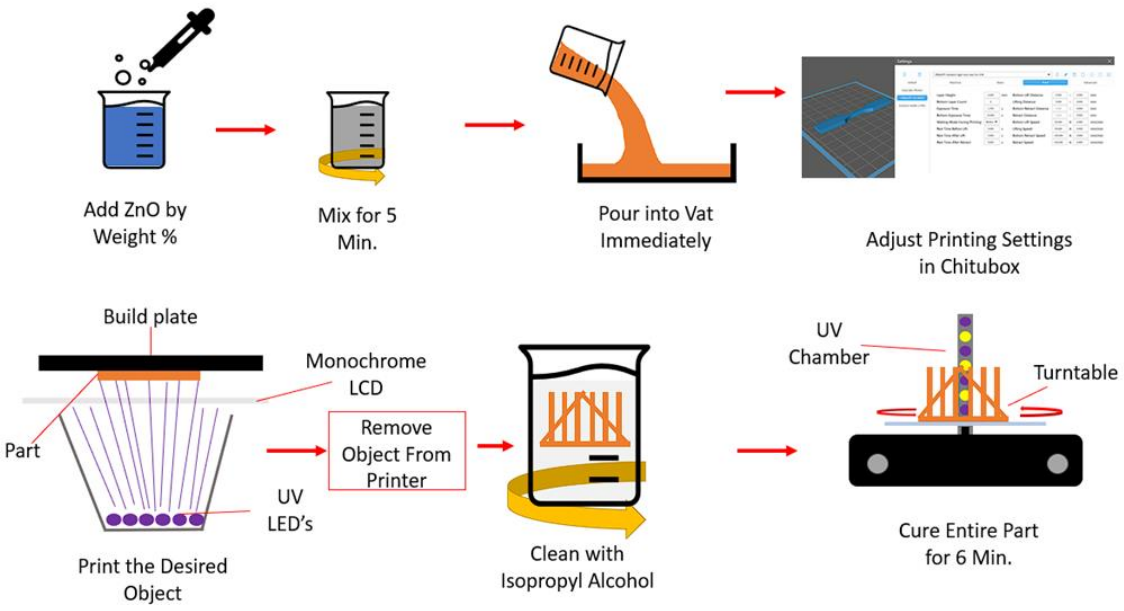


Figure 10: The Manufacturing Process for ZnO Nanocomposite Resin.

Proper particle dispersion is a substantial problem when working with nanoparticles of this size. Utilizing a low-viscosity resin is ideal for helping aid the overall particle dispersion, but heating the material also proved advantageous to the mixing process. The resin was heated on a hot plate at 60° Cand then left to cool to room temperature. This resin was then utilized in the printer without adverse effects on printing. This data was then used to help set mixing times based on the change in viscosity due to the thermal change of the material. Mixing times of 2 minutes led to insignificant changes in matrix temperature, and large agglomerations were still visible. Increasing this mixing time to the 5-minute while adding a degassing phase solved these problems. This procedure reduced the overall viscosity of the resin at all concentrations to a value lower than the control matrix at room temperature while completely dispersing the nanoparticle, as later demonstrated through SEM. Substantial air pockets were formed in the

nanocomposite when mixing for a longer duration. A 2-minute degassing phase on the Thinky mixer was incorporated to remove these air pockets.

The selected matrix utilizes isopropyl alcohol as a solvent, so all parts were rinsed thoroughly when removed from the printer. This ensured that inspected parts did not contain ZnO on the surface due to inadequate cleaning, but the nanoparticle was deposited within the part during the printing process. To obtain reliable antibacterial testing, ensuring that the ZnO reacting with the bacteria was adequately bonded to the part and not simply attached to the surface was critical. Thorough cleaning with a solvent ensured that only ZnO left exposed to the surface was adequately bonded and, therefore, would wear over time alongside the matrix.

Characterization of the mechanical properties of the nanocomposite was performed through testing of tensile specimens that would be printed for each variation of material. The printer was unmodified to produce the tensile specimens for testing, and all samples were printed at 22° C. Cure times were adjusted based on the nanoparticle concentration to print the nanocomposite, as shown in Table 1 properly. The nanocomposite was printed using control settings to determine optimal cure times, and cure times were gradually increased until print failures were no longer present. ZnO is often utilized for its UV absorption characteristics. Therefore, the cure time had to be increased to cure the photopolymer around the particles. To ensure that this change in cure time during the printing process did not affect the final strength, all samples were exposed to UV light in a chamber for a minimum of six minutes after removal from the printer. This should negate any difference in strength gained during the curing inside the printer. The prints were composed of two distinct layer settings. These layers refer to the first five layers produced by the printer and any layer printed after that. There was no change in the dimension of these layers, but the cure times were changed to aid in creating a solid foundation

for the part to print on. The bottom layers physically bond to a stainless-steel sheet and must be more completely cured to support the rest of the print. The remaining layers are cured much shorter to allow the curing reaction to progress enough for the part to hold its geometry but still require post-UV treatment. This dramatically reduces print time and allows easier post-processing, such as support removal. A total of five bottom layers were used on all parts, with a total layer count of 33.

Table 1: Cure Settings for All Different Novel Nanocomposites

Weight %	Bottom Cure Time (S)	Normal Cure Time (S)
0%	30	2.5
1%	35	3
2.5%	40	3.5
5%	50	5
7.5%	60	8

To test the tensile strength of the specimens, an Instron 5969 was utilized with a constant deformation rate of 1 mm/min. The tensile specimens were based on the ASTM D638 standard utilizing a barbell style with a gauge length of 40mm, a gauge width of 10mm, and a thickness of 1.75mm. The testing machine utilized a 5kn load cell, and all samples were tested with zero pretension and preload applied. A total of six specimens were tested for all concentrations to assess variability. These specimens were analyzed under an optical microscope to determine the

failure mode. In addition, an optical microscope image was processed through ImageJ and tested across four samples to determine the water contact angle [100].

3.3 Results and Discussion

To properly characterize each material in mechanical applications, tensile tests were performed with ultimate tensile strength, modulus, and strain metrics. These samples were analyzed under a microscope to identify the failure mode and ensure it was not due to a defect in the printing process. Water contact angle measurements were performed and characterized across all samples to analyze changes in surface energy. This data was paired with SEM imagery to characterize the particle dispersion on the surface. SEM images were analyzed using particle analysis to provide insights into agglomeration size, with EDS being utilized to verify the ZnO concentration.

3.3.1 Tensile Test Results

For the six control samples of only the matrix material, an average stress of 31.6 MPa was demonstrated with Young's modulus of 118.8 MPa. These statistics reveal that the base matrix performs similarly to the commonly used ABS thermoset when under load with an increased strain[101]. An increase in the ultimate tensile stress and modulus would be expected to improve the practical use of the matrix.

Starting with the 1% ZnO nanocomposite, all mechanical parameters were reduced. Stress was reduced by ~ 15%, while maximum strain increased by ~ 44%. These parameters reduce the practical applications of the material and eliminate the usefulness of a nanocomposite with a ZnO concentration of 1%

At 2.5% ZnO concentration, parameters were increased from the 1% specimens. These samples performed statistically similar to the control group, with an average ultimate tensile stress of 30.3 MPa and modulus of 848.2 MPa. More importantly, is a reduction in standard deviation for both parameters across all samples.

The maximum increase in ultimate tensile strength was observed at the 5% ZnO concentration with a 39.5 MPa. This is a ~ 25% increase compared to the control matrix. Additionally, a 36% increase was observed in the material modulus with a standard deviation over three times less than the control. These samples demonstrated the least maximum strain at only ~ 6% and had the least maximum strain deviation out of all samples tested.

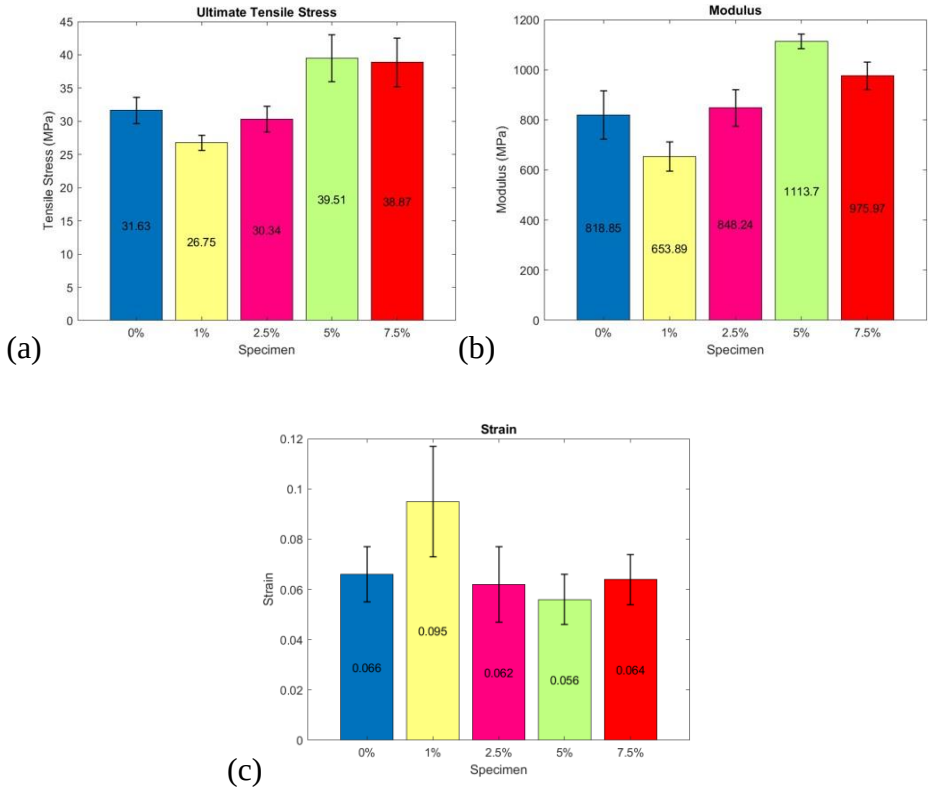


Figure 11: (A) Average Ultimate Tensile Stress with Error Bars Representing Standard Deviation. (B) Average Modulus with Error Bars Representing Standard Deviation. (C) Average Maximum Strain with Error Bars Representing Standard Deviation.

The final 7.5% ZnO samples tested performed statistically similar to the 5% samples regarding tensile strength. However, degradation in modulus and the ultimate strain was observed with a modulus of 975.97 MPa. The average maximum strain of these samples was statistically identical to the control and 2.5% samples at ~ 6%. The ultimate tensile strength and modulus of all samples were graphed in. When visually compared, it is relevant to note the increase in standard deviation for ultimate tensile stress as ZnO concentration increases. However, this is the opposite for the modulus, as the lowest standard deviation amounts were observed in the 5% and 7.5% samples. This trend allows for insights into the mechanical function of ZnO in terms of stiffness and strength addition and leads to better theories on the fracture mechanism of the material. All mechanical data and the standard deviation are presented in Table 2.

Table 2: Stress, Strain, And Modulus Data for All Samples, Including Standard Deviation

Weight %	**Stress (MPa)**	**Strain**	**Modulus (MPa)**
0%	31.6±2	0.066±0.01	818.85±96.37
1%	26.8±1.2	0.095±0.022	653.89±58.73
2.5%	30.3±1.9	0.062±0.015	848.24±73.39
5%	39.5±3.5	0.056±0.01	1113.70±30.18
7.5%	38.9±3.7	0.064±0.009	975.97±55.44

The main advantage of designing a nanocomposite utilizing ZnO is the presented antibacterial properties, but increases in mechanical strength were also witnessed. A disadvantage addressed in this study was the effect of the UV-absorbing nanoparticle when introduced into a thermoset cured at these wavelengths. ZnO nanoparticles from 15-40 nanometers have been documented to absorb UV wavelengths [40, 42]. This absorption of UV light directly affected the required cure times and defects in the specimens. The tensile tests performed gave insight into the nanoparticle's effect on the material's strength and stiffness. Further investigation utilizing SEM provided insights into failure modes and dispersion characteristics.

Ideal applications for this material would be in heavily trafficked areas with a large volume of human contact. Specific applications include dental implants, prosthetic appendages, and high-contact hardware such as doorknobs. Additionally, a reduction in strain is often required in items such as dental implants and prosthetics, as unwanted deflection can cause discomfort for the user. This technology best suits creating one-off parts that cannot be traditionally manufactured and require complex geometry. Introducing the nanoparticle at a 1% concentration reduced ultimate tensile strength and stiffness compared to the control. This is likely due to the addition of the ZnO causing minor defects in the sample and, at such a low concentration, being unable to make up for those defects mechanically. This theory further presents itself when analyzing the 2.5% and 5% concentrations, as the strength and stiffness increase linearly.

3.3.2 Water Contact Analysis

Water contact angles were measured for each sample to characterize surface quality and function the ZnO provides. As a baseline, the control showed a water contact angle of 48°,

demonstrating hydrophilic properties. Any increase in the contact angle would be beneficial as it would help reduce the amount of moisture that would adhere to the surface of the parts.

All tested samples saw an increase in the contact angle of water, indicating a reduction in the material's surface energy. For example, the sample with 1% saw an increase of 13.5°, while the 2% and 7.5% samples saw an increase of 8°. The most significant improvement was at the 5% concentration with a contact angle of 69.5°. The comparison between the control and the 5% ZnO sample is depicted in Figure 12

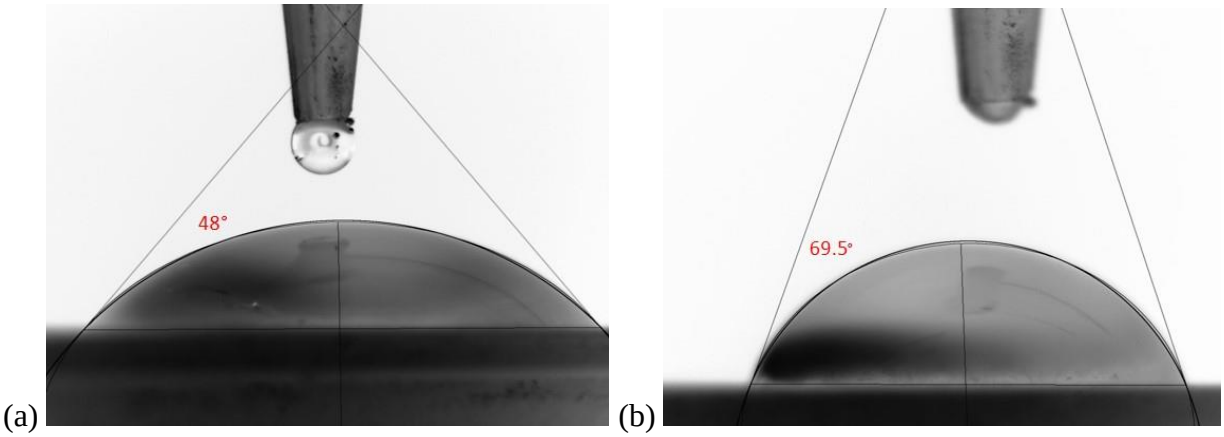
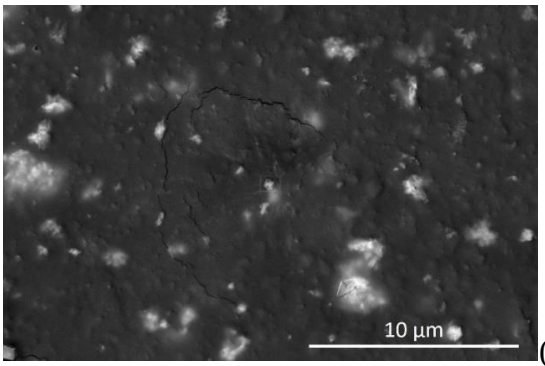


Figure 12: (A) Water Contact Angle of The Control Sample. (B) The Water Contact Angle of the 5% ZnO Sample

3.3.3 SEM Analysis

SEM was conducted to identify the dispersion and agglomeration characteristics of the nanocomposites. This allowed for the inspection of particle size, agglomeration, dispersion, and EDS analysis. Along with this, it allowed for the documentation of voids and imperfections caused due to increase in ZnO concentration. To prepare the samples for high vacuum SEM, all samples were coated with iridium at 2-5 nanometers. Beyond this, the samples were imaged as printed.

(a) 

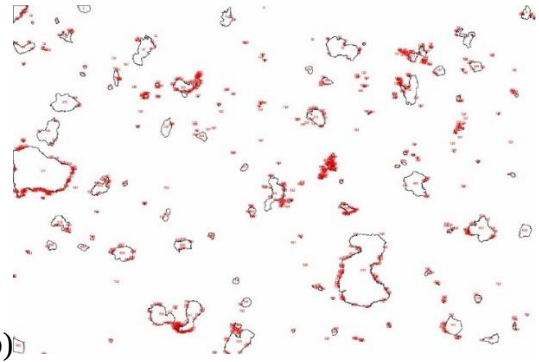
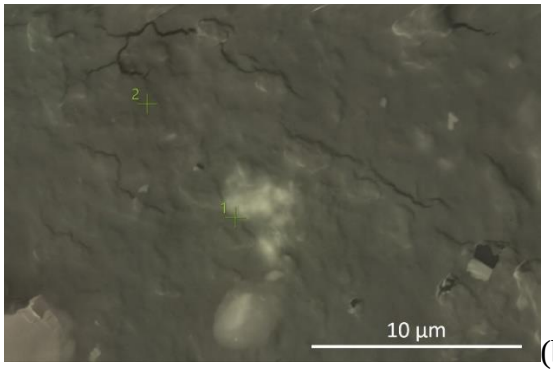
(b) 

Figure 13: (A) SEM Backscatter Imagery Of 2.5% ZnO Sample. (B) Particle Analysis Using ImageJ Demonstrating Surface Agglomerations.

To investigate the agglomeration of the ZnO, EDS was performed on the specimens, and then particle analysis through ImageJ was performed. Figure 13 depicts this process with a backscatter image of a 2.5% sample with the white agglomerations representing the ZnO. All images processed provided a rough estimate of surface coverage, demonstrating increased coverage with ZnO concentration. Figure 13 Image b also noted that large agglomerations were present but did not prevent an even coverage of the material's surface. As backscatter imagery was used at a 15kV accelerating voltage, these images depict the layer up to several microns under the surface providing evidence for 3D dispersion of the ZnO.

(a) 

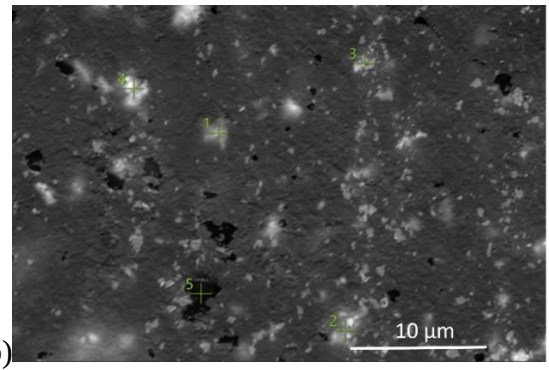
(b) 

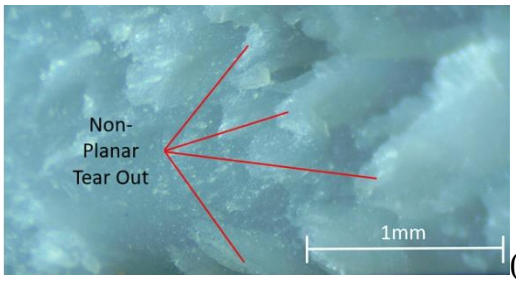
Figure 14: (A) SEM Backscatter Imagery Of 1% ZnO Sample with EDS Inspection Points at Markers. (B) EDS Analysis Of 5% ZnO Sample Validating Voids and ZnO Agglomerations.

Inspection of the samples at magnifications above 5000x begins to show geometrical voids and issues with samples at and above 5% in multiple locations of the sample. To adequately identify the makeup of the sample, EDS was performed on the samples. In Figure 14, image a, the number 1 inspection point provided a weight percentage of 57.4% for Zn while being completely absent at inspection point 2. Along with this, the sample's surface lacks voids and surface roughness. Comparatively, the 5% sample in Figure 14, image b, shows multiple voids and surface defects, although the zinc concentration was much higher. The void was verified through EDS, with inspection point 5 returning a complete lack of Zn. Inspection points 1 through 4 returned varying weight percentages of Zn ranging from 25.9% to 58.6%. This meets theoretical expectations based on the interaction volume of the electron beam picking up x-rays from below the ZnO agglomeration. Based on these results, the main concern is the voids' effect on the strength and reduced ability to qualify the process over mass manufacturing.

The ZnO agglomerations can be measured in the SEM images in Figure 13 and 14. A void would be defined as a pocket of resin left uncured due to improper light exposure. The

creation of voids increases with ZnO agglomeration size as the overall UV absorption per unit area increases. Utilizing SEM images, many agglomerations were documented to fall under 2 microns in diameter. When utilizing a layer height of 50 microns, a stack up of 2-micron agglomerations would gradually absorb the UV light as it travels vertically through the layer. This would lead to increased voids as nanoparticle concentration increases. This was demonstrated in Figure 29, with the 5% sample having significantly more voids than the lower 1% concentration samples. These voids would soon reach an equilibrium where the mechanical strength added due to the nanoparticle would be non-evident due to the void count.

Additionally, the larger the voids present, the increased probability that the sample would fail prematurely, leading to a larger standard deviation concerning tensile stress. This problem appears to happen in the 7.5% ZnO concentrations, where the tensile strength is statistically similar to the 5% sample when considering standard deviation, but the modulus of the material is reduced. This increase in maximum strain is a key indicator of larger defects within the sample that also increase the large strength variability. Optical microscope images were taken of the fracture point of several samples to provide more insight into the failure mechanism, as seen in Figure 15.

(a) 

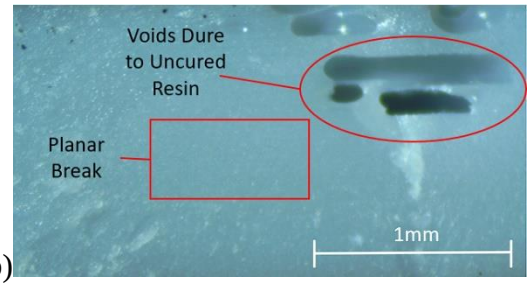
(b) 

Figure 15: (A) Optical Microscope Image of Fracture Point Of 7.5% Sample (B) Optical Microscope Image of Fracture Due to Voids On 7.5% Sample

The image in Figure 15a was taken of a sample that fell within the range of expected tensile values as provided by the data. An obvious tear-out is observed, with a nearly crystalline structure left behind. The image in Figure 15b was taken of a sample that failed prematurely with large voids. The images are presented with the z-axis traveling vertically through the images. No layer lines are visible, but the voids appear to have formed within several consecutive layers leading to a weakened sample. An important note is that the fracture point on the defective sample shows no tear out and resembles a smooth surface indicating that the point at which the ZnO became the functional mechanical structure was never reached.

The presented data leads to the theory that ZnO addition to a UV curable resin matrix increases the part's mechanical properties by up to 5%. This considers the failure in achieving a defect-free sample, allowing future research in processes to reduce the void count. SEM images for samples up to 2.5% demonstrated no concerning void creation near or around the ZnO. At and above 5%, these voids became very apparent and were often located near a large agglomeration of ZnO. As ZnO absorbs the UV, it is suspected that the imaged voids are uncured resin surrounding larger ZnO groups. Possible solutions to this issue would be to reduce layer height and increase energy density per unit volume of the nanocomposite. Increasing the dispersion of the ZnO, specifically through methods such as tip sonication to help overcome the surface energy of the particles, should also be further investigated. Lastly, performing thermal studies on the temperature and viscosity of the nanocomposite during the printing process would likely lead to improved part performance.

3.4 Conclusions

The work presented in this study demonstrated several key findings, including the importance of optimized cure time for different nanoparticle addition, the possibility of in-situ

heating to decrease viscosity and increase print speed, and the mechanical limit reached for a given nanoparticle regardless of weight concentration. Similar to the first study, improvements in mechanical strength were demonstrated. Contrary to the first study, these improvements were not observed until high loading percentages. This was determined to be caused due to the unoptimized cure times for each material. As cure time was linearly increased with nanoparticle loading, the higher concentration nanocomposites likely reached a further degree of cure than the lower concentrations. While it is expected that degree of cure will change with a change in loading, further research will have to be performed to find the effect of nanoparticle addition given a constant cure time. Further investigations into possible reasons for void creation and inadequate bonding at higher nanoparticle concentrations should be studied.

CHAPTER 4: HIGH-CONCENTRATION TITANIUM DIOXIDE ANTIBACTERIAL NANOCOMPOSITES

4.1 Introduction

It was determined from the previous two studies that precise control would have to be put on every step to quantify the key characteristics in the manufacturing process. To adequately cure each nanocomposite would require a specified cure time and condition from resin synthesis through post-cure. This study will aim to continue using high concentrations of an antibacterial nanoparticle but will precisely control the entire manufacturing process and keep cure settings constant across all nanocomposites. The base resin will also change for this study to an engineering quality resin that is biocompatible certified, as this is a better candidate for end-use parts with antibacterial properties.

During the printing process, there are two stages of curing: the bottom cure, which incorporates the first 5 to 10 layers of a print, and the normal cure, which constitutes all remaining layers of a print. As this study's goal is to identify if a given cure time is optimized for a single nanoparticle concentration, it has been designed to print the parts normally than machine off the material manufactured with the differing settings. This ensures that any differences in material properties will be solely due to the nanoparticle addition and not any other attribute during manufacturing. These steps will allow for a conclusion regarding the effect of nanoparticle addition for a given cure time and whether the cure time should be modified for different nanoparticle concentrations.

4.2 Methods and Materials

The resin selected for this research was an off-the-shelf externally biocompatible certified engineering grade thermoset from Sirya tech. The Blu Clear V2 formulation was utilized as the matrix material as it had documented properties, cure settings, and post-processing instructions for obtaining biocompatible parts. Additionally, the clear nature of the sample would allow us to analyze TiO_2 interaction with the resin better. The resin was recommended to be printed at a minimum of 30° C. The printer selected was an Elegoo Mars 2 Pro with no modifications. To achieve the elevated printing temperatures required, an aluminum convection oven was specially constructed to circulate warm air at a specified temperature. A thermocouple regulated the temperature above the printing vat and held the chamber within 1° C of the 40° C set temperature. As viscosity decreases with a temperature rise, the chamber was held at 10° C over the recommended minimum for the best results.

The nanoparticle of choice was TiO_2 ranging from 10-30nm in diameter sourced from sky spring materials. The selected nanoparticle was 99.9% pure. The smaller diameter nanoparticle was chosen to help improve overall part dispersion and resin infiltration. No preprocessing was performed on the material before being added to the resin.

Three different nanocomposite concentrations were chosen for this study, including 2.5%, 5%, and 7.5% TiO_2 by weight. Each batch of specimens required a minimum of 120 grams of nanocomposite for printing. The resin was mixed in 70-gram batches utilizing a Thinky AR-1000 mixer. Each batch had TiO_2 added by weight percentage and mixed by hand before being inserted into the Thinky mixer. The composite was mixed for 10 minutes and degassed for 2.5 minutes. These time intervals were determined based on the final temperature and viscosity of the material. At the end of the combined mixing and degassing process, the material temperature was 36.5° C.

This increase in temperature led to a better particle dispersion as the viscosity reduced, and the agglomerations could separate through the mixing processes.

Once mixed, the material was transferred to the printer and encapsulated in a custom convection heating chamber that maintained a temperature of 40° C. The resin was allowed to sit in the vat for 20 minutes or until temperature equilibrium was reached. Next, printing settings were calculated based on the printing performance of the highest nanocomposite concentration. This was done by printing a resin manufacturer calibration test and checking the test for tolerances. Settings were continuously changed until all of the tolerances were met. The final cure settings consisted of five bottom layers at a cure time of 27.5 seconds and the remaining layers exposed to the light for 3.5 seconds. The manufacturer-recommended settings for the machine and virgin resin were 45 seconds and 3.5 seconds. This means that the virgin resin should perform as stated by the manufacturer, and the reduced bottom layer time was indicative of a better printer setup leading to fewer build plate adhesion issues.

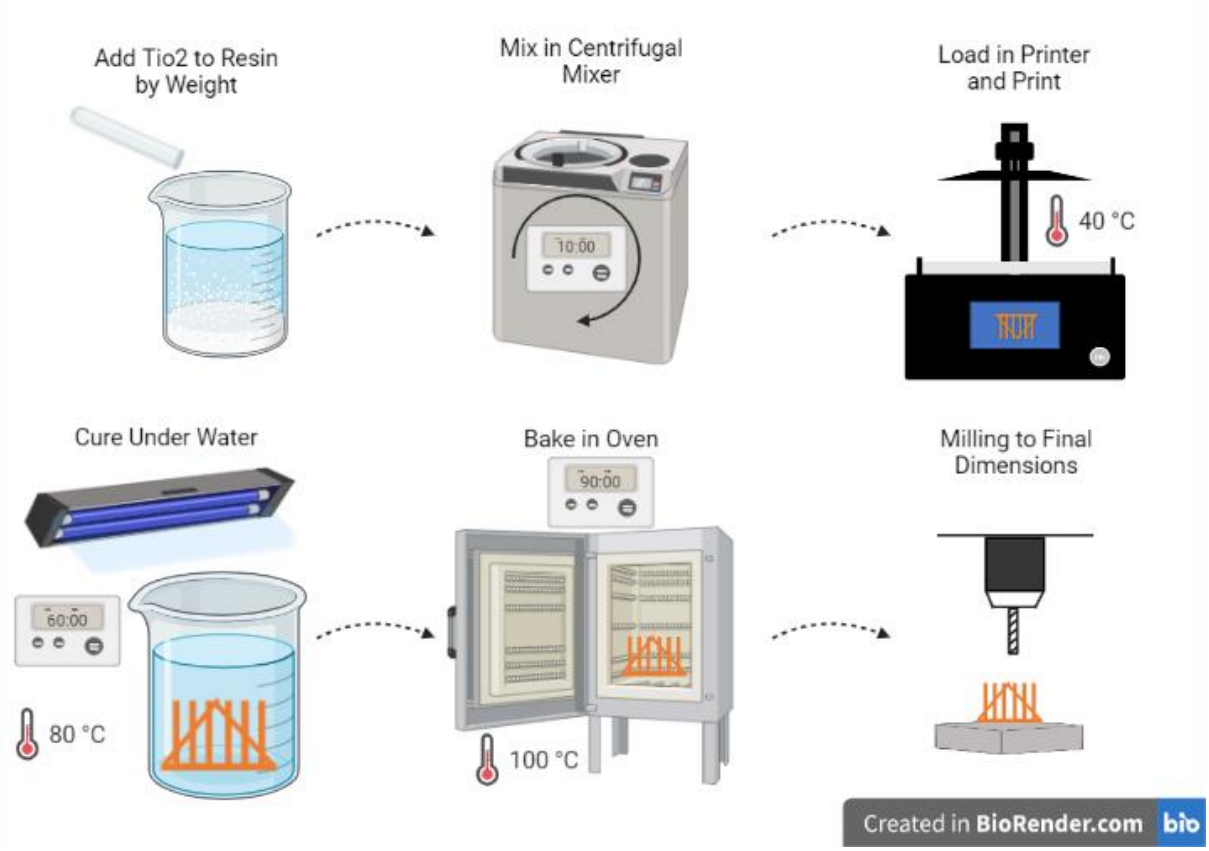


Figure 16: The Manufacturing Process of TiO_2 Nanocomposite Tensile Samples.

After confirming the printing parameters, ASTM D638 Sample V specimens were modified to be 1.78mm thicker. This extra thickness was added to be removed after post-processing to negate any side effects caused due to the bottom layers being cured for a longer time or the effect the removal process may have had on the part surface. Therefore, the part subject to tensile testing would be entirely cured at the 3.5-second interval, as the part cured for 27 seconds was machined off. The entire manufacturing process can be seen in Figure 16**.** In addition, samples were printed in batches of 7, as shown in Figure 38, to ensure that extraneous data could be traced back to an individual sample or a manufacturing error throughout the entire batch.

Once samples were printed, they were cleaned from the build plate. The cleaning process was performed using isopropanol alcohol as a solvent. Samples were cleaned using a Kim wipe dipped in isopropanol alcohol to wipe the samples clean. Submersion was avoided as the samples were set to print at the fastest possible cure time, and therefore the part had not reached full hardness. This led to specimen degradation when submerged as the isopropyl alcohol broke down the bonds forming within the sample.

The post-curing process was determined based on several other studies demonstrating increased mechanical properties when samples were printed at higher temperatures [43, 102]. Therefore, the samples were cured in a 405nm wavelength curing chamber inside an oven at 80° C with the experimental setup depicted in Figure 39. In addition, to aid in thermal distortion caused by the exothermic curing process, the samples were cured underwater in a 1L glass beaker. The water also aided in light refraction and diffusion to properly expose all sides of the samples. The parts were cured for a total of 60 minutes, with them being repositioned at the 30-minute mark to ensure an even cure.

The final step in sample preparation was removing the 1.78mm thickness added during printing. To do this, the samples were machined in a CNC mill utilizing custom fixturing and a probing system to ensure an accuracy of less than 25 microns, as depicted in Figure 40. In addition, these samples were machined with a toolpath that ensured the surface finish matched the printed surface and no chipping or unnecessary stresses were introduced into the sample. The samples were then dried in an oven at 100° C for 90 minutes and set aside for tensile testing.

4.3 Results and Discussion

4.3.1 Tensile Testing Results

The mechanical strength changes in the material due to the addition of the nanoparticle's ultimate tensile strength were determined through tensile testing. Twelve specimens per composite were tested, providing a power percentage of 80% with a minimum detectable change of 1.75 MPa. These values were chosen as they would show any difference over 5% in strength compared to the control, which would be deemed a reasonable enough increase to be practically useful. Tensile testing was performed on an Instron 5969 machine with a 5kN load cell and a 2 mm/min constant extension rate. The data collected included: load, extension, time, modulus, and video. In addition, this data was used to calculate ultimate tensile strength, modulus, strain, and digital image correlation. The table of average results can be observed in Table 3: Tensile Test Results for All Nanocomposites and Controls below, with the standard deviation also listed below the average value.

Table 3: Tensile Test Results for All Nanocomposites and Controls

Sample wt. %	0%	2.50%	5%	7.50%
Stress (MPa)	48.7±1.9	37.6±2.0	43.5±5.2	36.7±2.0
Strain	0.203±0.044	0.123±0.023	0.236±0.029	0.2337±0.040
Modulus (MPa)	567.2±49.8	686.6±36.6	510.9±58.3	428.1±51.1

The control resin demonstrated the largest ultimate tensile strength (UTS) compared to all novel nanocomposite resins. The most promising nanocomposite resin, at a 5% concentration, came within about 10% of the UTS value of the control resin but also suffered from the most

significant standard deviation. Notably, the tensile strength of the nanocomposites with higher and lower concentrations of TiO_2 demonstrated lower UTS compared to this sample set, even considering the large standard deviation observed. Further investigation into this phenomenon by analyzing the modulus of the materials, we discovered that the 2.5% TiO_2 sample demonstrated the largest modulus along with the least standard deviation. Furthermore, the modulus continues to decline as the concentration of TiO_2 increases, with the 5% sample demonstrating statistically similar results and the 7.5% sample demonstrating the lowest modulus out of all samples.

The strain data appears to follow an interesting phenomenon, with 2.5% of samples reacting differently than the rest. The 2.5% composite's statistically lower maximum strain relates directly to its increased modulus. Additionally, the 2.5% composite always fell within the two lowest standard deviation brackets for each category. In contrast, the 5% samples displayed the largest standard deviation for all categories besides strain. The drastic difference between these two steps indicates that the increase in nanoparticle loading plays a direct role in the ability of the material to perform consistently. The 7.5% composite confirms this idea as it also suffers from a large standard deviation compared to the control and 2.5% samples.

Utilizing standard deviation across all tests, it appears that the increased loading after 2.5% TiO_2 changes the molecular bonding of the material or causes the manufacturing process to create fewer uniform parts leading to unpredictable failures. However, as the UTS of the 5% composite was statistically stronger than the 2.5% samples, it does not appear to be a molecular bonding issue rather than a manufacturing defect. The 7.5% results further show this as the values continue to decline with increased loading.

These initial tensile test results uncover a trendline that points to an optimal composite loading falling between 2.5% and 5% TiO_2 by weight. It also demonstrates that adding the TiO_2

in low concentration can significantly improve modulus while not reducing repeatability regarding UTS results. Further investigations into the failure mode of the material revealed abnormal changes during the elastic region of the material, as depicted in Figure 17. For the 5% and 7.5% samples, the stress-strain curves depicted in Figure 17c and 17d portray an elongation in strain with no change in stress as expected at the end of the elastic region of a material. Comparatively, the control and 2.5% samples did not demonstrate this region as expected. This appears to have a significant role in the final modulus of the material but not the UTS. The final maximum strain of the material also has little effect on the UTS of the material, as the composite samples demonstrated both lower and higher maximum strain values compared to the control.

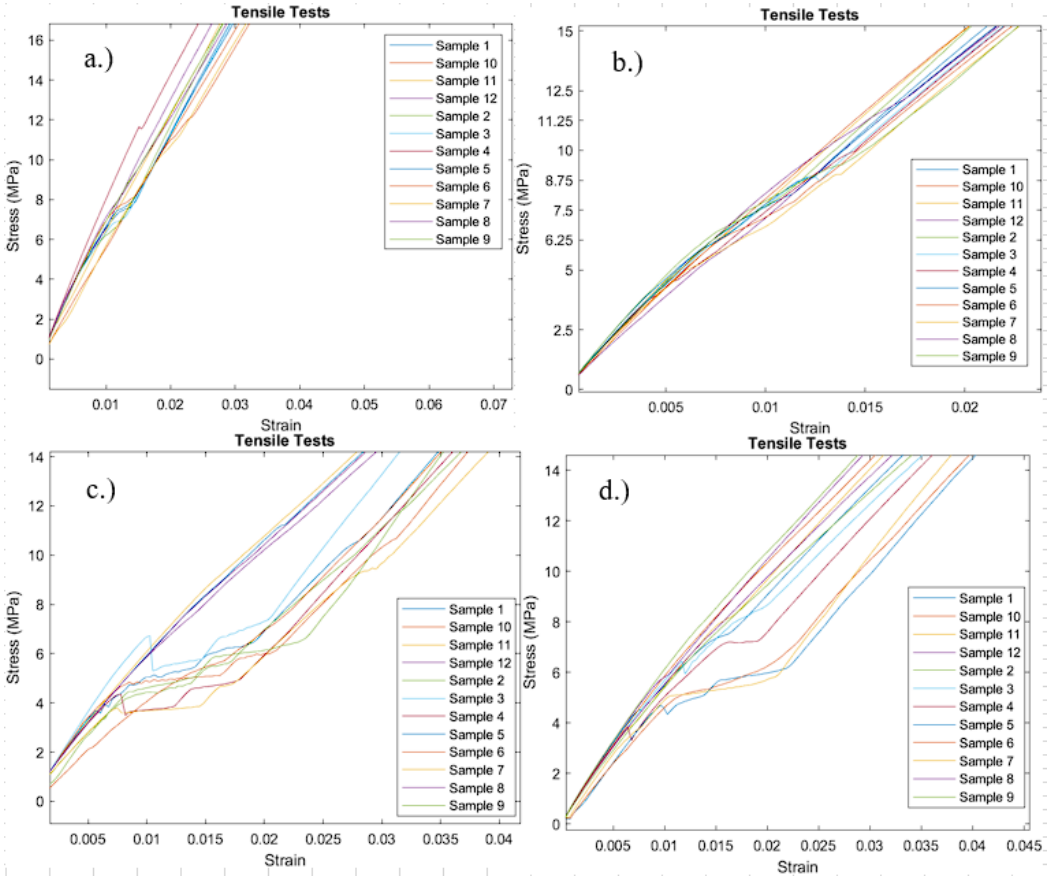


Figure 17: Elastic Region of All Samples. A.) Elastic Region of Control Samples. B.) Elastic Region Of 2.5% Concentration Samples. C.) Elastic Region Of 5% Samples. D.) Elastic Region Of 7.5% Of Samples

As all tensile tests were printed and post-processed using identical parameters, this leads to the theory that increased nanoparticle loading requires changes in the manufacturing settings. Previous research by the team utilized custom cure times for a ZnO nanocomposite and discovered that the loading of the material could surpass the virgin material with modified cure times [60]. This research presented here aimed to determine if the cure times adversely affected the results to favor the larger composites or if the composites directly led to the improved strength. Based on the results presented here, the composites improve the material's mechanical properties. However, their effectiveness diminishes if the cure settings are not adapted to compensate for changes in the uncured material properties such as viscosity, opacity, and cure rate. In addition, several other tests were performed to provide further information about what is causing the changes in the mechanical strength, such as SEM, High magnification optical microscopy, wear resistance, water contact angle, and glass transition temperature.

4.3.2 Digital Image Correlation

Videos of the tensile tests were taken to provide data used in digital image correlation. In addition, select samples were sputter coated using an airbrush to provide a unique pattern that software could recognize to provide strain and displacement analysis throughout the experiment. This allowed for a more thorough analysis of the stress distribution across the sample's surface and information about deformation right before the break. Results from the 2.5% and 5% nanocomposite samples are depicted in Figure 18, displaying the transverse deformation.

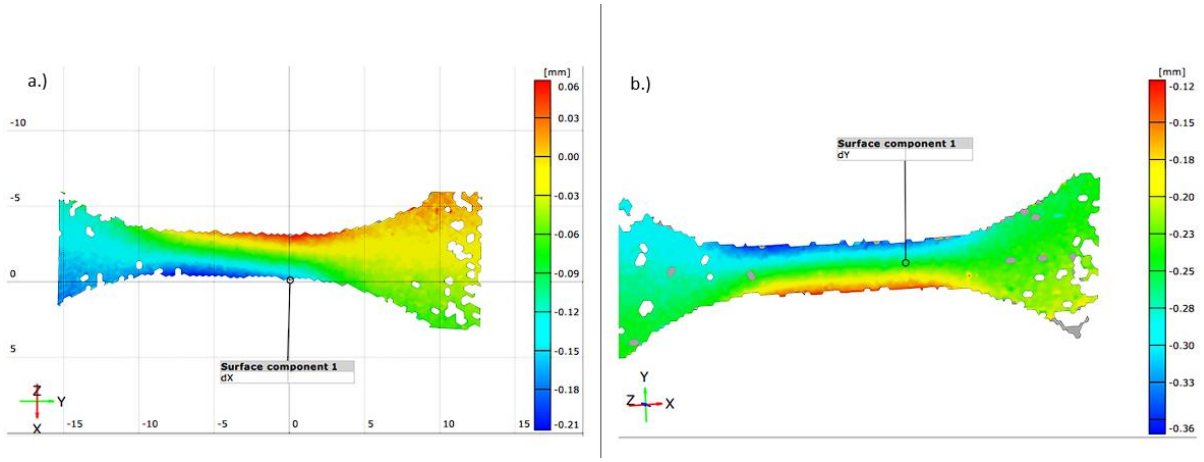


Figure 18: A.) Digital Image Correlation of Transverse Displacement Of 2.5% TiO_2 Sample. B.) Digital Image Correlation of Transverse Displacement Of 5% TiO_2 Sample.

Both images in Figure 32 were obtained in the frame before the sample breaks, where displacement across the sample is at a maximum. The 2.5% TiO_2 sample displayed a maximum transverse displacement of 0.27mm, whereas the 5% TiO_2 sample displayed a maximum transverse displacement of 0.48mm. This is above a 75% increase in transverse strain between the two composites. The normal strain difference between the two samples was just over 90%, demonstrating that the composites are uniformly deforming as expected. The deformation in the 5% sample provides insight into why the composite could withstand up to 5 MPa more resistance in UTS tests. An increase of over 75% in transverse strain would directly impact the sample's ability to withstand more force through plastic deformation comparatively. Although this was beneficial between the two samples, it is not what is expected from a nanocomposite with a higher loading percentage. A reduction in strain generally reflects a nanocomposite with a higher nanoparticle loading percentage. This assumes that the part has effective crosslinking between the nanoparticle and matrix and that no defects are caused during manufacturing. Therefore, based on tensile test results, it must be assumed that there is a transition between the 2.5% and

5% nanocomposites where the nanoparticle is no longer effectively crosslinking with most of the part.

4.3.3 Water Contact Angle

Contact angle analysis was performed to determine if the nanoparticles altered the surface interactions with liquid water. Eight different angles were measured for each different sample concentration. The average water contact angle for the control, 2.5%, 5%, and 7.5% TiO_2 resin by weight were as follows: 63.3°±3.4°, 66.9°±3.2°, 61.4°±1.7°, 62.8°±3.2°. All of these values obtained are statistically similar, utilizing an alpha value of 99% with a 15-degree of freedom t-test except for the 2.5% sample. The 2.5% sample has a statistically higher contact angle ($t=-1.99$, $df=11.32$, $p<.05$). Sample images are shown in Figure 19, depicting the results obtained for one of the droplets tested on each surface.

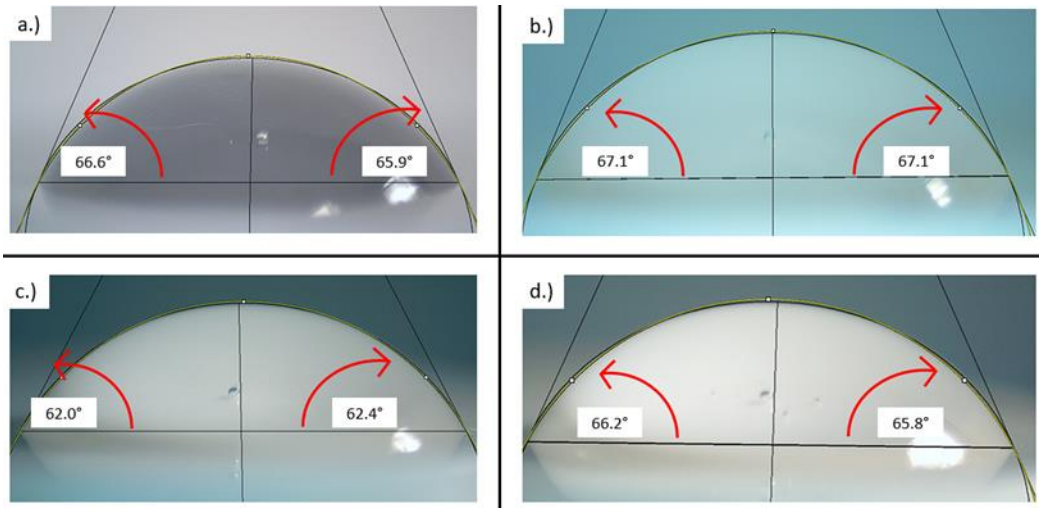


Figure 19: a.) Control Water Contact Angle. b.) 2.5% TiO_2 Water Contact Angle. c.) 5% TiO_2 Water Contact Angle. d.) 7.5% TiO_2 Water Contact Angle

All of the sampled surfaces display a hydrophilic reaction with the water. At the same time, this is not ideal for use cases in high moisture environments where bacterial growth is a

concern. However, it does offer several other advantages. Hydrophobic properties are not always desirable in the medical field when the object is being utilized in human or animal implants or aid devices. Hydrophobicity would cause the natural human fluids such as blood or saliva to react adversely to the printed parts and cause issues with items such as implants. Additionally, the surfaces sampled demonstrated consistent reactions with the water with standard deviations as low as 1.7°. Although the 2.5% sample is statistically different, the sample still falls well within the hydrophilic range and would need multiple other processes that increase hydrophobicity to be considered viable in an application that requires zero water adhesion.

When analyzing the modulus, the water contact angle gives insight into the results observed during tensile testing. The contact angle of the materials with the larger modulus trended upwards, while the lower modulus trended downwards. Although the values are statistically similar between the three tests, the 2.5% composite stood out similarly to the modulus data.

4.3.4 Glass Transition Temperature

The materials tested were an amorphous thermoset determined by DSC testing. The glass transition temperature was determined for all samples with two different cycles run on each sample with the control data shown in Figure 20. The average values for the control, 2.5%, 5%, and 7.5% specimens were 70.27° C, 70.29° C, 69.79° C, and 69.78° C. The 5% and 7.5% samples were statistically different, with a 0.01 p-value. The reduction in glass transition temperature is expected as the TiO_2 will increase the change in heat flow. This change was observed in both samples at the glass transition point.

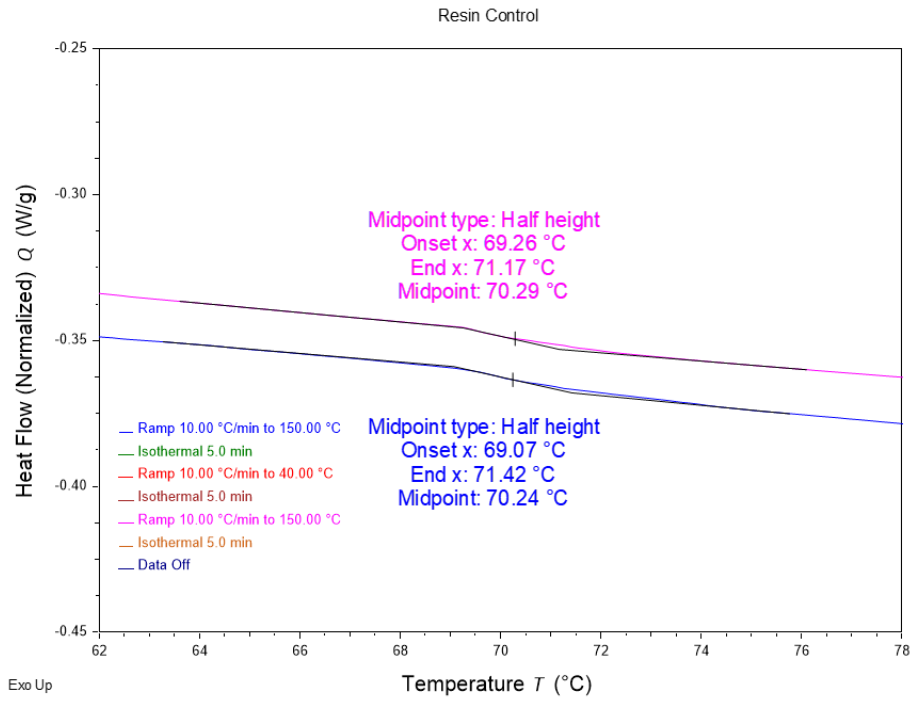


Figure 20: Glass Transition Temperature of Control Resin

While the composite resin did demonstrate a reduction in glass transition temperature, the average difference was less than 1° C. A change of this small should be negligible for nearly all use cases. The change in heat flow was also marginal at less than 0.05 W/g total at the glass transition stage for all samples tested. This confirms that the titanium conducts heat energy into the sample faster but not causing a significant difference in applicable use cases.

4.3.5 Abrasion Resistance

Abrasion tests were conducted to determine the change in wear statistics of the material. Each sample was ground against an abrasive pad at a constant speed in 30-second intervals for 12 cycles. All composite samples displayed increased abrasion resistance, with the 5% and 7.5% samples being significantly different, with a p-value of 0.01. The large standard deviation for the 2.5% sample, as shown in Figure 21, was due to the difference in performance between the two

tested samples varying drastically. Both samples performed better than both control samples but the low concentration of TiO_2 made for large differences in abrasion resistance at each layer.

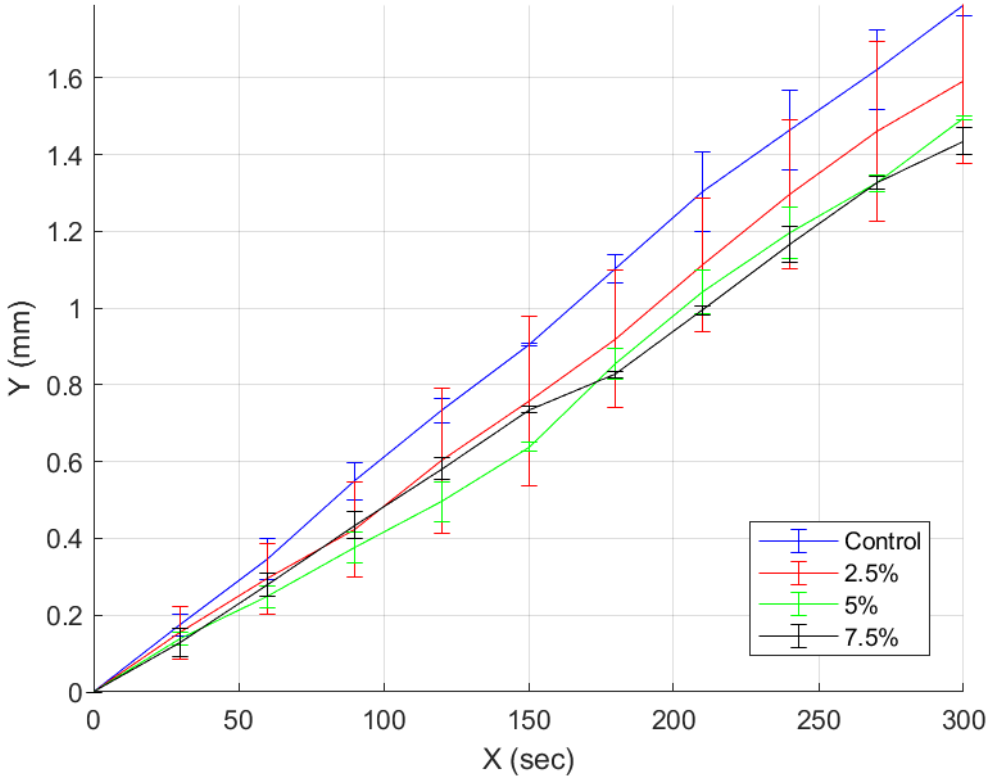


Figure 21: Abrasion Comparison of Control and TiO_2 Samples

Increased abrasion resistance pairs well with the intended use case of this nanocomposite, as it would last longer in high-use public environments. The linear increase in abrasion resistance with TiO_2 concentration verifies that TiO_2 is responsible for increased abrasion resistance. Additionally, this data confirms that while all samples were cured under identical conditions, the TiO_2 still formed enough bonds to the polymers to produce positive results at higher concentrations.

4.3.6 High Magnification Imagery

Two different types of imagery were obtained to understand better the samples' dispersion, loading, and surface quality. First, high-resolution optical imagery was obtained utilizing a Keyence-VHX7000 Ultramicroscope along with 3D and 2D scans of the surface topology. Secondly, a Thermo Quattro S field-emission environmental scanning electron microscope was utilized to provide high-resolution images above 30,000x. Samples were prepared in the same manner as the tensile tests to ensure accurate findings, with the only changes being that the SEM samples were coated with ≈ 4nm of iridium utilizing an EMITech K575X to ground the samples to the machine. The images taken can be viewed in Figure 22 with the topographic 2D image in 3b.

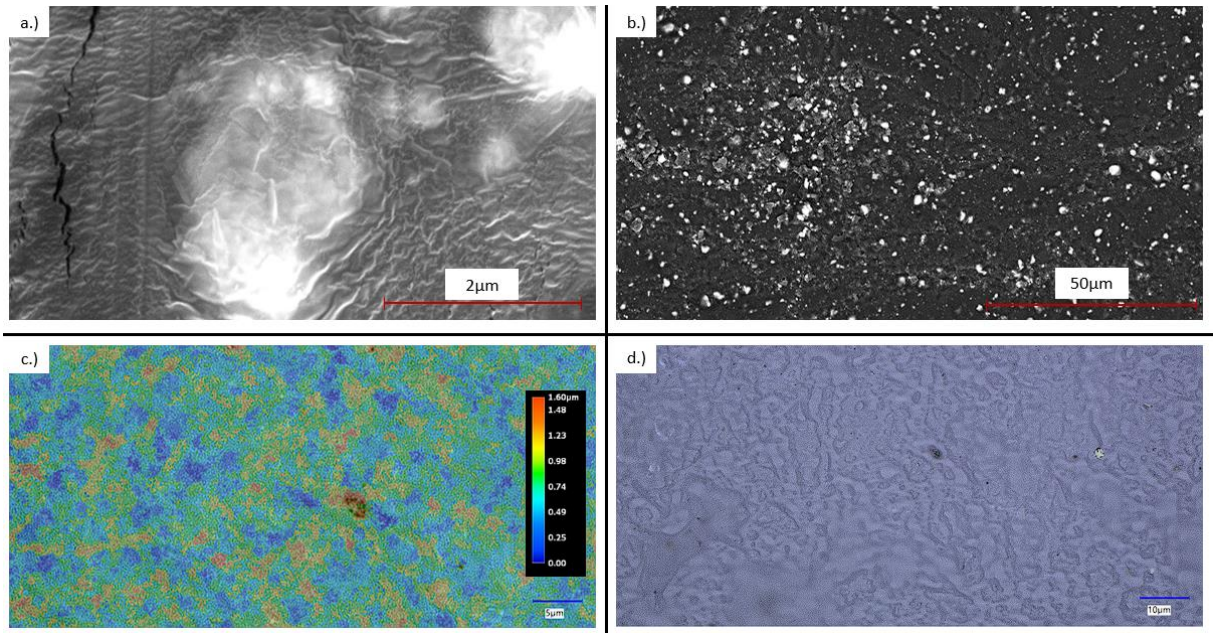


Figure 22: A.) SEM Image Of 5% TiO_2 Sample Using ETD Detector. B.) SEM Image Of 7.5% TiO_2 Using a Backscatter Detector. C.) Surface Topography Map Of 5% TiO_2 Sample. D.) Optical Microscope Image of Surface Features Of 5% TiO_2 Sample.

All the imaged surfaces consisted of the last layer of the print. This ensured that the images depicted layers similar to normal ones and did not have alterations due to the longer cure time or contact with the build plate. This also ensured that the topography data would resemble surface characteristics for any internal or side geometry produced during a print.

As SEM imaging degraded away the polymer when imaging, the best images able to be obtained were at just over 30,000x, as seen in Figure 36a. This image is of several agglomerations of TiO_2, along with several small nanoparticles in between the two agglomerations. With the particle size falling between 10-30 nm in diameter, the agglomerations present a makeup of approximately 7 to 20 different nanoparticles. The two sites in the upper right of the image are likely single nanoparticles as they measure approximately 30nm in size. These agglomerations and single nanoparticle sites are distributed across the entire surface of the samples, as shown in Figure 36b. The backscatter imagery shows a stark contrast between the TiO_2 and the polymer due to the elemental difference and helps highlight the dispersion pattern and agglomeration characteristics. As the 7.5% sample was the statistically weakest sample, large agglomerations, and voids are expected to be observed, assuming the hypothesis that the reduction in strength was due to manufacturing standards compared to composite loading. This phenomenon was observed in the 7.5% and 5% samples, where agglomerations comprised most of the composite, often located in large groups, as seen on the left-hand side of Figure 36b. These large agglomerations change the nanocomposite ratio throughout the sample creating an isotropic material with voids and defects due to a lack of successful crosslinking. Several results from the SEM testing demonstrated large amounts of voids across the 7.5% sample where nanoparticle agglomerations appeared to fall out or resin was left uncured. These voids often followed

patterns of appearing near or around the larger groupings creating large stress anomalies in the material when exposed to force.

These results tend to reinforce the hypothesis that the manufacturing process plays a more significant role in the final strength than the loading of the material, with all other variables held constant. Because the manufacturing process takes place in 25-micron increments, the opacity of the material regarding 405nm and UV light critically affects the final strength of the resin. Other studies support this hypothesis, where nanocomposite loading of pho-absorbing additives necessitated increased exposure time[103]. Additionally, as all samples are exposed to the same post-processing treatment, any decrease in light transmission due to increased loading would compound the negative effects caused due to incomplete curing. The TiO_2 appears to create a UV shield within the resin where the agglomerations block light from reaching the resin directly behind it, creating a void of uncured resin. This phenomenon would lead to several mechanical features, including decreased UTS, increased standard deviation, and increased maximum strain. The decline in UTS would be expected as the voids in the material would lead to suboptimal results compared to a 100% cured control resin. The voids would also reduce the interfacial bonding between the resin and nanoparticles. These issues would also increase standard deviation as the material would be acting isotopically, with the failure point being determined by the location with the most agglomerations blocking UV light compared to a failure of the resin or a failure of the TiO_2 resin bond. Lastly, the maximum strain would be expected to increase compared to a properly bonded nanocomposite as the failure rate of a successful composite would be determined by the failure of the interfacial bonding of the nanocomposite and the matrix resulting in a lower standard deviation from the normal polymer.

These attributes were observed, determining that the 5% and 7.5% nanocomposites were overloaded for the prescribed cure times.

Further findings utilizing the optical microscope and 3D surface modeling helped demonstrate the curing process of the material at a layer-by-layer level. Analyzing the image in Figure 36d shows that the surface of the composite follows very natural topographic geometries. These geometries likely relate to the flow of the material right before curing, along with their interaction with the hydrophobic print surface in which they sit. An important factor in these images is the overall surface roughness of the sample. Out of all samples modeled, the largest deviation in surface roughness was 4.3µ, with many samples falling under 3µ in change. With a single layer consisting of 25 microns, the most deviation in the final surface was just 17.2% of that entire layer. This was recorded on a 5% sample where SEM has already depicted that the surface is imperfect due to nanoparticle fallout and uncured resin. Therefore, the curing process can cure the bottom 20% of a layer faster than the other 80% between that bottom 5µ and the build plate. To further cause issues in the composites, the TiO_2 was blocking UV light, creating an uneven gradient of light that would reach the build plate. This created a micro anomaly on each layer where the top of the layer would be most cured and the bottom would be least cured, with pockets inside that layer potentially being completely uncured due to light block. This also would explain why the control resin performed so well as it is a clear resin, so the effect of a gradient cure would be negated as the light could still pass through once the first 5µ began curing. The proposed solution to this problem would be to decrease the layer height to a minimum of 5 microns or less. While the machinery used can have a minimum layer of 10µ, the printing time would exponentially increase to the point of other issues likely occurring. As printed, a set of tensile samples took just over 54 minutes; utilizing a 50µ layer height, the print

time would increase to over 4 hours and 22 minutes. This is also not considering that the exposure time would likely need to be increased for some of the higher-loading composites. While this is possible and prints of this time were successfully performed, it reduces the practicality of the printer, with useful items such as prosthetic hands taking nearly a week.

4.4 Conclusions

By finely controlling the entire manufacturing process, it was discovered that the cure rate is directly related to the nanoparticle concentration of a given nanocomposite. By utilizing a curing parameter that is adequate for all resins, including control, the final composite will likely lack mechanical strength due to a lack of proper curing. For the tested parameters, it was determined that the optimum nanoparticle addition fell between 2.5 and 5 wt%. Further, research should be conducted utilizing the same process but with longer cure times to determine if the reduction in UTS compared to the matrix was due to a lack of compatibility between the polymer and nanoparticle or a lack of crosslinking due to a lack of energy during the curing process.

CHAPTER 5: FLEXIBLE CNT NANOCOMPOSITES

5.1 Introduction

With the success of the previous studies, further research into more advanced nanoparticles such as CNTs was warranted. CNTs are often considered one of the most promising nanoparticles due to their incredible strength-to-weight ratio and high aspect ratio. These properties make them fantastic candidates for improving photocurable-based AM manufacturing, but several large challenges must be overcome.

The high aspect ratio and Van Der Wall forces associated with CNTs often make it difficult to disperse the nanoparticle properly in viscous fluids. Additionally, the UV absorbent properties of CNTs will cause manufacturing complications as the additive will absorb the same energy used to cure the material. This study will analyze these challenges as CNT is used in a low concentration to produce an electrical resistive flexible sensor for human motion detection.

5.2 Materials and Methods

A photocurable thermoset matrix and carbon nanotube nanoparticle were combined by a weight concentration of 0.25% filler to the matrix to synthesize the novel nanocomposite. The matrix thermoset was a market-available Superflex resin from 3DMaterials. The multi-walled CNTs were 50-90 nanometers in diameter with an aspect ratio above 100 from Sigma Aldrich. The nanocomposite was synthesized by mixing the two materials in a planetary Thinky AR100 mixer for 10 minutes in 70mL increments. The final temperature of the material after mixing was 37° C. A Mars 2 Pro from Elegoo manufactured the printed samples with custom cure settings.

To regulate the viscosity of the resin during the manufacturing process, a custom convection-based heating chamber was built to hold the entire printer and resin at 40° C.

Testing samples were printed following ASTM D638 Type V dimensions as the maximum size sample could be printed in all directions of the build plate. These printed samples were utilized for tensile, fatigue, and resistance testing. Data collection for these results was acquired through an Intron 5969 with a 5kN load cell. Resistance data were collected by a Hioki RM3545 resistance meter. Tensile tests were performed at a 10 mm/min extension rate and fatigue testing at 20% strain/min.

The manufacturer suggested cure times for the virgin material utilizing 50-micron layer heights were 20 seconds for the bottom layers and 9 seconds for all remaining layers. With a 50-micron layer height, the tested print settings were 40 seconds for the bottom layer and 7.5 seconds for all remaining layers. An additional key difference was that the printer was placed inside a custom convection heated chamber at 40° C to help control resin viscosity and degree of cure. This increased manufacturing temperature allowed for a faster rate of cure which is demonstrated during the normal cure. The increased bottom cure was added as the increased chamber temperature also reduced part stiffness once printed and, therefore, more stress on the build plate and part mating surface. This was increasingly evident on prints with large aspect ratios, where they would often fail due to the extreme flexure of the part relative to its starting print location. To prevent this from happening, increasing the area of the bottom of the part through a raft or increasing normal layer time is recommended.

Once the part was finalized printing, it was removed from the heated chamber and cooled completely for removal. It was then cleaned with isopropyl alcohol, the recommended solvent for the matrix material. Once cleaned, the part was submerged in a glass beaker filled with water

and placed into a curing oven with a 405nm light source and turntable at 60° C. Next, the parts were submersed in water, which aided in dispersing the heat generated during the exothermic post-curing process and reduced part warp. All samples were cured for a total time of 60 minutes.

Parts intended for strain gauges were then modified by gluing copper strips on the ends with a conductive paste. This ensured that the resistance would not change due to the probe connection but due to the strain of the sample. This interface was extremely important as a bad electrical connection could lead to resistance values up to 4x that of the printed sample alone. The final solution for a flexible conductive epoxy was a mixture of PDMS and CNTs at a 2% weight concentration. This ensured that the resistance due to the PDMS epoxy would be far less than the printed sample as it had 8x the amount of CNT content.

The viscosity of the material was tested by utilizing a digital rotary viscometer with the material placed on a hot plate. An NDJ-9S rotary viscometer was used with data logging to capture the viscosity of the material as it was slowly brought up to printing temperature. As the heating process was performed on a hot plate instead of inside the oven for this test, it took several minutes for the material to reach thermal equilibrium, as noted in the manuscript.

5.3 Results and Discussion

Several mechanical, thermal, and rheological tests are performed to properly characterize and demonstrate the practical uses of this novel nanocomposite and manufacturing method. First, the material's tensile, modulus, and max strain values are investigated to determine its maximum working conditions. Second, fatigue tests are completed to demonstrate its long-term durability and resistance response. Third, viscosity testing is performed to identify the effect of the printing

chamber on the material. Fourth, samples are analyzed under a differential scanning calorimeter to determine the glass transition temperature. Optical imagery aids in identifying CNT dispersion and alignment. Lastly, a practical application is demonstrated for use in human-based sensors.

5.3.1 Tensile and Strain

A total of 12 samples were tested to determine tensile stress, max strain, and modulus. The average stress, strain, and modulus are 1.74±0.233 MPa, 2.35±0.147MPa, and 0.737±0.062 MPa, respectively. The samples' results are graphically presented in Figure 23 with standard deviation error bars added. Figure 1b demonstrates the extreme elongation capabilities of this material as it can stretch up to 135% of its original length on average. As the material is a flexible thermoset, the importance of tensile strength for this application is not critical.

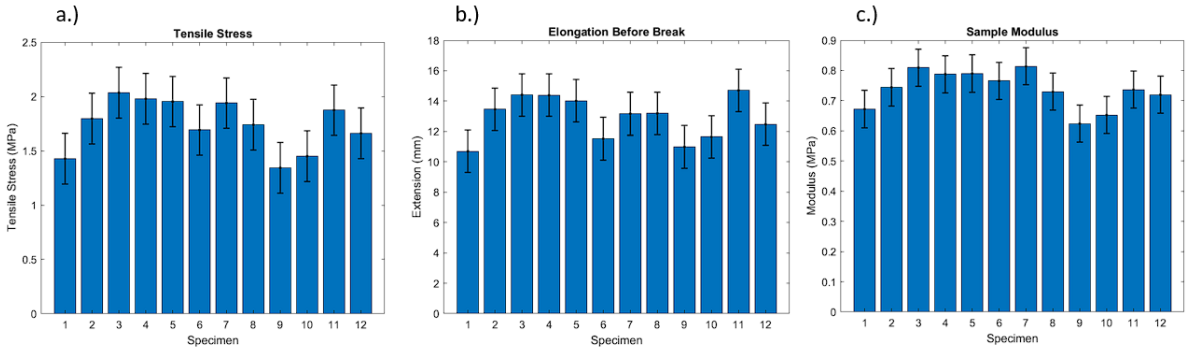


Figure 23: a.) Tensile test results of ASTM D638 Type V samples with standard deviation plotted. b.) The maximum elongation of the sample before failure. c.) The Young's modulus of each sample

Compared to the virgin matrix material printed at room temperature with standard cure settings, the tensile strength rises to 5.5 Mpa, but the elongation at break drops to only 80%. Therefore, increasing the maximum strain before failure is more desirable to incorporate this material into a human-mounted sensor than increasing tensile stress. The changes in the

manufacturing of the material also likely affected these changes as the degree of cure was changed, and post-processing parameters were altered.

5.3.2 Fatigue

To properly characterize and demonstrate the ability of this material to withstand implementation into high-cycle equipment, fatigue testing was conducted. To complete this testing, a sample manufactured for resistance measurement was used to help measure the change in resistance throughout several hundred cycles. The sample tested was set up to run a continuous cyclic test of 0-20% strain for 250 cycles. The resistance over time, stress over time, and stress-strain curves can be seen in Figure 24.

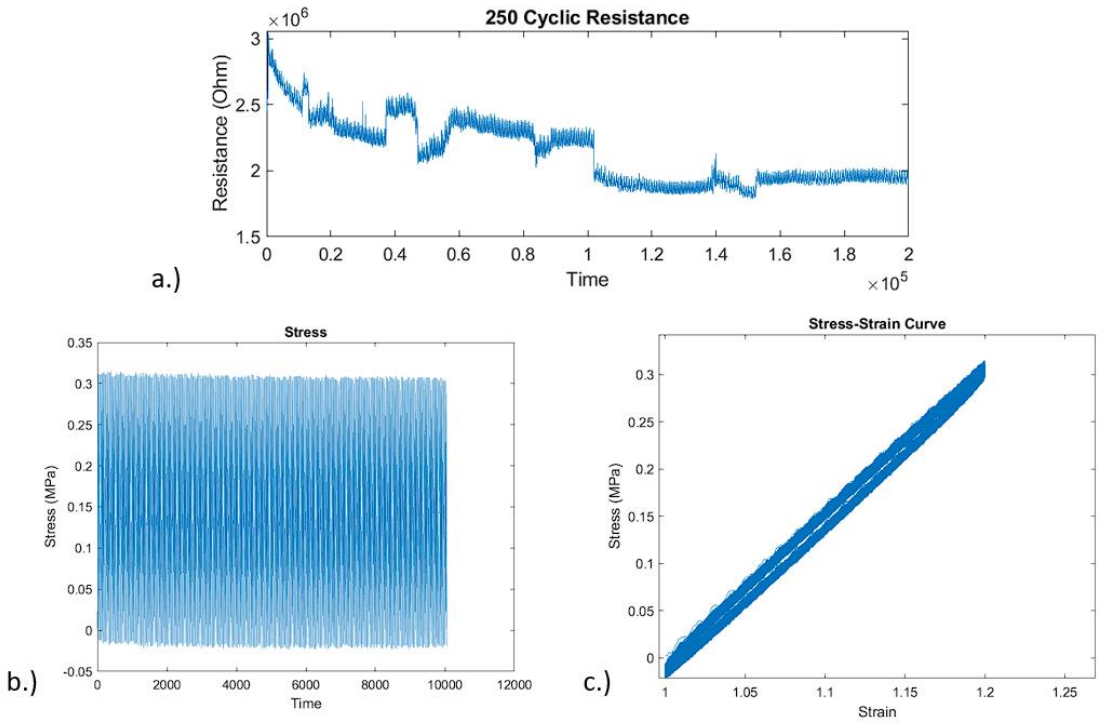


Figure 24: a.) Resistance of sample over time. b.) The stress of the sample over time c.) Stress-strain curve of a sample of all 250 cycles.

The maximum strain was held constant at 20% for all cycles, and the load had no maximum. As observed for all cycles, the stress of the sample stayed nearly the same with no degradation of strength. Notably, the resistance response of the sample became more stable after about 125 cycles and held constant for the remainder of the test. The total resistance decreased, and the response became very predictable and linear. This is likely due to the sample warming up as it cycled and reached equilibrium.

5.3.3 Resistance Mapping

An important characteristic of a highly flexible strain sensor is its ability to clearly define different amounts of strain through different resistance responses. To model this behavior, a short cyclic test was set up with varying strain levels. Then, the strain was increased in a step-like function until the sample failed. Finally, the data were analyzed in Matlab utilizing a moving average smoothing technique and local extrema function, as seen in Figure 25c, to demonstrate how these sensors' output could be analyzed in real-time and movements automatically characterized.

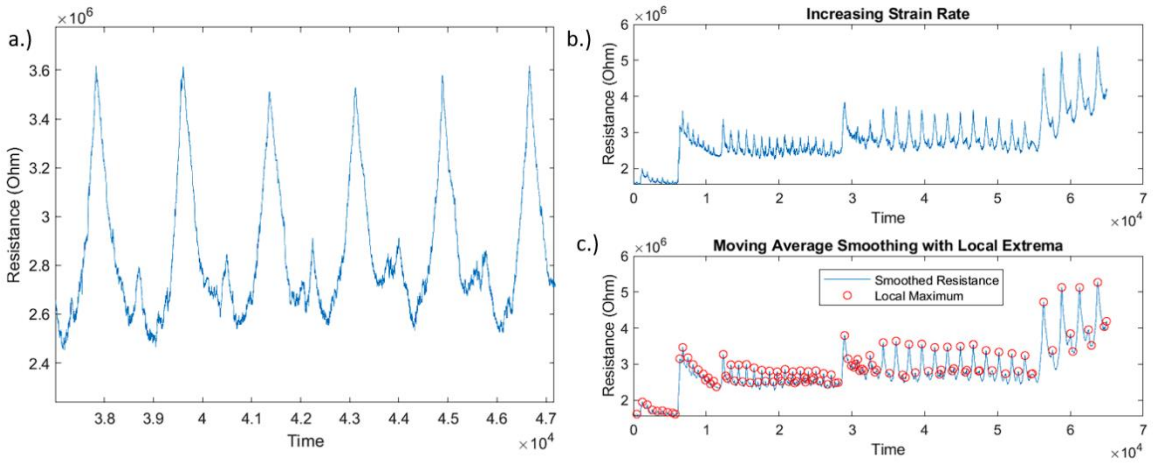


Figure 25: a.) Several cycles at 70% strain. b.) Raw data of resistance at multiple different strain values. c.) Smoothed data with local extrema automatically detected.

The gauge factor for the provided samples is around one at or under 30% strain. Above 30% strain, the gauge factor begins to fall off as the resistance response is not completely linear with the strain of the material. However, the resistance response does increase notably enough, though it can be easily picked up by software and can be differentiated through algorithms for more precise location information.

One of the main issues with resistance testing for this material was the interface between the copper plate and the sample. Connections were obtained with resistance values around 500-600 kilohms at 0% strain through testing. These connections were often obtained by clamping the material together instead of using an interfacing adhesive. These results demonstrated that the nanocomposite base resistance value was four to six times less than displayed during the cyclic testing. Investigating better ways to obtain this interface would help increase the gauge factor of the material, as there would be less loss of resistance due to the interfacing connection. This is later proved in section 2.7 with the practical applications provided.

5.3.4 Viscosity

Other researchers have demonstrated the ability to increase in-situ curing through temperature modulation of the resin[79]. This was attributed to the resin's decrease in viscosity and energy needed to cure during the exothermic reaction. However, with the addition of CNTs, which have been shown to absorb UV light, the need to modify the degree of cure was required to obtain reasonable print times[104, 105]. To achieve this change in the degree of cure, the nanocomposite and printer were heated to 40° C. This led to a nanocomposite with a viscosity nearly half that of the resin at room temperature, with much better flow characteristics, as shown in Figure 26.

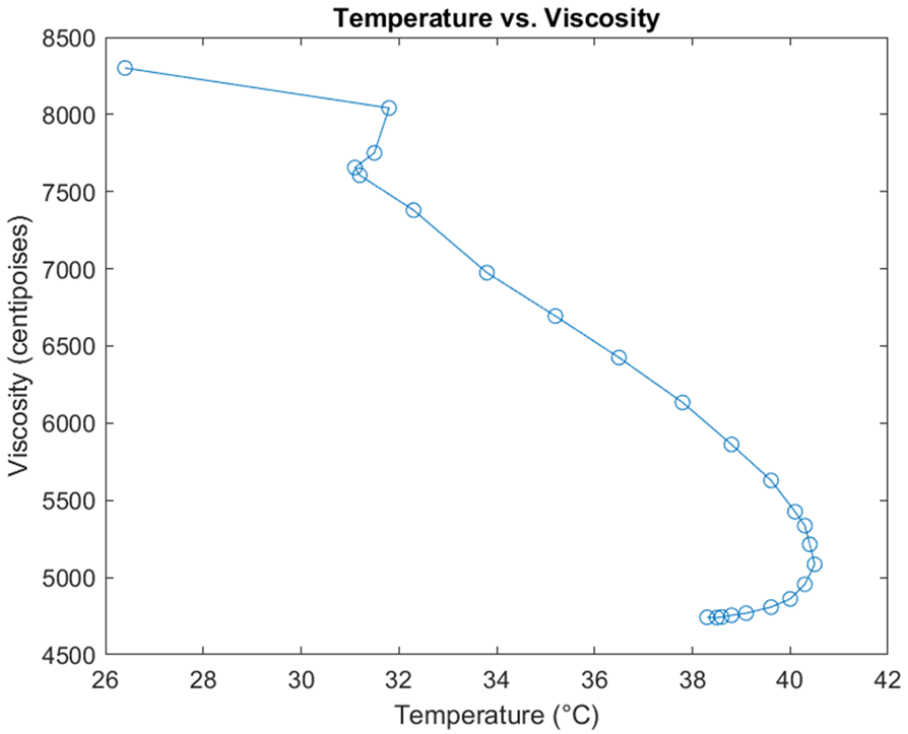


Figure 26: The viscosity of resin material as it is heated to printing temperature.

As the resin approached its operating temperature, it took several minutes for the viscosity to equalize as the material reached thermal equilibrium. The average viscosity recorded at operating temperature was 4742 centipoises. This is still relatively high for resin printing; therefore, future research studies should investigate if printing can continue at higher temperatures. In addition, finding an equilibrium between in-situ print rigidity and reduction in the cure rate would be required to allow for fine detail printing without print failures. At the current temperature and viscosity of the material, printing could be completed at a rate higher than recommended by the resin manufacturer. If larger CNT loadings are desired, the temperature would likely need to be increased to continue to print at the same rate.

The planetary shear mixer is the other important process that relies on the viscosity of the material for this novel nanocomposite synthesis. Properly dispersing the CNT and reducing the matrix viscosity is beneficial; therefore, mixing for a long duration to lower the viscosity to that of the printing viscosity would be ideal. This was achieved by mixing the material for different intervals until the final nanocomposite was removed from the mixer at operating temperature due to friction-based thermal gain.

5.3.5 Glass Transition Temperature

Properly characterizing the material's glass transition temperature would allow the materials to be used in a thermal cleaning scenario for medical applications if it is above 135° C. Differential scanning calorimetry was performed on several different samples to determine the average glass transition temperature of the material. The material was also determined to be amorphous. The glass transition temperature was determined utilizing a half-height midpoint calculation, as shown in Figure 27.

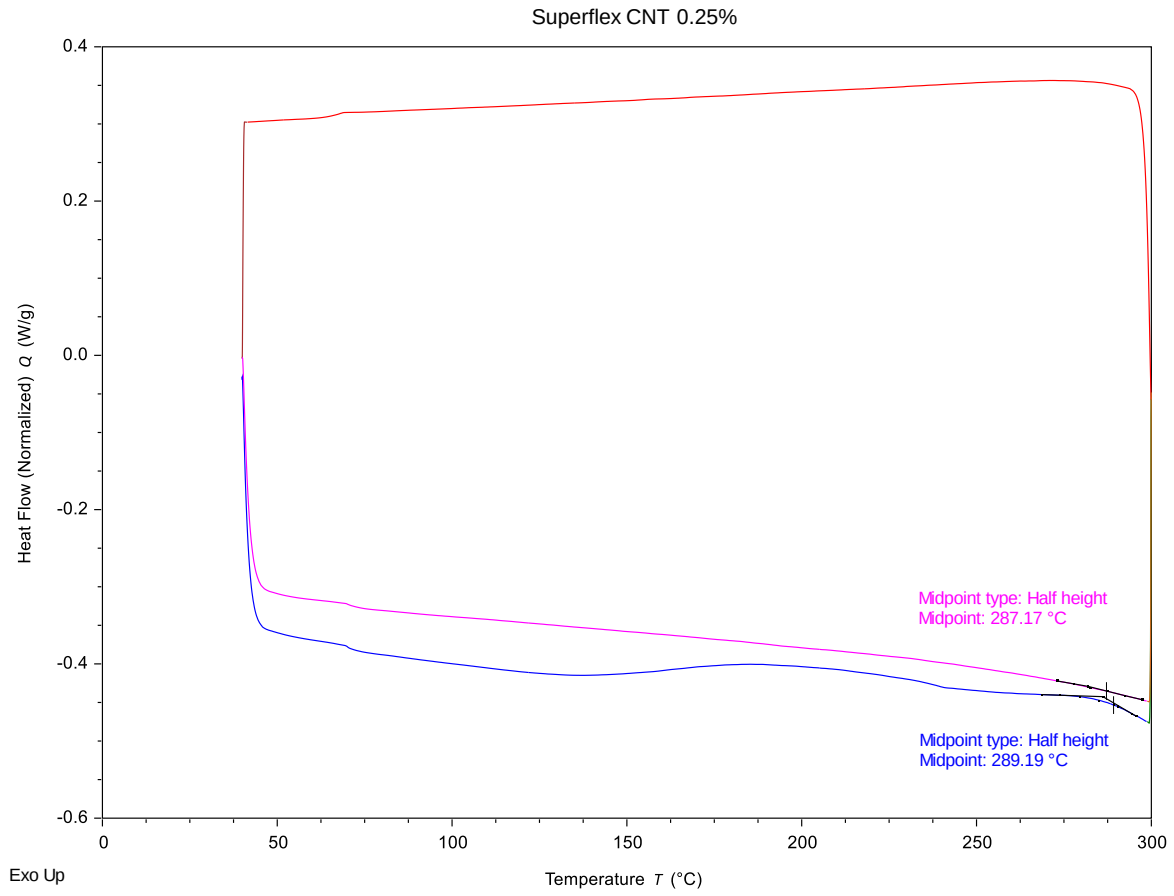


Figure 27: Normalized heat flow compared to temperature with glass transition temperature determined using a half-height midpoint calculation.

The average glass transition temperature recorded across eight different readings was 288.15° C with a standard deviation of 1.22° C. This places the polymer well above the temperature needed for thermal cleaning systems often used in the medical field and makes it a strong candidate for prosthetic interfaces and other medical sensing technologies. An important note is that the samples were run through two cycles, and the glass transition temperature on the second cycle was often 1 degree less than the first. This is likely due to some sample degradation during the first cycle, changing the heat flow required for the second cycle.

5.3.6 High Magnification Imagery

A Keyence VHX-7000 ultramicroscope was used to image the sample's surface and break location. This allowed for the characterization of CNT dispersion, entanglement, and pullout. The material's surface was also mapped in 3D, as seen in Figure 28, to provide insight into the surface finish, defects, and tear-out.

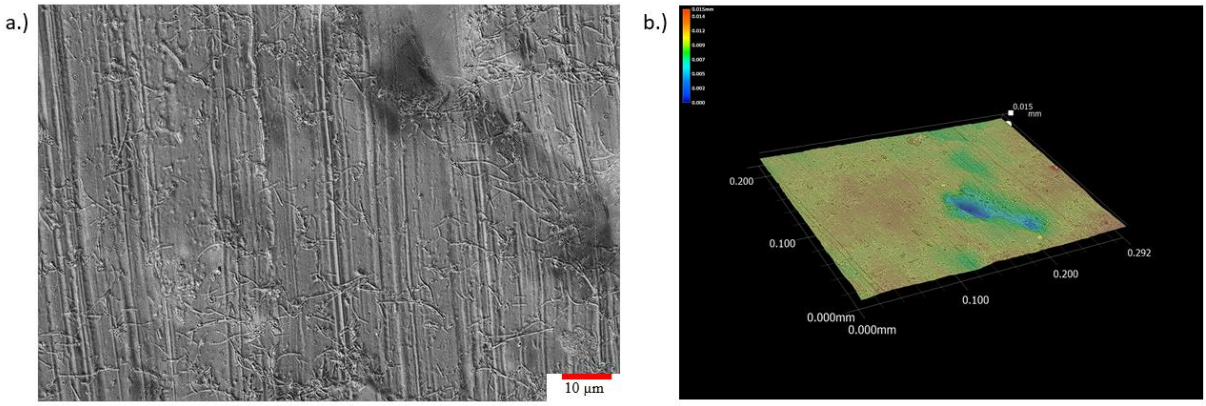


Figure 28: a.) 2500x magnification of as printed surface with CNT dispersed throughout. b.) The 3D model generated of the sample demonstrating surface finish

These images reinforced the decision to utilize planetary shear mixing as the dispersion technique, as all images showed an equal dispersion of CNTs. CNT entanglement also appeared minimal, with many long strands of CNTs above 10 microns in length visible. The supplier states an aspect ratio above 100, and the image results reinforce that the CNTs remained unbroken as their aspect ratio was often in the 200 range. As expected, there is no CNT alignment in the x or y-axis specifically, which should exhibit isotropic properties in that plane. However, particle alignment was noted in the tear-out samples parallel to the x-axis shown in Figure 29. This is likely caused by the printing mechanism pressing down on the nanocomposite of each layer and helping the CNTs lay flat. This would increase the strength of the material when pulled in the

XY plane along the z-axis. This is very apparent in the 3D fracture image in Figure 7a, where very few CNTs are running parallel to the surface, and instead, locations of CNT pullouts along the main fracture lines are evident.

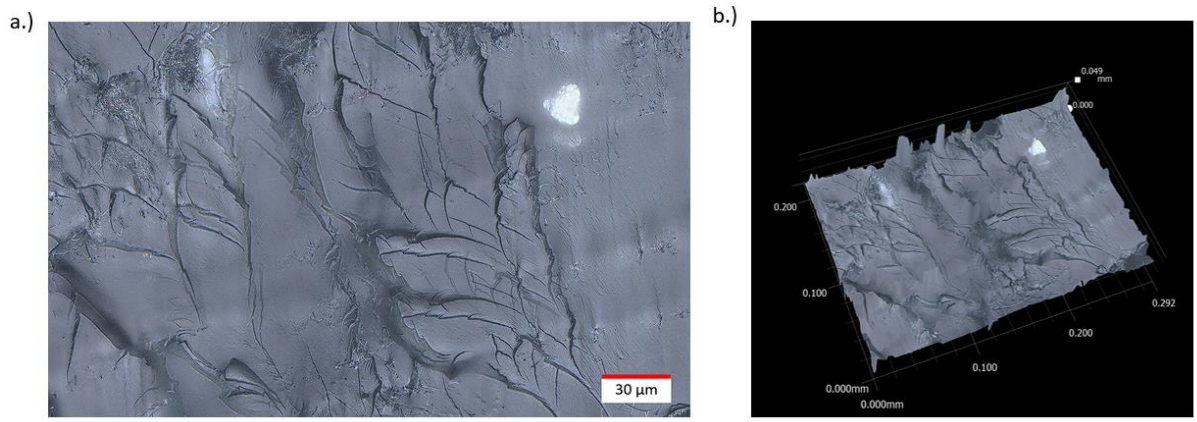


Figure 29: a.) High magnification stitched image of CNT tear out across sample fracture. b.) 3D model of the sample fracture plane.

There also appear to be larger CNT agglomerations based on the printed layer level when analyzing the xy cross-section from the z-axis perspective. While CNT is prevalent on all layers, further investigation would need to be conducted on the effects of CNT settlement over time, leading to varying volume fiber ratios for longer prints. The top left of Figure 7a most prominently displays the large CNT agglomerations that appear to transmit most of the load during tension. The major fracture running down the middle of the image also has multiple locations of fiber pullout evident. Further investigation into the manipulation of layer heights should be conducted to determine the effect of the printing system's mechanical motion on aligning CNTs in the XY plane.

5.4 Practical Applications

While the material has shown several favorable characteristics for adaptation into the medical industry, it must still perform adequately when incorporated into human motion measurement systems. To analyze its capability of being a skin-attached strain sensor, a printed part would attach to a finger and help measure the flexion and extension of the proximal interphalangeal joint. This application aimed to determine if the hand was attempting to grip something or was loose and relaxed. Matlab code automatically smooths the raw data and determines when the finger was extended or under flexion based on local extrema, as shown in Figure 30.

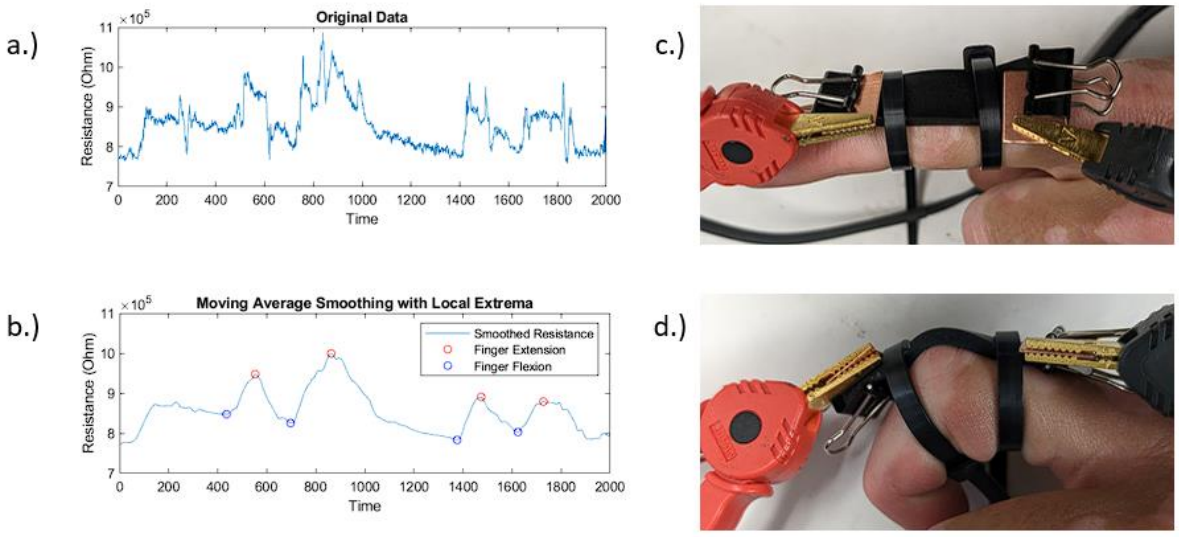


Figure 30: a.) Raw data from the resistance meter. b.) The Matlab modified data with key points automatically determined. c.)Finger under extension with a mounted sensor. d.) Finger under flexion with a mounted sensor.

The finger flexion amount can be easily determined by the first two peaks in Figure 8b. The finger was fully bent inward, whereas the finger was only under 50% flexion in the second

two peaks. As the sensor is mounted on a moving object with lots of microstrains, the data requires cleaning for accurate motion detection. For this scenario, a simple moving average was applied where the window size could be easily changed depending on the sensitivity of the resistance meter. Additionally, as the parts are 3D printed, each sensor can be custom designed for the end users' dimensions. As shown in Figure 8c, the printed sensor was designed to fit the user's finger joint with enough excess for resistance meter measurements. The only part of the sensor under flexion is the center of the sample between the two attachment points; therefore, the overall strain of the sample remains very low. This is ideal as the lower the sample's strain must undergo, the longer the lifespan of the sample.

The tested specimen's resistance meter and sample interface were pressed on a copper plate. This allowed for a better electrical connection, with resistance values of about 25% of the values in the fatigue tests.

Final application prints could incorporate the wire or copper plating inside the print for improved, durable connections. This can be achieved by modifying the printing code to pause at a certain layer and increasing the layer height to 100 microns. A copper plate could then be placed on the part and fused inside during the next layer. Another possible method would be to utilize a low-resistance thermoplastic and press the copper plates onto the samples with pressure and heat.

5.5 Conclusions

This work details a novel flexible nanocomposite's synthesis, manufacturing, mechanical, and electrical testing. The material synthesized has an extremely high maximum strain of 135% and has proven durable over high cyclic testing loads and lower strain values. Furthermore,

adding CNTs at only a 0.25% weight loading concentration has demonstrated a clear ability to deliver reliable strain sensing results. The gauge factor for several tested samples was 1, with a detectable and predictable response for motion through the entire strain range. The manufacturing process was modified to allow quick printing comparable to virgin photopolymers without adding an extra photoinitiator. The viscosity of the nanocomposite responds well to raises in temperature to allow for easy flow and detail retention during the printing process. High magnification optical imagery was utilized to demonstrate the cause of anisotropic characteristics of the printed samples where CNTs aligned in the xy plane. This allowed for increased tensile results when pulling along the z-axis. Lastly, a sample was custom printed to demonstrate the part's ability to be used as a skin-attachable strain sensor for detecting human motion. A Matlab code was developed to automatically smooth and detect changes in the data to highlight different points of motion. Future considerations for this work would be reducing layer printing height and increasing in-situ cure temperatures to better align the CNTs while increasing part strength. Additionally, this material would be a strong candidate for pneumatic-powered smart actuators as printed samples were air and watertight, and motion could be controlled through inflation. Overall this novel nanocomposite demonstrates the ability to use low-cost resins and manufacturing machines to develop customized strain sensing systems applicable to the medical field.

CHAPTER 6: STRUCTURAL REINFORCED CNT NANOCOMPOSITES

6.1 Introduction and Objectives

This research study aimed to determine an optimized manufacturing process for structurally reinforced CNT nanocomposites utilizing a DLP printer. Previous work demonstrates many challenges associated with properly manufacturing UV-cured nanocomposites in a traditional photocurable printing system. To solve several of the unknowns, this work was designed to run through multiple tests while changing different manufacturing variables to determine the effect on the final nanocomposite. Several samples were manufactured for each run of variables and compared against each other.

The success of the previous research utilizing CNTs in elastic polymers to create high-strain sensors led to this experiment's goal to be designed around ultimate strength increases using a rigid polymer with a high glass transition temperature compared to most common thermoplastics. Other published research has found that incorporating CNTs into photopolymers has increased fracture strength and ultimate tensile strength as high as 40% of the base resin[11, 106, 107]. This project aims to meet or exceed those results by manipulating several key manufacturing characteristics, including in-situ cure time, post-cure time, and CNT concentration.

Two key parameters being observed are in-situ cure time and the effect of temperature on printing. It has been shown that both light intensity and ambient temperature play a major role in the crosslinking reaction of commercially available photopolymers[108]. The light intensity can be controlled by increasing the cure time or decreasing layer thickness for our application. Ambient

temperature can also be controlled by external environmental control or increasing cure time, as crosslinking is an exothermic reaction. This is important as adding CNTs can reduce the curability of the matrix as CNTs absorb UV light[109]. Increasing light intensity is often required with CNT concentrations as low as 0.3 wt% [70]. This study aims to reach CNT concentrations as high as 1 wt%.

6.2 Methods and Materials

To properly test extreme cure conditions on the novel nanocomposite, a DLP printing system was utilized as it would not suffer from the common ailment referred to as elephant's foot, where the final model is oversize in the x and y dimensions due to light leak around the LCD. The DLP printing system uses mirrors to only reflect the needed shape onto the resin vat, allowing for extreme exposure times without losing part geometry. To modulate temperature during the printing, a custom heat box was designed to hold the entire printer and material at a consistent temperature with a forced convection heating element. Post-curing was performed inside an oven where the temperature could be raised above 80° C.

The matrix material of choice was a commercially available high-temperature photopolymer from Phrozen labeled TR300. The provided specifications of the resin can be referenced in Table 4. Mechanical testing to determine UTS, elongation at break, and modulus will follow ASTM D638 standards.

Table 4: TR300 Mechanical and Thermal Properties

Property	Value
Ultimate Tensile Strength	32 Mpa
Strain at Break	2%
Youngs Modulus	1857 MPa
Glass Transition Temperature	220° C
Heat Deflection Temperature	190° C

A total of 8 different runs were designed to focus specifically on in-situ cure time, CNT concentration, and post-cure time. Temperature, layer height, and post-cure temperature were constant for these eight runs. The specifications for each run have been detailed in Table 5. It should also be noted that there was an increased bottom layer cure time for each of the sample sets, with the 60-second in-situ cure time having a 180-second bottom layer cure time for the first eight layers and the 180-second in-situ cure time having a 240-second bottom layer cure time for the first eight layers. All runs were mixed in a planetary Thinky AR-100 mixer for 10 minutes.

Table 5: Manufacturing specifications for each different nanocomposite sample set

Run #	Post Cure Time	In-Situ Cure Time	CNT Concentration
1	15 min	60 seconds	0.5 wt%
2	15 min	60 seconds	1 wt%
3	15 min	180 seconds	0.5 wt%
4	15 min	180 seconds	1 wt%

5	60 min	60 seconds	0.5 wt%
6	60 min	60 seconds	1 wt%
7	60 min	180 seconds	0.5 wt%
8	60 min	180 seconds	1 wt%

The printer had a light transmittance value of 92% and a rated power of 15 watts. An even energy reading of 3.052 mW/cm^2 was observed across the build surface. The in-situ curing temperature was set at 50° C for all tests. This value was decided on by running multiple tests until no failures were present during the printing process. Most failures occur during the 1 wt% CNT concentration, so the in-situ cure temperature could likely be lowered for the 0.5 wt% samples. All samples were post-cured underwater at an ambient temperature of 80° C.

A minimum of 3 samples were created for each manufacturing technique and followed ASTM D638 Type V design constraints. An Instron 5969 was utilized with a 5kN load cell for force and strain measurement. All samples were pulled apart at a constant rate of 1mm/min following the ASTM recommendation.

6.3 Results and Discussion

This study specifically focuses on the samples' manufacturability and mechanical results. There will be a qualitative discussion about the manufacturing defects and obstacles for each manufacturing set, along with quantitative results for the tensile results.

6.3.1 Manufacturing

The manufacturability of the samples varied greatly based on the in-situ cure settings and the CNT weight concentration. To determine a baseline of cure characteristics, a custom system

was designed and manufactured to measure the rate of cure of base resin materials. The apparatus utilized an LED matrix light source of 405nm and a light intensity meter tuned to 405nm. Using carbon fiber thermoplastic, the system was manufactured to absorb as much UV light as possible. It would then expose the desired material to the light and pick up the reflected light off the surface. The one downside to this apparatus was that it only worked with resins that did reflect some amount of the UV light. Any nanocomposite with higher CNT concentrations could not be quantitatively measured. This device was therefore used to determine the curing parameters of the base matrix material at room temperature and determine the remainder cure setting based on those values.

The rate of cure test results is below in Figure 31, where it was determined that a complete cure was reached at 60 seconds. This value was used as a baseline for the shorter exposure time for the testing. This test was also performed at room temperature, whereas the samples were printed at 50° C. The test sample also rose in temperature by over 5° C during the cure test below. While this curing mechanism could not be reliably used to deliver a rate of cure results for higher concentrations, CNT nanocomposites could be used to determine maximum layer thickness before all of the UV light was absorbed or blocked by the top cured layer. The 1 wt% CNT nanocomposite was used for this test as it would be the most difficult to cure. The material was exposed to UV light in excess of 10 minutes, and the final cure depth was determined to be 125 microns. This reinforces the design decision to run all tests at a layer height of only 25 microns.

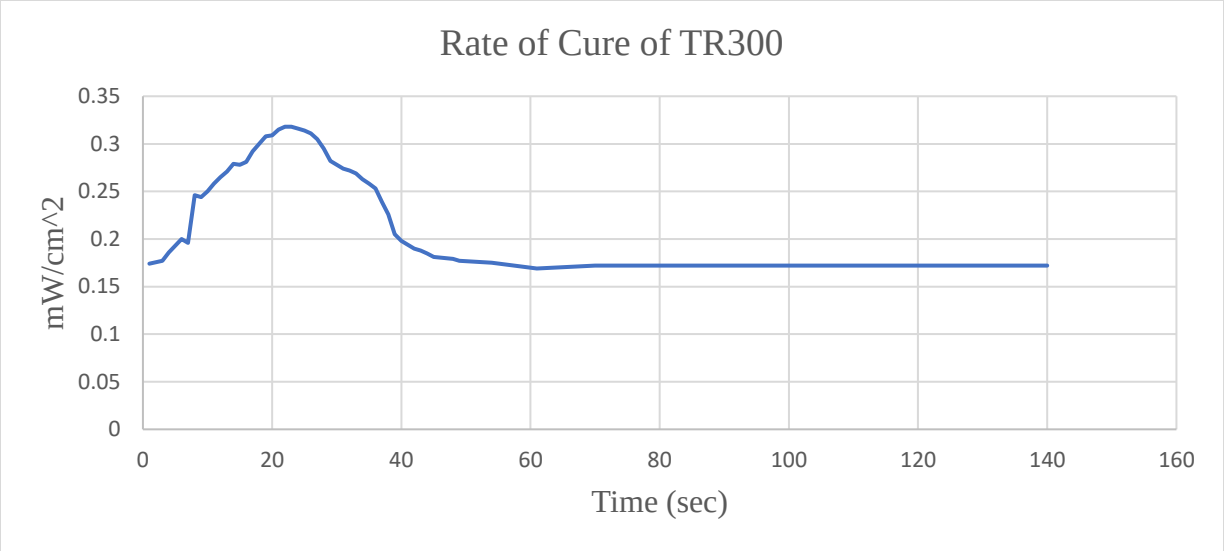


Figure 31: Rate of cure of commercially available TR300 resin.

The first set of tests was performed at the shorter in-situ cure time of 60 seconds. These tests printed as expected, with most samples having very few defects or surface imperfections due to the cleaning process. Surface defects were more apparent in the 1 wt% samples, as shown in Figure 32a. This is where the viscosity of the resin plays a large role in the ability to manufacture consistent samples with low layer heights. As the resin needs to reflow between layers to coat the bottom sheet, any increase in viscosity properly will raise the probability of inclusions forming during the printing process. The elevated chamber temperature helps alleviate this, but there does reach a point where modifications to the matrix material through the addition of plasticizers or photoinitiators may be required.

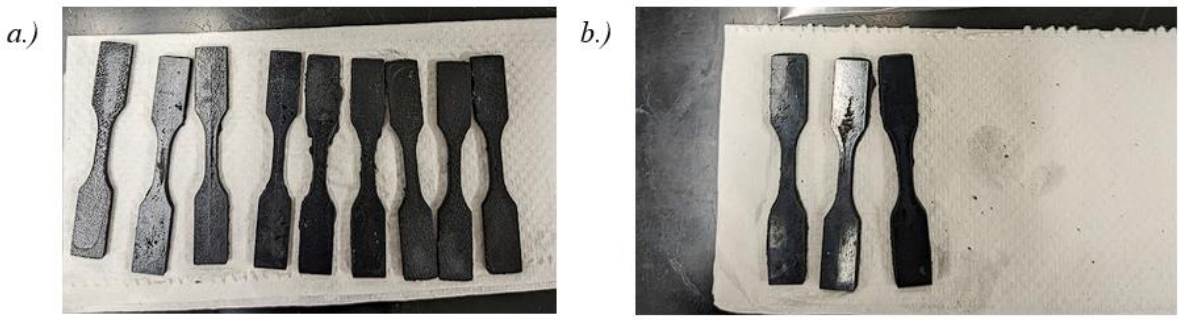


Figure 32: a.) 1 wt% samples with 60 seconds of in-situ pre- and post-curing. b.) 0.5 wt% samples with 60 seconds of in-situ cure pre-post curing.

Unexpected anomalies began to form during the extended cure time, where the resin began to cure the surrounding material due to the overexposure and extreme temperatures that the material was experiencing due to this overexposure. The new material being formed outside the boundaries of the designed dogbones was extremely porous and would break off cleanly at the boundary layer of the designed part. Figure 33b demonstrates this extra cured material as a growth-like substance around the 0.5 wt% samples. This material formed more commonly in areas between two samples instead of on the outside edges of samples. This reinforced the idea that the material was cured due to the increased heat and overexposure due to a printer malfunction.

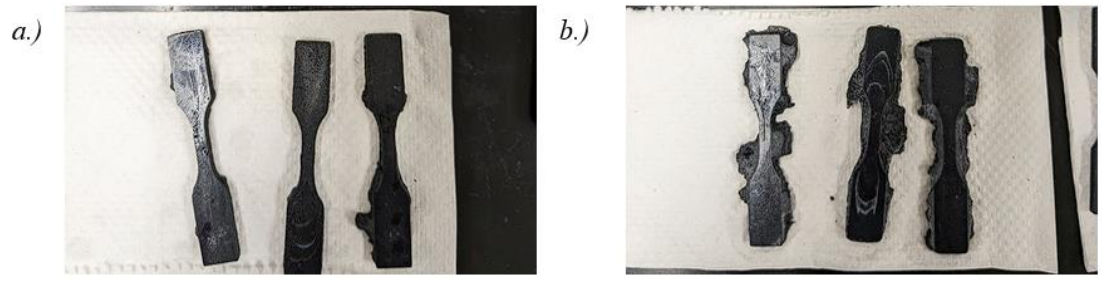


Figure 33: 1 wt% samples with 180 seconds of in-situ pre- and post-curing. b.) 0.5 wt% samples with 180 seconds of in-situ cure pre-post curing.

The 1 wt% samples did not appear to suffer from this artifact as prominently as the higher CNT concentration helped disperse the thermal energy and absorb the UV light better. This also insinuates that the 0.5 wt% samples are likely reaching a fully cured state during the in-situ manufacturing stage before reaching post-processing.

6.3.2 Tensile Test Results

The tensile test results varied greatly regarding UTS, Modulus, and strain at failure. This indicated that the proposed testing properly identified the key characteristics needed to improve mechanical strength. The results are summarized in Table 6, with run three showing the most promising results regarding UTS and modulus. The top three runs regarding UTS were all of the 0.5 wt% CNT concentrations. The worst performing nanocomposite was 1 wt% CNTs with long in-situ exposure and longer post-cure time.

Table 6: Average mechanical characteristics of each run

Average Values of Each Run							
Run	Stress (Mpa)	StressSD	Strain	StrainSD	Modulus (Mpa)	ModulusSD	Elongation (mm)
Run 1	58.558	6.813	0.116	0.018	592.559	20.098	0.883
Run 2	52.000	8.281	0.115	0.022	565.624	41.123	0.876
Run 3	75.967	7.984	0.111	0.012	858.898	107.773	0.846
Run 4	50.970	4.024	0.112	0.013	674.995	104.476	0.856
Run 5	52.903	5.522	0.077	0.001	813.161	97.242	0.588
Run 6	32.021	8.286	0.075	0.012	514.405	65.490	0.574
Run 7	49.009	8.686	0.072	0.018	830.695	63.892	0.547
Run 8	46.359	5.966	0.080	0.010	663.965	28.609	0.606

It is expected that as CNT concentration increases, the strength of the nanocomposite will also increase. These results were not experienced in this study, likely due to defects and inclusions created during manufacturing. There will be a theoretical limit of CNT concentration where the proposed manufacturing method will no longer be effective due to the rise in the viscosity of the nanocomposite. That limit appears to be near the 1 wt% concentration, as the only way to decrease viscosity without modifying the chemical makeup of the nanocomposite would be to increase the in-situ curing temperature. With the artifacts observed in the 0.5 wt% samples raising the temperature further is not feasible while retaining part geometry.

The longer post-exposure time lead to some of the worst results on average, with run six being statistically equivalent to the base matrix with no increase in part strength. The reduction in strength due to increased post-exposure is likely due to the fact that the long exposure is over-

curing the outer layers of the finalized part, causing them to become more brittle. This creates a weaker outer shell that will fail under tensile stress at a lower load than the properly cured samples. The 60-minute post-cure also subjects the samples to 80° C underwater conditions for 45 minutes longer than the shorter post-cure. This could be causing a thermal degradation that is not present in the other samples.

Concerning in-situ cure time, the longer exposure did appear to have a significant impact on part strength. Run three demonstrated a 15 MPa increase in strength over run 1 where the same composite and the same post-cure settings were utilized, but the in-situ curing was significantly shorter. Noteably run three also had the issue during printing with the formation of extra cured material around the tensile samples. Further testing would have to be conducted to determine if a reduction in in-situ temperature would help alleviate this issue or if slightly decreasing in-situ cure time would still lead to the same strength without the above problem presenting itself. All extra cured material that appeared to grow on the dogbones broke away very easily and was extremely porous in nature, so it provided no structural benefit during the testing as it was removed.

Further analysis of the stress and strain curves which can be found in Figures 42-49, can be seen that the 1 wt% samples often had anomalies compared to the 0.5 wt% samples. Run 4 and 6 specifically had large anomalies in the stress-strain curves. During run 4, one of the samples appears to hold a constant load while continuing to deform for the middle portion of the test as if it slipped but still breaks at an expected strain value. Run four ended up having the second lowest strain deviation out of all runs, even with this anomaly. This indicates that there were internal issues with the sample that likely led to this result. For run 6, sample 3 far outperformed the other samples in the data set. A fourth sample was tested to verify, and if the

results from sample 3 are removed, the average strength for that run drops to the lowest average value of just 28.065 MPa. As this run had a lower in-situ cure time, we expect more anomalies to occur with the higher CNT concentration. This increased probability of anomalies paired with the extended post-cure that creates brittle outside layers explains the unexpected results and the very high standard deviation in UTS.

To better determine the stress concentrations of a 0.5 wt% CNT nanocomposite, digital image correlation (DIC) was performed on a sample, as shown in Figure 34. This image was in the final frame before the sample failed, and it should be noted that the sample is only seeing about 5% strain compared to the chart above. This is likely due to the DIC's ability to only account for strain in the guage section based on the ASTM standards that are built into the Zeiss GOM software compared to Instron simply outputting strain as the total distance the mechanical system moved during the test.

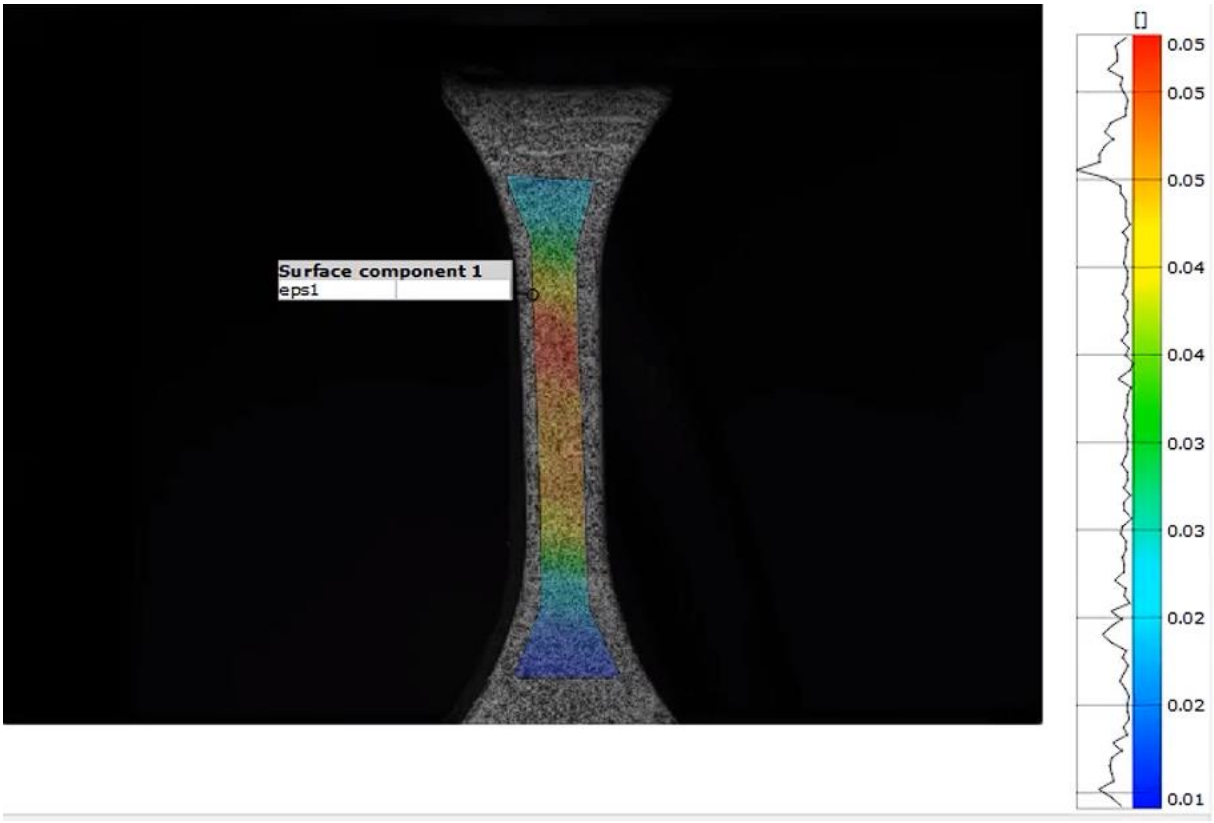


Figure 34: Digital Image Correlation displaying strain across a 0.5 wt% ASTM D638 Type V sample.

The DIC also reported an increased Modulus of 2800 MPa, which would lead to over a 30% increase in modulus from the manufacturer resin. These results appear to be far more realistic, as an increase in CNT to a resin should increase the stiffness and UTS of the material. The lower values reported from Instron are likely inaccurate when compared to the data provided by the manufacturer. Due to this issue, the values are only used on a comparative basis, and a system such as DIC is used to provide the final quantitative results of the best nanocomposites.

6.4 Conclusions

This study helped provide a baseline data set for optimizing CNT-based photopolymers that can be manufactured in commercially available AM machines. By modifying in-situ cure time, post-cure time, and CNT concentration, an optimized formulation was determined for increased part strength. The 0.5 wt% nanocomposites performed best with the unmodified commercial machines and demonstrated strength increases up to 230% stronger than the matrix material. These results greatly exceed other published results and reinforce the need for process optimization of photocurable printing systems. The 1 wt% nanocomposite concentrations performed far worse than expected due to manufacturing defects and inadequate curing of the material. Other anomalies were also identified in the manufacturing process, such as maximum cure temperatures for the 0.5 wt% nanocomposites before other materials in the vat began to polymerize. Future work for this study should focus on changing more variables, including layer height, in-situ cure temperature, post-cure temperature, and photoinitiator additives.

CHAPTER 7: FUTURE WORK AND CONCLUSIONS

7.1 Conclusions

The work presented in this dissertation provides a detailed insight into the challenges, solutions, and outcomes of utilizing commercially available AM machines to manufacture novel nanocomposites. A thorough study is conducted on the possibilities of improved mechanical, thermal, and electrical properties for different nanocomposites. These studies specifically focus on identifying and optimizing the manufacturing parameters for a given nanocomposite. The final results demonstrate composites that are greatly improved mechanically, chemically, thermally, and electrically.

7.1.1 AM Manufacturing of Antibacterial Photopolymers

Utilizing ZnO and TiO_2 as nanoparticle fillers proved advantageous when optimizing tensile strength, abrasion resistance, water contact angle, and surface hardness. These nanoparticles paired well with unmodified zero additive commercially available resins. Part strength was demonstrated to be increased by up to 25% when manufactured with the proper cure settings. Abrasion resistance was also improved in nearly all tests. The water contact angle was either improved or remained the same for all samples produced regardless of the base resin.

It was determined that the mixing of the nanoparticle was best achieved through a planetary mixer at elevated temperatures. This mixing process reduced agglomerations witnessed during early trials and yielded more consistent results. Manufacturing in a heated environment also proved beneficial as it allowed the material to reach a further degree of cure given the same amount of time. Post-curing also followed the same protocol, except that samples were submerged underwater. This helped aid in reducing the warp caused due to the in-situ stresses,

along with evenly heating the sample during curing. The water also helped refract the light around the sample, leading to a much more consistent post-cure.

The top limit of nanoparticles was determined to be near the 5 wt% value for the given nanoparticles as manufacturing defects appeared above that value. These defects are due to the increased viscosity, inclusions caused due to uneven curing, and large layer height relative to the cure depth. It was proven that the cure time must be changed for each nanocomposite to achieve the best mechanical results. These tests were used to ensure that the increase in strength was not driven by the increase in cure time of previous tests but by the increased nanoparticle addition.

It is possible to manufacture low-cost antibacterial parts utilizing custom novel nanocomposites on commercially available hardware. These parts are a promising option for the future of healthcare and public health in general as their low cost, quick manufacturing, and custom design options open up an array of engineering avenues for existing technologies. Incorporating other common lab equipment into the manufacturing and process control makes these parts significantly stronger and easier to manufacture than many existing options, such as injection molding and direct ink writing.

7.1.2 CNT Reinforced Photopoymers

Utilizing the information gained from the previous sets of studies, two different experiments were conducted that successfully manufactured samples with CNT reinforcement. The first study utilized a flexible thermoset to manufacture custom strain sensors for human motion detection. These sensors could be manufactured at high rates of speed with custom design geometry based on the end user. The second study delved into optimization printing parameters for CNT-based nanocomposites. Utilizing a rigid, high-temperature resistant

thermoset resin as a base, the study produced samples with a UTS of over 225% stronger than the base resin.

The flexible-based sensors were developed using a low-concentration nanocomposite to help develop a manufacturing process for later projects that aimed to increase the CNT concentrations. These sensors were tested using a resistance meter to measure break-in, fatigue, gauge factor, and level of response correlated to strain. When paired with a human for automated motion control detection, a custom Matlab code was developed to automate the detection process. These sensors provided reliable results across 100s fatigue cycles and a consistent gauge factor throughout break-in. This novel nanocomposite would be well suited for incorporation into prosthetics, soft robotics, or human motion detection applications where user comfort is critical.

The second study was designed around eight different runs to optimize the manufacturing process of a CNT nanocomposite. It successfully demonstrated which key characteristics played a role in the mechanical properties of a nanocomposite and led to improved mechanical strength in nearly all cases. This study also demonstrated that manufacturing CNT nanocomposites up to a 1 wt% concentration was possible, but there will likely be defects during the printing process that reduce the material's overall strength. If strength is not a concern but electrical response or thermal conductivity is the priority, these nanocomposites would be well suited for those applications.

7.1.3 Key Parameters in Producing Mechanically Strong Parts

To summarize all results to form a conclusion and recommendation for future research, the energy input into each sample discussed throughout was calculated along with all of its mechanical properties listed in relation to the virgin material. This calculation aimed to

determine at what stage the sample was being cured, how much total energy the sample was exposed to, and the effect of other manufacturing parameters such as temperature and layer height. Twenty-seven different process parameters were studied and utilized to perform correlation calculations to deliver the following conclusions. A value of 1 represents a strong correlation, and a value of -1 represents the opposite.

I The percentage of energy delivered in situ compared to post-processing has a 0.67 correlation to increasing the part's final strength compared to the virgin material.

II The bottom several layers in situ cure time has a 0.61 correlation to increasing the part's final strength compared to the virgin material.

III The standard cure time has a 0.55 correlation to increasing the part's final strength compared to the virgin material.

IV The in situ temperature has a 0.45 correlation to increasing the part's final strength compared to the virgin material.

The following correlations strongly support the idea that nanocomposite resin manufacturing must rely more heavily on in-situ manufacturing parameters compared to standard virgin resins. The nanoparticle's ability to absorb and interact with UV light creates manufacturing hurdles that must be overcome through temperature control and increased energy delivery. With only three different in situ temperatures being tested, it is expected that the correlation will increase with more trials. It is also recommended that for all future work, viscosity should be added as a data point to determine the effect of viscosity on cure rate and part strength.

Several manufacturing parameters that had little correlation to the final part strength, contrary to common practice, included manipulation of the post-cure time and the layer height. Post-cure time is less critical for nanocomposite parts as the UV light can only penetrate up to several hundred microns through the surface compared to translucent virgin resins. What did have a weak correlation regarding post-curing, though, was the temperature. Higher post-cure temperatures did show a weak upward trend with regard to final part strength. This is likely because it added more energy to the system to allow the material to finalize the polymerization started during printing. Layer height had no correlation to strength, not because it doesn't affect processing time but because layer height was treated as an energy-independent variable, and therefore assuming the same energy is delivered per unit volume of material layer height does not affect final part strength. All layer height testing was performed at a value of 50 microns or less; therefore, UV penetration was not a concern.

My final recommendation based on these conclusions is that to improve the transparency and state of the art regarding resin-based AM of nanocomposites, the following should be done:

I Present curing statistics for photopolymers utilizing energy delivered per layer rather than printer settings.

II Collect temperature data for every stage of manufacturing, including mixing, printing, post-processing, and drying.

III Perform cure tests to determine the maximum UV penetration of a nanocomposite to better tailor the printing parameters for that material.

7.2 Future Work

The work presented here clearly defines the critical variables and considerations for manufacturing novel nanocomposites on commercial photocurable resin systems. It highlights the importance of process control, nanocomposite concentration, and material handling. Utilizing these findings as a guideline, future work should be conducted to develop an optimization system that can be followed for any nanocomposite. Due to the large number of variables directly impacting part strength, the best way to optimize novel resins is through trial runs, as demonstrated in this research.

To develop a system that does not require the intricate process of running trials, a system should be developed utilizing a rate of cure meter similar to what was developed in this work paired with several thermal tests to outline the best manufacturing process for a given nanocomposite. This would allow for the rapid adoption of new resins into the industry while providing greatly improved strength and functional properties compared to current market offerings.

The success of the flexible sensor system should be further researched to develop soft robotic systems and prosthetic additions. An initial design was performed of a soft finger robotic arm that could be manufactured with this resin, as shown in Figure 35. This material could be manufactured with varying CNT concentrations at different z heights of the robotic arm to deliver varying responses based on the deformation. The design freedom for systems like this is greatly increased compared to traditional manufacturing, as complex channels and internal pressure chambers can be designed and printed in one piece.

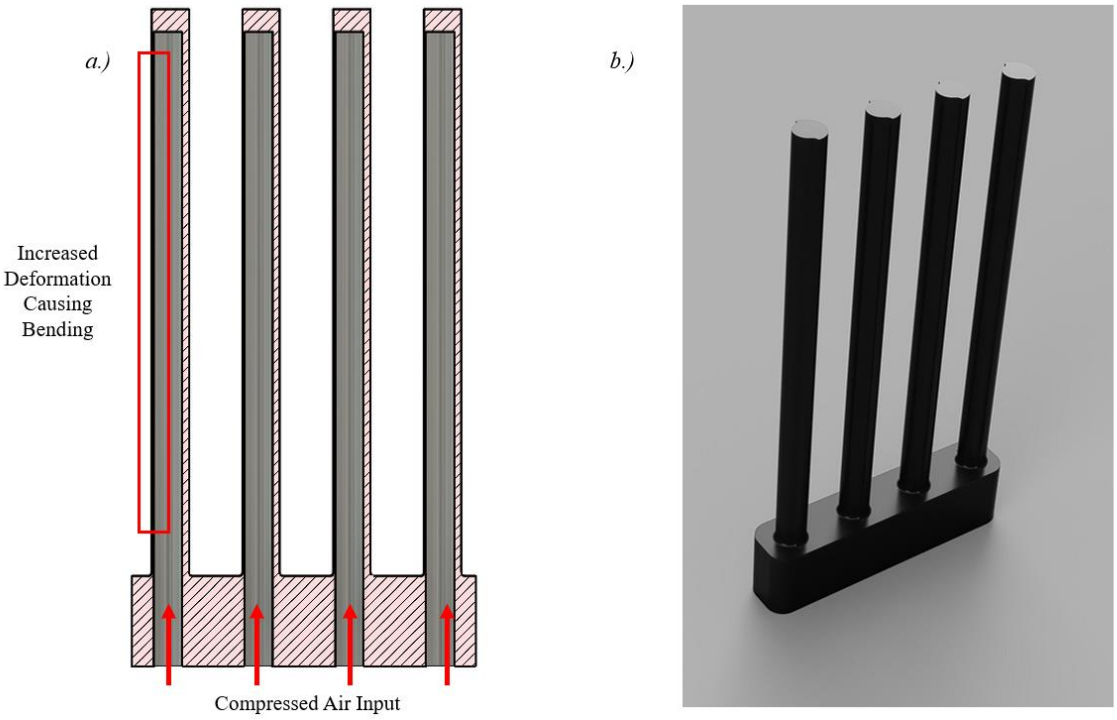


Figure 35: a.) Cutaway of soft robotic finger system with internal cavities and dynamic wall thickness. b.) Full render of finished CNT embedded print.

Additional modifications to the printing system should also be considered to aid in part manufacturing. The most significant obstacle to overcome at higher nanoparticle concentrations was inclusions or voids due to the lack of the ability to reflow properly. Implementing a recoating system similar to SLS machines in this scenario should be greatly beneficial as it will ensure the bottom is perfectly coated before each layer. A proposed system was designed and shown in Figure 36 to recoat the printing vat after each layer evenly. This system would also allow for direct heating of the material and additional data measurement through infrared sensors and thermocouples.

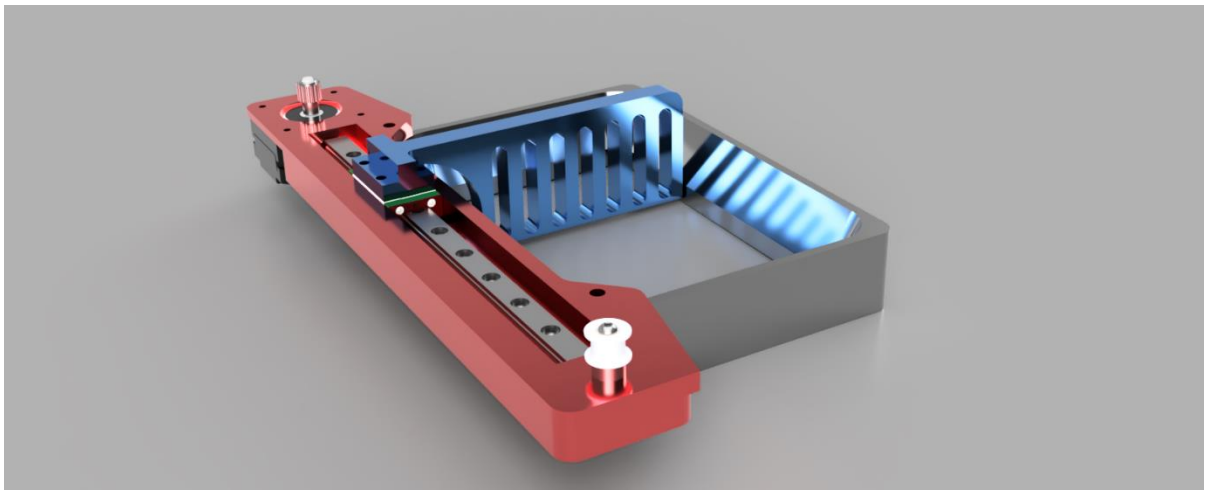


Figure 36: A custom recoating system designed for MSLA and DLP printing systems for use with high-concentration nanoparticles.

To summarize, the work presented in this report clearly defines the requirements for using AM to produce high-fidelity novel nanocomposites. The proposed manufacturing process demonstrated Significant improvements in all mechanical applications. Future work should include further refining secondary variables and making machine modifications to improve the capability of this technology further. The ability to manufacture advanced functional polymers at a sub-20 micron scale in all dimensions will allow for great advancements in many different industries.

APPENDIX – SUPPORTING INFORMATION

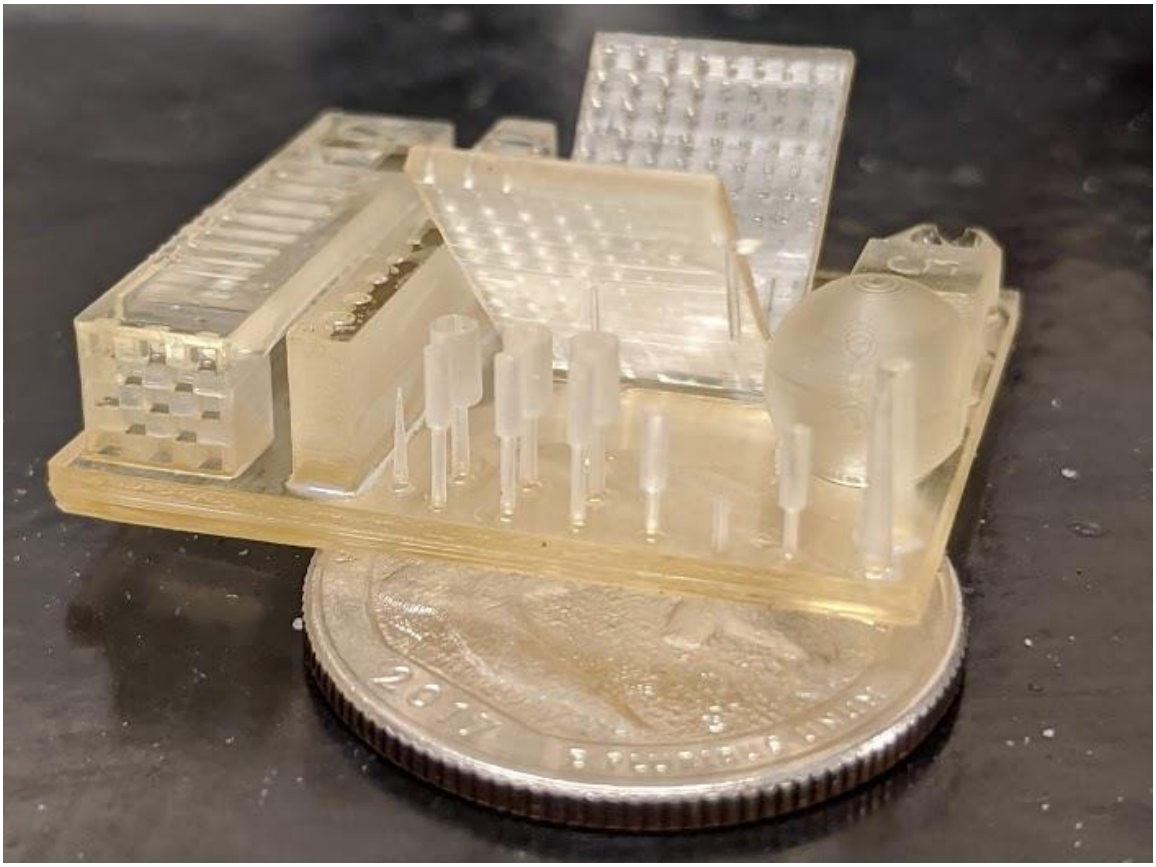


Figure 37: Calibration Test of Virgin Resin on MSLA Printer

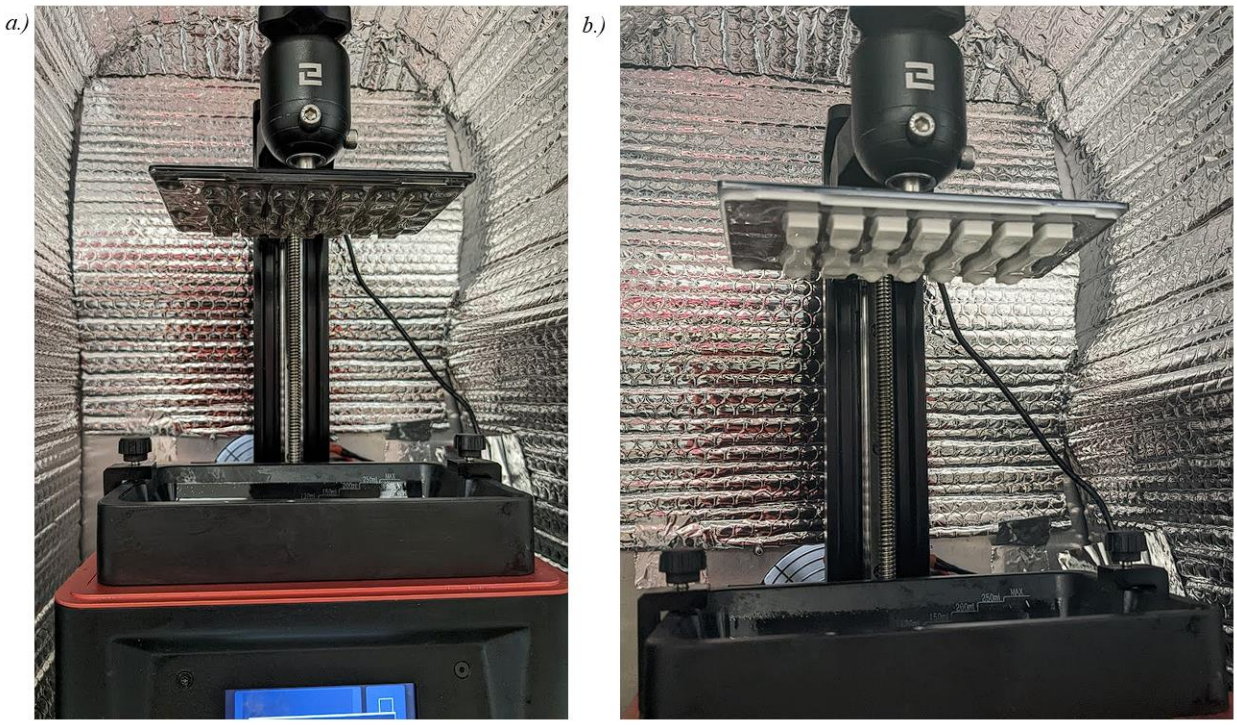


Figure 38: a.) Virgin translucent resin during batch printing on MSLA printer. b.) Zinc Oxide reinforced nanocomposite during batch printing on MSLA printer.

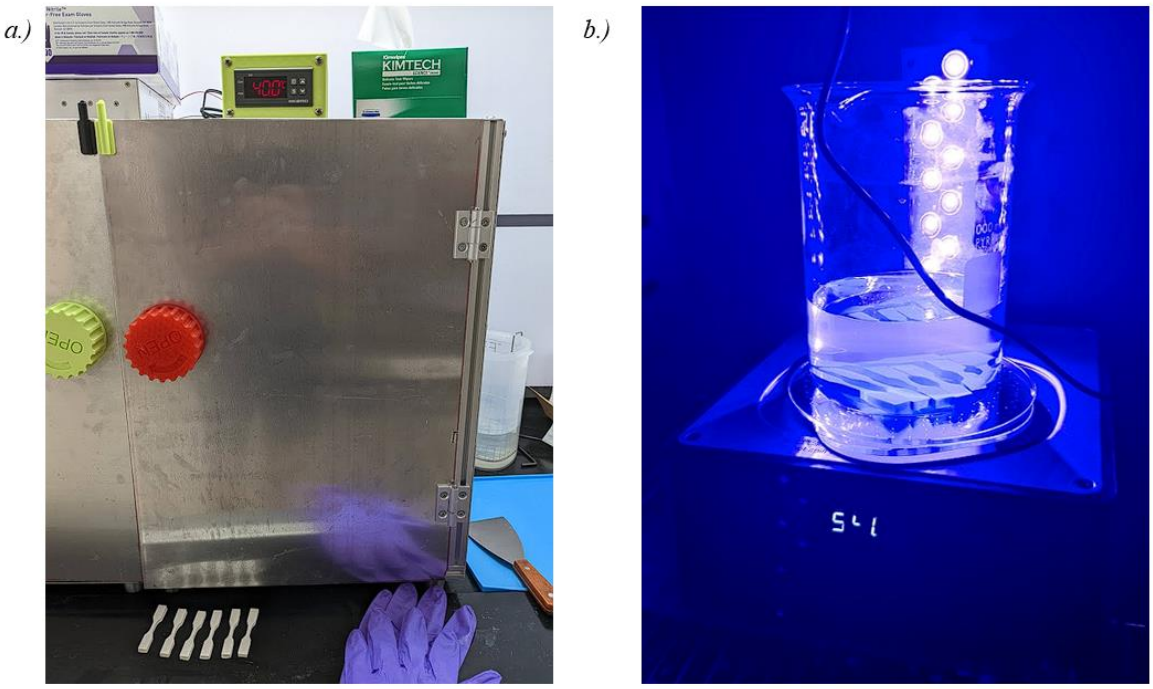


Figure 39: a.) Custom heated in-situ manufacturing enclosure system. b.) High-temperature underwater post-curing system.



Figure 40: a.) Custom machined fixturing for machining off bottom layers of samples. b.) CNC machining of the samples using custom toolpaths and flood coolant to negate any chipping or stress concentrations.

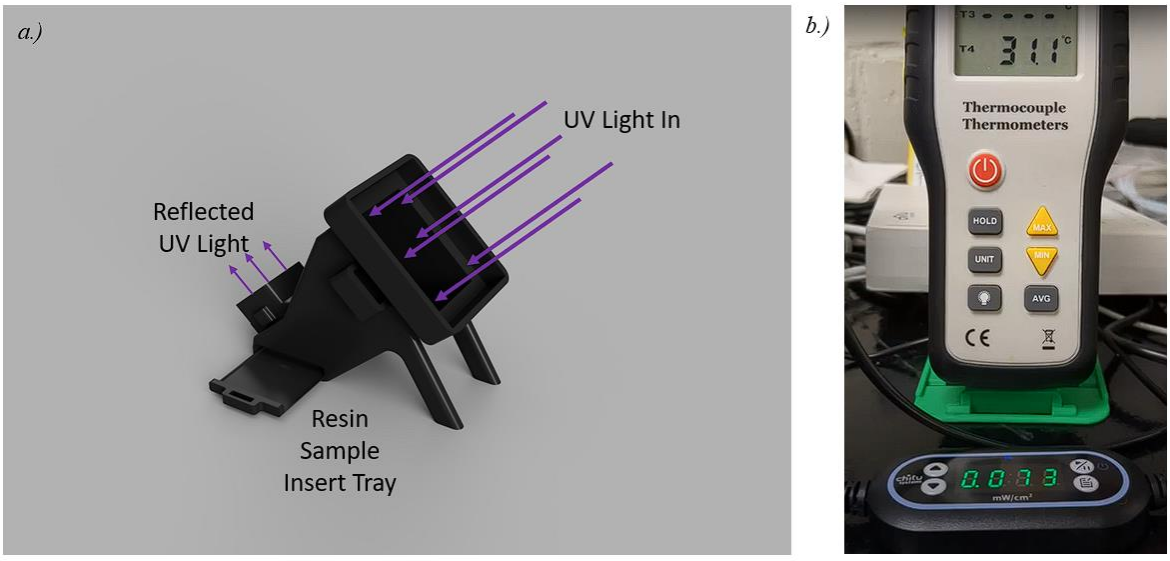


Figure 41: a.) Rate of cure testing apparatus with removable sample trays. b.) Live measurement of the reflected UV light and the temperature of the resin.

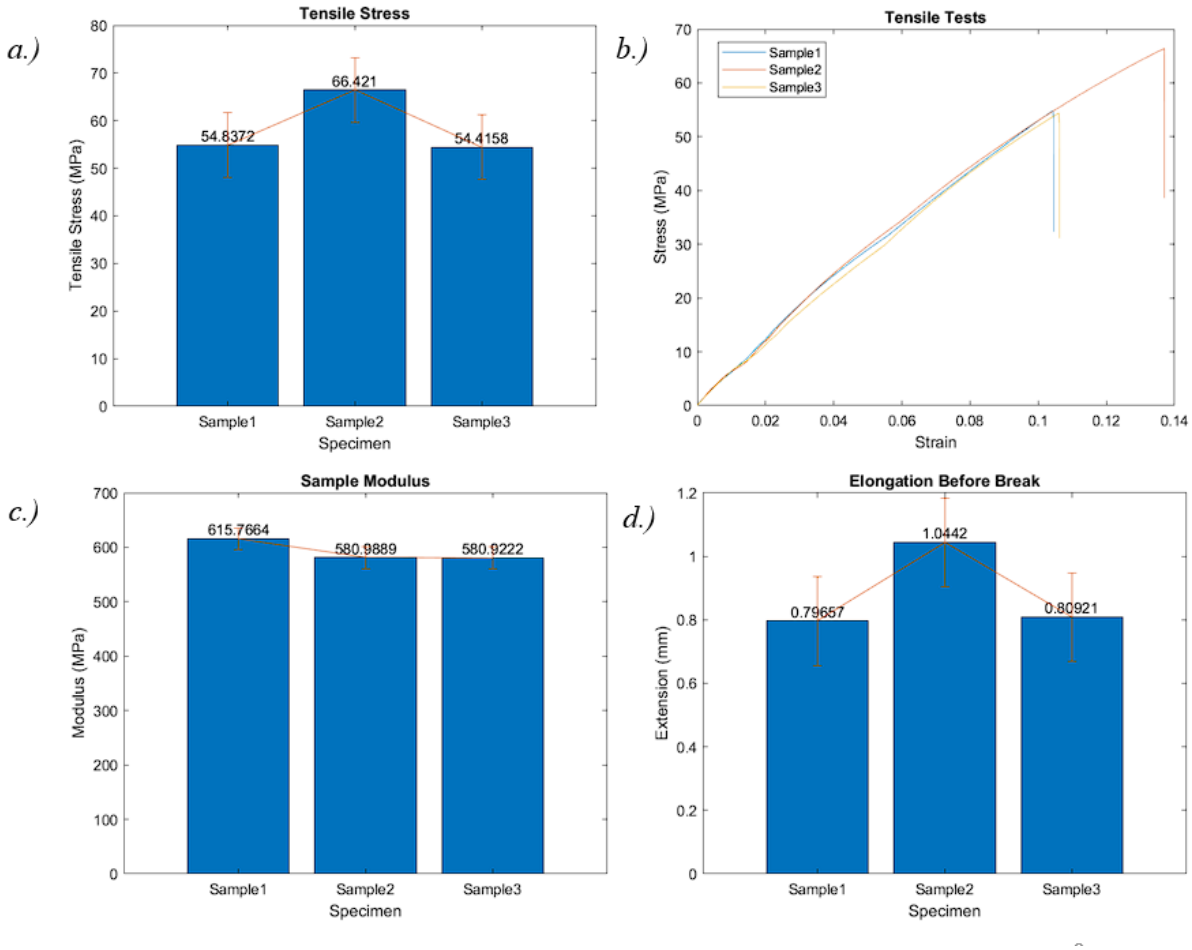


Figure 42: Run 1 of CNT Manufacturing Test. a.) Tensile test results of the specimens. b.) A stress strain curve of all three specimens. c.) Modulus of all specimens. d.) Amount of elongation or strain before break.

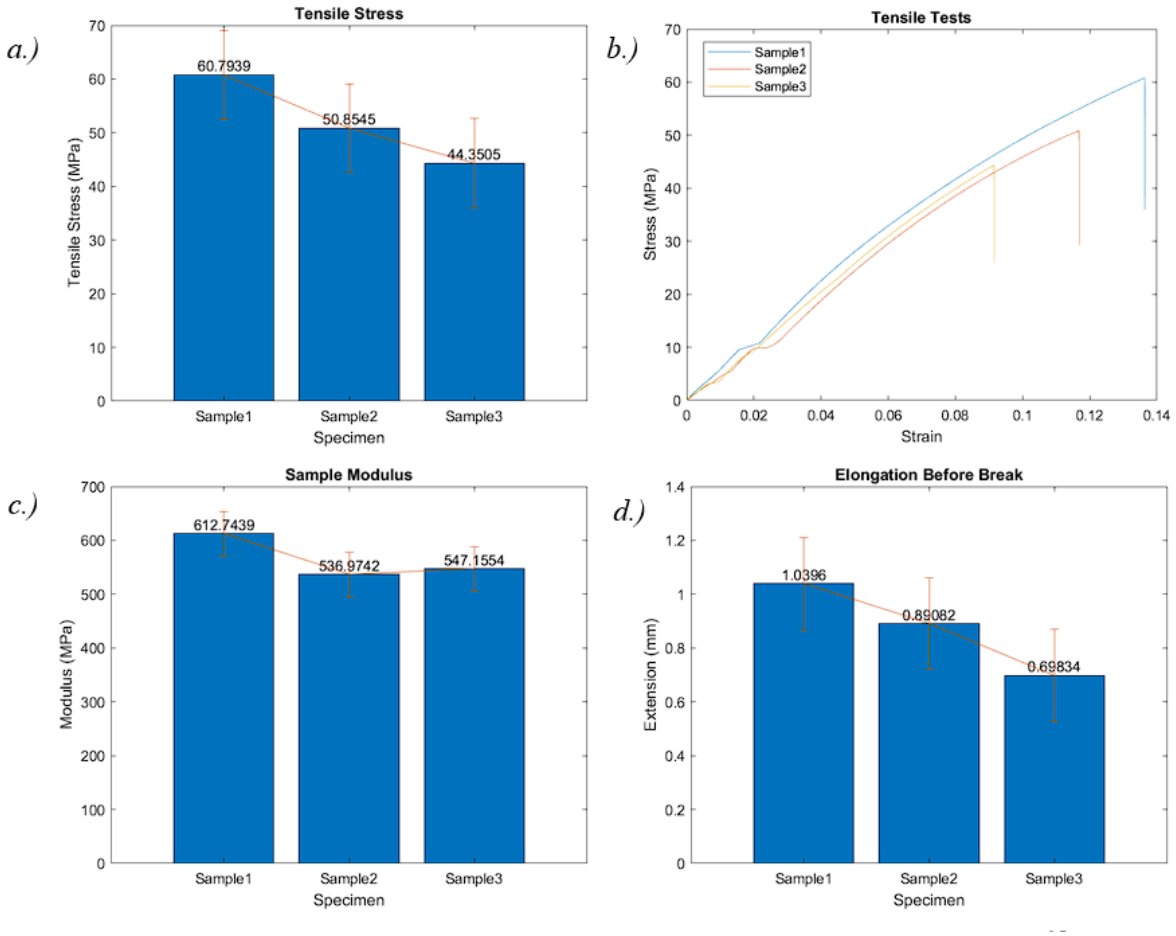


Figure 43: Run 2 of CNT Manufacturing Test. a.) Tensile test results of the specimens. b.) A stress strain curve of all three specimens. c.) Modulus of all specimens. d.) Amount of elongation or strain before break.

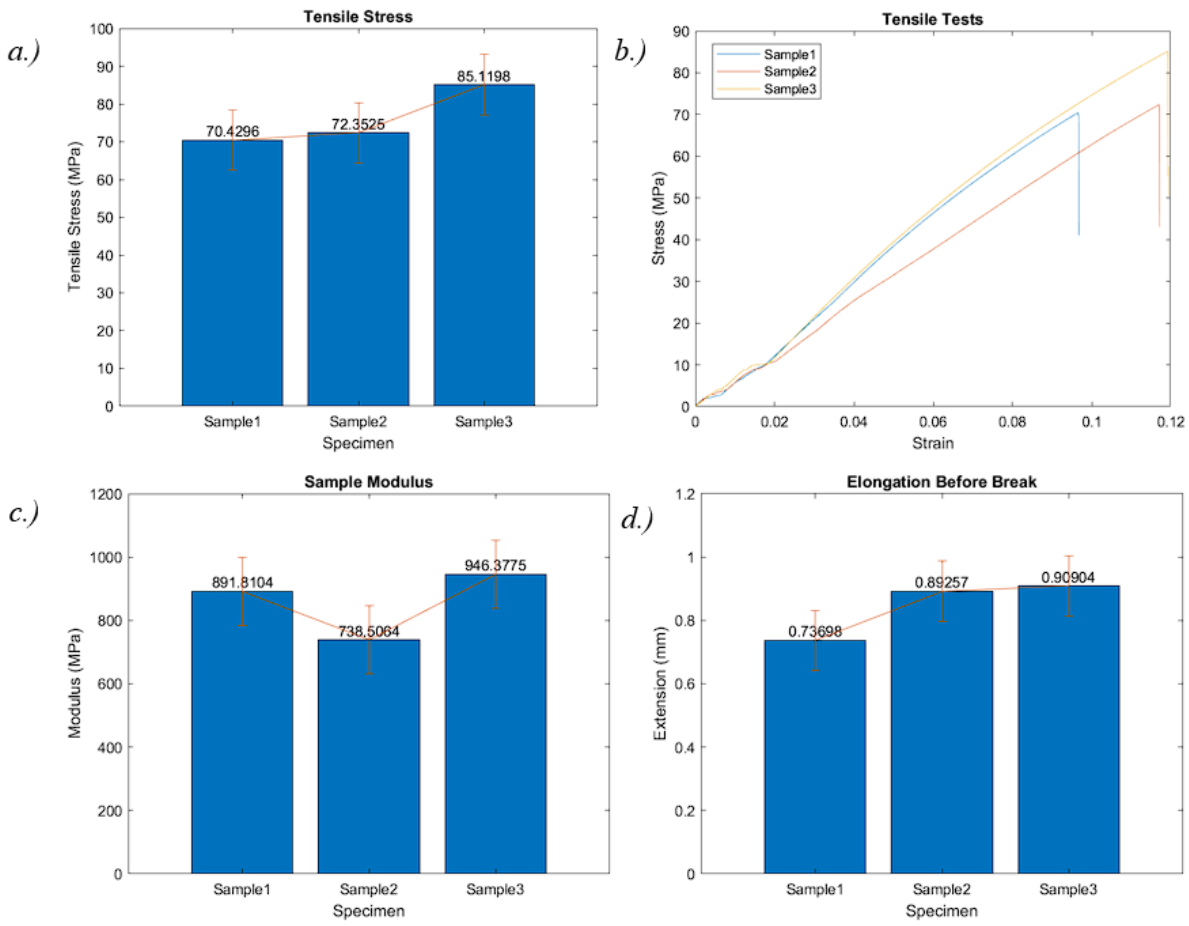


Figure 44: Run 3 of CNT Manufacturing Test. a.) Tensile test results of the specimens. b.) A stress strain curve of all three specimens. c.) Modulus of all specimens. d.) Amount of elongation or strain before break.

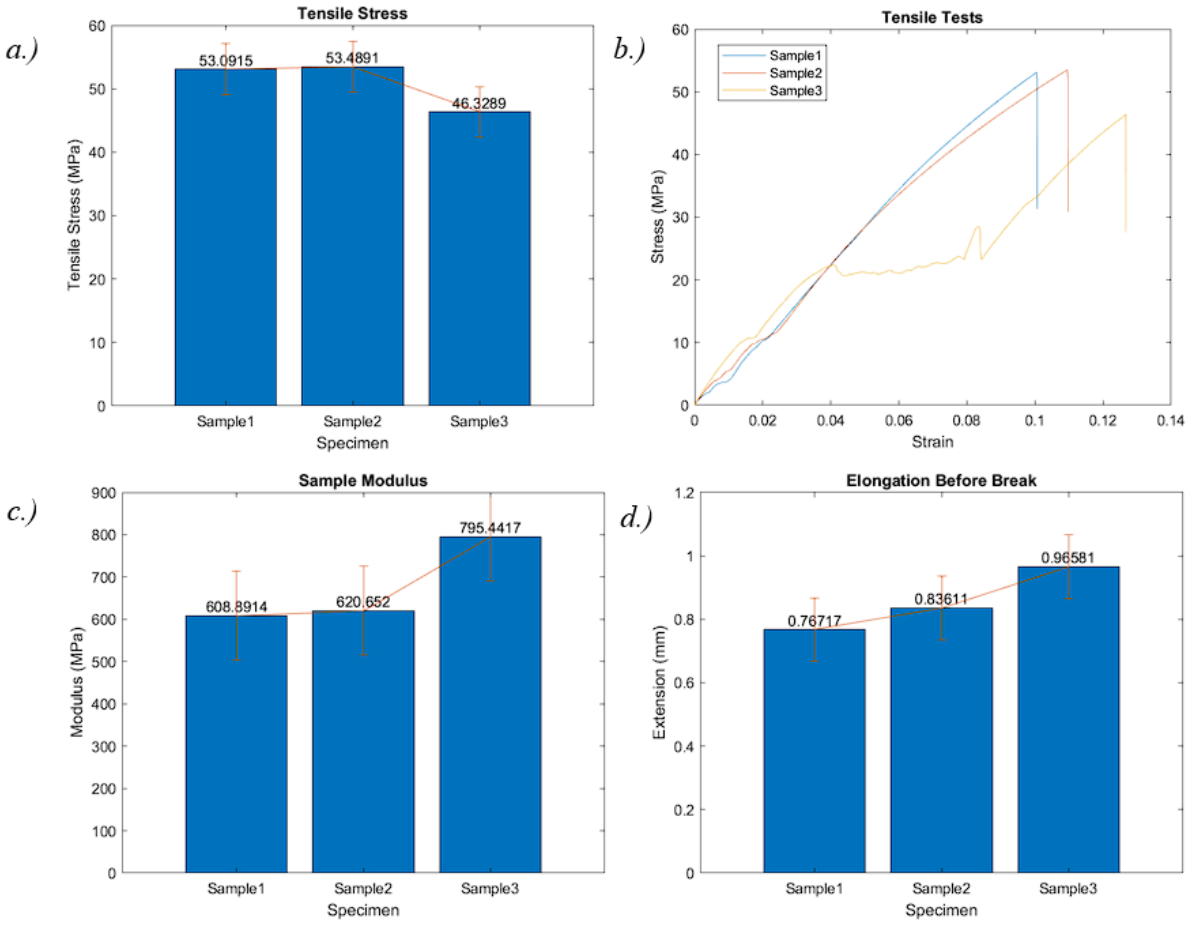


Figure 45: Run 4 of CNT Manufacturing Test. a.) Tensile test results of the specimens. b.) A stress strain curve of all three specimens. c.) Modulus of all specimens. d.) Amount of elongation or strain before break.

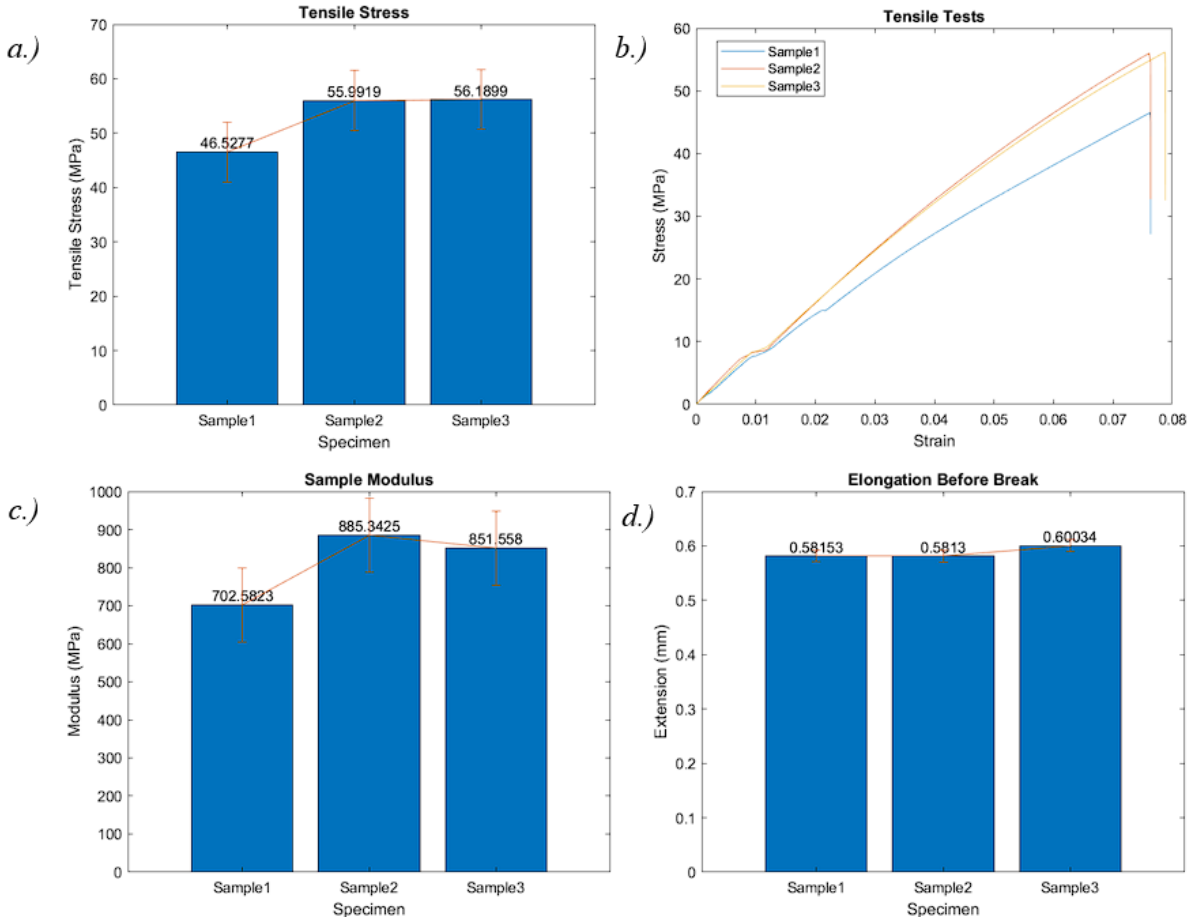


Figure 46: Run 5 of CNT Manufacturing Test. a.) Tensile test results of the specimens. b.) A stress strain curve of all three specimens. c.) Modulus of all specimens. d.) Amount of elongation or strain before break.

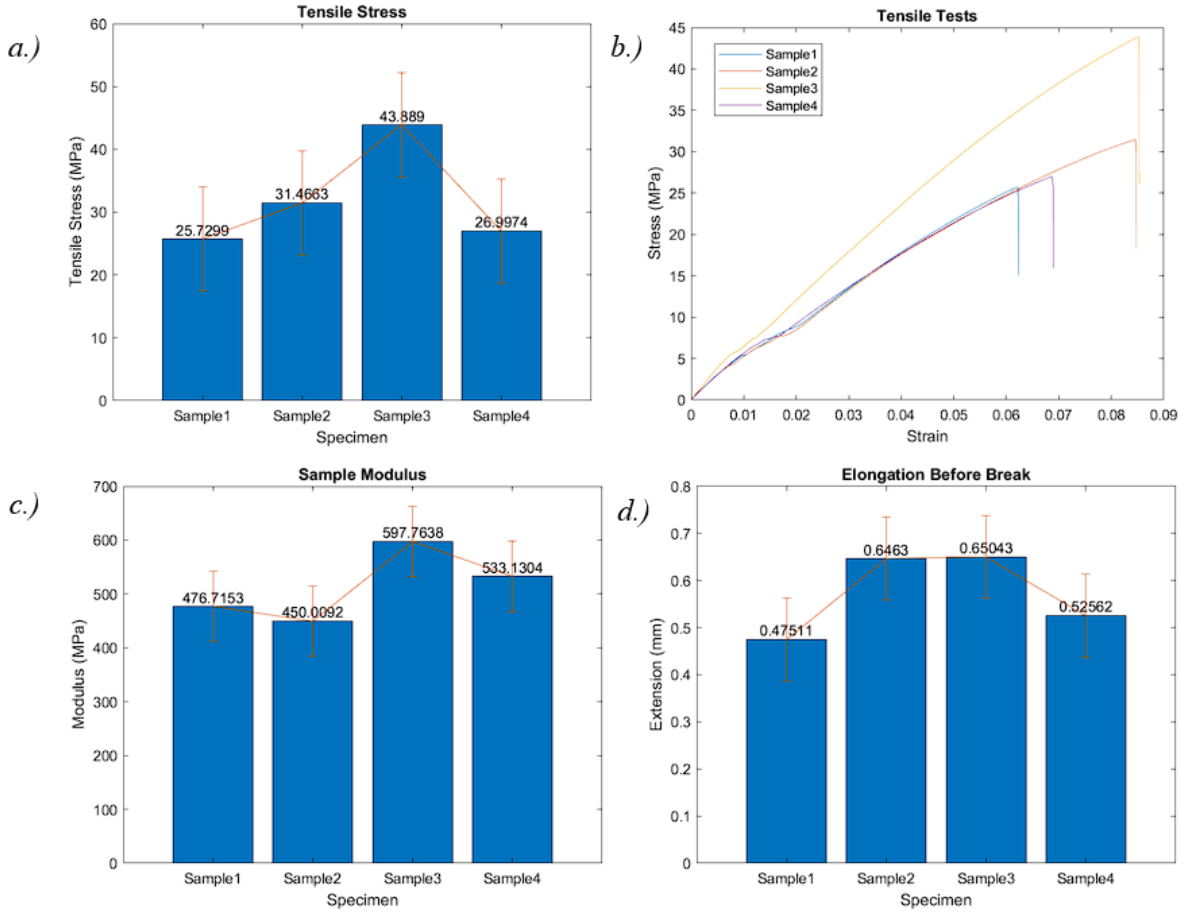


Figure 47: Run 6 of CNT Manufacturing Test. a.) Tensile test results of the specimens. b.) A stress strain curve of all three specimens. c.) Modulus of all specimens. d.) Amount of elongation or strain before break.

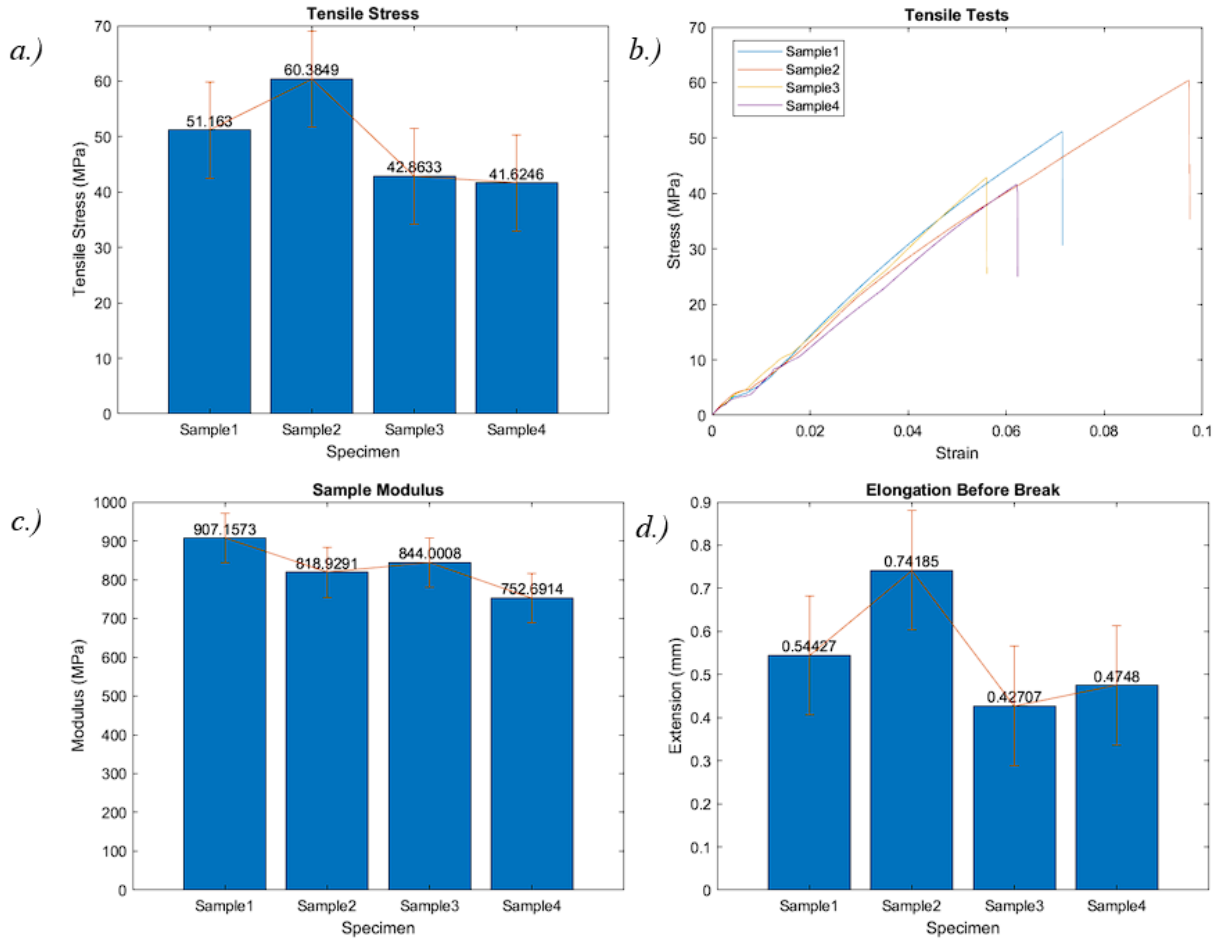


Figure 48: Run 7 of CNT Manufacturing Test. a.) Tensile test results of the specimens. b.) A stress strain curve of all three specimens. c.) Modulus of all specimens. d.) Amount of elongation or strain before break.

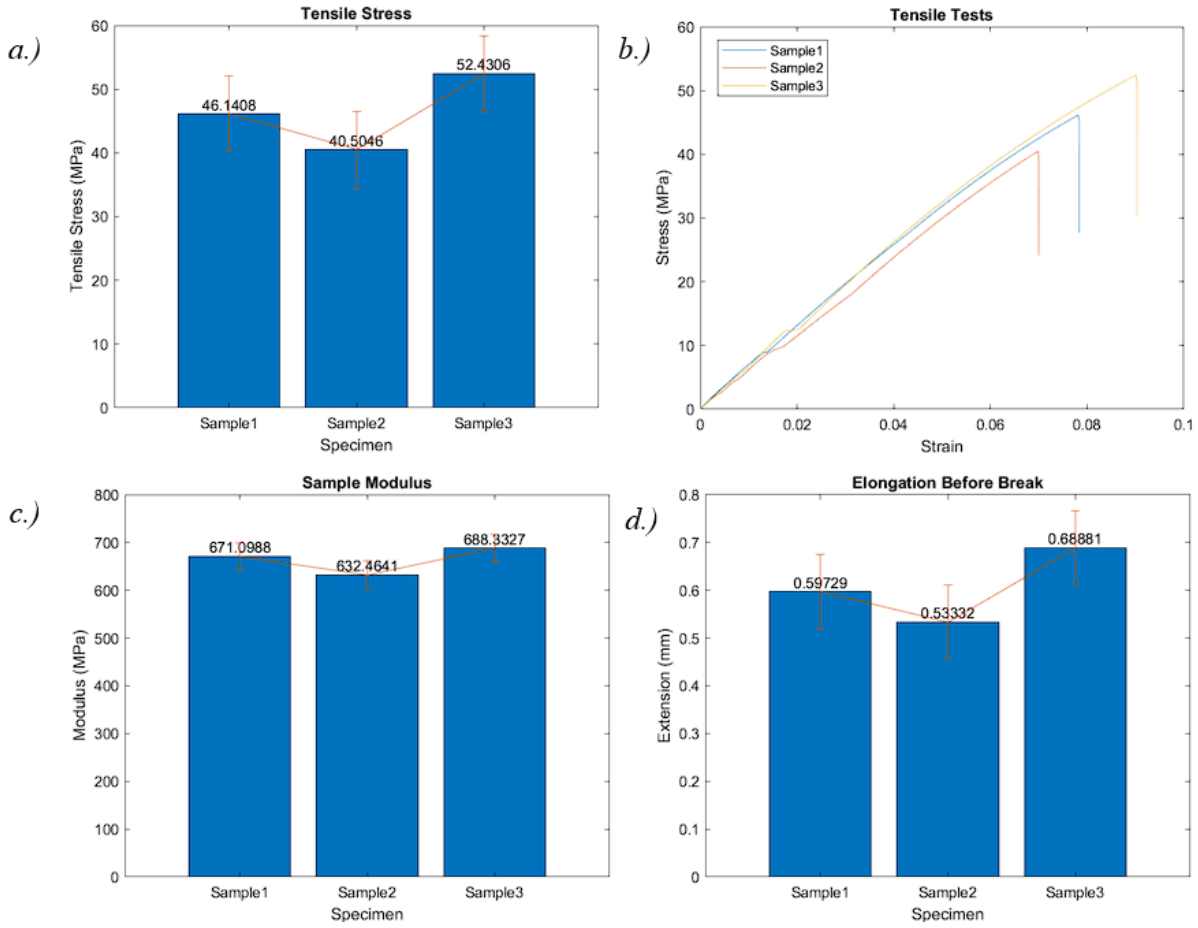


Figure 49: Run 8 of CNT Manufacturing Test. a.) Tensile test results of the specimens. b.) A stress strain curve of all three specimens. c.) Modulus of all specimens. d.) Amount of elongation or strain before break.

REFERENCES

[1] D. Wu, Z. Zhao, Q. Zhang, H. J. Qi, and D. Fang, *Soft Matter*, 2019, **15**(30), 6151-6159.

[2] H. Quan, T. Zhang, H. Xu, S. Luo, J. Nie, and X. Zhu, *Bioactive Materials*, 2020, **5**(1), 110-115.

[3] S. M. El-Megharbel, M. Alsawat, F. A. Al-Salmi, and R. Z. Hamza, *Coatings*, 2021, **11**(4), 388.

[4] P. K. Rai, Z. Usmani, V. K. Thakur, V. K. Gupta, and Y. K. Mishra, *Current Research in Green and Sustainable Chemistry*, 2020, **3**, 100011.

[5] S. Khan, M. Ul-Islam, W. A. Khattak, M. W. Ullah, and J. K. Park, *Cellulose*, 2015, **22**(1), 565-579.

[6] O. Yamamoto, *International Journal of Inorganic Materials*, 2001, **3**(7), 643-646.

[7] K. R. Raghupathi, R. T. Koodali, and A. C. Manna, *Langmuir*, 2011, **27**(7), 4020-4028.

[8] J. Sun, A. M. Forster, P. M. Johnson, N. Eidelman, G. Quinn, G. Schumacher, X. Zhang, and W.-l. Wu, *Dental Materials*, 2011, **27**(10), 972-982.

[9] A. Lo Giudice, V. Ronsivalle, L. Rustico, K. Aboulazm, G. Isola, and G. Palazzo, *Clinical Oral Investigations*, 2022, **26**(1), 303-312.

[10] A. Nulty, *BDJ Open*, 2022, **8**(1).

[11] L. A. Chavez, J. E. Regis, L. C. Delfin, C. A. Garcia Rosales, H. Kim, N. Love, Y. Liu, and Y. Lin, *Journal of Applied Polymer Science*, 2019, **136**(22), 47600.

[12] D. Mondal and T. L. Willett, *Journal of the Mechanical Behavior of Biomedical Materials*, 2022, **135**, 105450.

[13] S.-H. Chiu, S. T. Wicaksono, K.-T. Chen, C.-Y. Chen, and S.-H. Pong, *Rapid Prototyping Journal*, 2015, **21**(3), 262-269.

[14] S.-H. Chiu and D.-C. Wu, *Journal of Applied Polymer Science*, 2008, **107**(6), 3529-3534.

[15] I. Ahmed, K. Sullivan, and A. Priye, *Biosensors*, 2022, **12**(8), 652.

[16] C. Billings, C. Cai, and Y. Liu, *Polymers*, 2021, **13**(16), 2616.

[17] P. Parandoush and D. Lin, *Composite Structures*, 2017, **182**, 36-53.

[18] B. Herren, M. C. Saha, M. C. Altan, and Y. Liu, *Polymers*, 2022, **14**(11), 2269.

[19] M. Abshirini, M. Charara, Y. Liu, M. Saha, and M. Altan, *Advanced Engineering Materials*, 2018, **20**.

[20] L. Singh, B. Singh, and K. K. Saxena, *Advances in Materials and Processing Technologies*, 2020, **6**(2), 441-457.

[21] B. Ding, T. Ogawa, J. Kim, K. Fujimoto, and S. Shiratori, *Thin Solid Films*, 2008, **516**(9), 2495-2501.

[22] C. Hueber, K. Horejsi, and R. Schledjewski, *Advanced Manufacturing: Polymer & Composites Science*, 2016, **2**(1), 1-13.

[23] B. Yalcin, D. Valladares, and M. Cakmak, *Polymer*, 2003, **44**(22), 6913-6925.

[24] I. Blanco, *Journal of Composites Science*, 2020, **4**(2), 42.

[25] C. Mendes-Felipe, J. Oliveira, I. Etxebarria, J. L. Vilas-Vilela, and S. Lanceros-Mendez, *Advanced Materials Technologies*, 2019, **4**(3), 1800618.

[26] L. Brunet, D. Y. Lyon, E. M. Hotze, P. J. Alvarez, and M. R. Wiesner, *Environmental science & technology*, 2009, **43**(12), 4355-4360.

[27] M. Shekofteh-Gohari, A. Habibi-Yangjeh, M. Abitorabi, and A. Rouhi, *Critical Reviews in Environmental Science and Technology*, 2018, **48**(10-12), 806-857.

[28] B. Abebe, E. A. Zereffa, A. Tadesse, and H. Murthy, *Nanoscale research letters*, 2020, **15**(1), 1-19.
[29] P. Marashizadeh, M. Abshirini, M. Saha, L. Huang, and Y. Liu, *Advanced Theory and Simulations*, 2022, 2200010.
[30] Y. Lin, G. Ehlert, and H. A. Sodano, *Advanced functional materials*, 2009, **19**(16), 2654-2660.
[31] P. Marashizadeh, M. Abshirini, M. Saha, L. Huang, and Y. Liu, *Langmuir*, 2021, **37**(23), 7138-7146.
[32] L.-E. Shi, Z.-H. Li, W. Zheng, Y.-F. Zhao, Y.-F. Jin, and Z.-X. Tang, *Food Additives & Contaminants: Part A*, 2014, **31**(2), 173-186.
[33] B. L. da Silva, B. L. Caetano, B. G. Chiari-Andréo, R. C. L. R. Pietro, and L. A. Chiavacci, *Colloids and Surfaces B: Biointerfaces*, 2019, **177**, 440-447.
[34] K. Q. B. C. J. Yu and W. Ho, *Alloys Compd*, 2017, **727**, 792-820.
[35] J. Guo, Y. Zeng, P. Li, and J. Chen, *Ceramics International*, 2019, **45**(17, Part B), 23007-23012.
[36] A. Sirelkhatim, S. Mahmud, A. Seeni, N. H. M. Kaus, L. C. Ann, S. K. M. Bakhori, H. Hasan, and D. Mohamad, *Nano-Micro Lett.*, 2015, **7**(3), 219-242.
[37] T. Miyauchi, M. Yamada, A. Yamamoto, F. Iwasa, T. Suzawa, R. Kamijo, K. Baba, and T. Ogawa, *Biomaterials*, 2010, **31**(14), 3827-3839.
[38] M. Cacaci, C. Martini, C. Guarino, R. Torelli, F. Bugli, and M. Sanguinetti, *Advances in Microbiology, Infectious Diseases and Public Health: Volume 14*, 2020, 21-35.
[39] L. Rizzello, R. Cingolani, and P. P. Pompa, *Nanomedicine*, 2013, **8**(5), 807-821.
[40] M. Saito, *Journal of Coated Fabrics*, 1993, **23**(2), 150-164.
[41] E. G. Goh, X. Xu, and P. G. McCormick, *Scripta Materialia*, 2014, **78-79**, 49-52.
[42] B. Ramezanzadeh, M. Attar, and M. Farzam, *Journal of thermal analysis and calorimetry*, 2011, **103**(2), 731-739.
[43] B. Nowacki, P. Kowol, M. Kozioł, P. Olesik, J. Wieczorek, and K. Wacławiak, *Materials*, 2021, **14**(17), 4856.
[44] M. Lee, G. Kwak, and K. Yong, *ACS Applied Materials & Interfaces*, 2011, **3**(9), 3350-3356.
[45] A. N. Ren-De Sun, F. Akira, W. Toshiya, and H. Kazuhito, *J. Phys. Chem. B*, 2001, **105**(10), 1984-1990.
[46] J.-M. Park, J.-S. Ahn, H.-S. Cha, and J.-H. Lee, *Materials*, 2018, **11**(6), 1043.
[47] U. Diebold, *Surface Science Reports*, 2003, **48**(5), 53-229.
[48] C. Han, J. Lalley, D. Namboodiri, K. Cromer, and M. N. Nadagouda, *Current Opinion in Chemical Engineering*, 2016, **11**, 46-51.
[49] L. M. Anaya-Esparza, Z. Villagrán-De La Mora, J. M. Ruvalcaba-Gómez, R. Romero-Toledo, T. Sandoval-Contreras, S. Aguilera-Aguirre, E. Montalvo-González, and A. Pérez-Larios, *Processes*, 2020, **8**(11), 1395.
[50] M. Morsella, N. D'Alessandro, A. E. Lanterna, and J. C. Scaiano, *ACS Omega*, 2016, **1**(3), 464-469.
[51] B. Dréno, A. Alexis, B. Chuberre, and M. Marinovich, *Journal of the European Academy of Dermatology and Venereology*, 2019, **33**(S7), 34-46.
[52] R. Nakano, H. Ishiguro, Y. Yao, J. Kajioka, A. Fujishima, K. Sunada, M. Minoshima, K. Hashimoto, and Y. Kubota, *Photochem Photobiol Sci*, 2012, **11**(8), 1293-1298.

[53] W. Kangwansupamonkon, V. Lauruengtana, S. Surassmo, and U. Ruktanonchai, *Nanomedicine: Nanotechnology, Biology and Medicine*, 2009, **5**(2), 240-249.
[54] H. Kong, J. Song, and J. Jang, *Environmental Science & Technology*, 2010, **44**(14), 5672-5676.
[55] F. Subirada, R. Paoli, J. Sierra-Agudelo, A. Lagunas, R. Rodriguez-Trujillo, and J. Samitier, *Polymers*, 2022, **14**(14), 2955.
[56] A. Cortés, X. F. Sánchez-Romate, A. Jiménez-Suárez, M. Campo, A. Esmaeili, C. Sbarufatti, A. Ureña, and S. G. Prolongo, *Nanomaterials*, 2021, **11**(5), 1106.
[57] N. Vidakis, M. Petousis, E. Velidakis, N. Mountakis, D. Tsikritzis, A. Gkagkanatsiou, and S. Kanellopoulou, *Biomimetics*, 2022, **7**(1), 8.
[58] N. Vidakis, M. Petousis, N. Michailidis, J. D. Kechagias, N. Mountakis, A. Argyros, O. Boura, and S. Grammatikos, *Journal of the Mechanical Behavior of Biomedical Materials*, 2022, **134**, 105408.
[59] X. Zhao, J. Han, Y. Song, X. Shen, J. Xiao, and X. Feng, *Sustainable Computing: Informatics and Systems*, 2022, **35**, 100762.
[60] C. Billings, P. Kim, T. Shadid, J. D. Ballard, C. Cai, and Y. Liu, *Journal of Composites Science*, 2022, **6**(9), 248.
[61] A. Cortés, X. F. Sánchez-Romate, A. Jiménez-Suárez, M. Campo, A. Ureña, and S. G. Prolongo, *Polymers*, 2020, **12**(4), 975.
[62] S. Ghoshal, *Fibers*, 2017, **5**(4), 40.
[63] K. Grabowski, P. Zbyrad, and T. Uhl, *Key Engineering Materials*, 2014, **588**, 84-90.
[64] F. Liu, D. Xie, F. Lv, L. Shen, Z. Tian, and J. Zhao, *ACS Applied Nano Materials*, 2023, **6**(6), 4522-4531.
[65] M. Son, K. Raju, J. Lee, J. Jung, S. Jeong, J.-I. Kim, and J. Cho, *Materials*, 2023, **16**(5), 1873.
[66] B. Herren, M. Charara, M. C. Saha, M. C. Altan, and Y. Liu, *Nanomaterials*, 2020, **10**(2), 233.
[67] B. Herren, P. Larson, M. C. Saha, and Y. Liu, *Polymers*, 2019, **11**(7), 1212.
[68] B. Herren, M. C. Saha, M. C. Altan, and Y. Liu, *Composites Part B: Engineering*, 2020, **200**, 108224.
[69] B. Herren, V. Webster, E. Davidson, M. C. Saha, M. C. Altan, and Y. Liu, *Nanomaterials*, 2021, **11**(7), 1740.
[70] G. Gonzalez, A. Chiappone, I. Roppolo, E. Fantino, V. Bertana, F. Perrucci, L. Scaltrito, F. Pirri, and M. Sangermano, *Polymer*, 2017, **109**, 246-253.
[71] H. Eng, S. Maleksaeedi, S. Yu, Y. Y. C. Choong, F. E. Wiria, R. E. Kheng, J. Wei, P.-C. Su, and H. P. Tham, *Rapid Prototyping Journal*, 2017, **23**(1), 129-136.
[72] Q. Mu, L. Wang, C. K. Dunn, X. Kuang, F. Duan, Z. Zhang, H. J. Qi, and T. Wang, *Additive Manufacturing*, 2017, **18**, 74-83.
[73] O. W. Saadi, A. Schiffer, and S. Kumar, *Int J Adv Manuf Technol*, 2023.
[74] X. Chen, H. O. T. Ware, E. Baker, W. Chu, J. Hu, and C. Sun, *Procedia CIRP*, 2017, **65**, 157-162.
[75] S.-C. Tsai, L.-H. Chen, C.-P. Chu, W.-C. Chao, and Y.-C. Liao, *Additive Manufacturing*, 2022, **51**, 102590.
[76] L. Wang, F. Zhang, Y. Liu, S. Du, and J. Leng, *ACS Applied Materials & Interfaces*, 2021, **13**(15), 18110-18119.

[77] E. Bayarsaikhan, J.-H. Lim, S.-H. Shin, K.-H. Park, Y.-B. Park, J.-H. Lee, and J.-E. Kim, *Polymers*, 2021, **13**(8), 1180.
[78] C. Riccio, M. Civera, O. Grimaldo Ruiz, P. Pedullà, M. Rodriguez Reinoso, G. Tommasi, M. Vollaro, V. Burgio, and C. Surace, *Applied Mechanics*, 2021, **2**(4), 942-955.
[79] B. Steyrer, B. Busetti, G. Harakály, R. Liska, and J. Stampfl, *Additive Manufacturing*, 2018, **21**, 209-214.
[80] M. L. Gupta, S. A. Sydlik, J. M. Schnorr, D. J. Woo, S. Osswald, T. M. Swager, and D. Raghavan, *Journal of Polymer Science Part B: Polymer Physics*, 2013, **51**(6), 410-420.
[81] Y. J. Noh, S. Y. Pak, S. H. Hwang, J. Y. Hwang, S. Y. Kim, and J. R. Youn, *Composites Science and Technology*, 2013, **89**, 29-37.
[82] A. Pantano, N. Montinaro, D. Cerniglia, F. Micciulla, S. Bistarelli, A. Cataldo, and S. Bellucci, *Composites Part B: Engineering*, 2019, **163**, 52-58.
[83] B. Arash, Q. Wang, and V. K. Varadan, *Scientific Reports*, 2014, **4**(1), 6479.
[84] M. Tarfaoui, K. Lafdi, and A. El Moumen, *Composites Part B: Engineering*, 2016, **103**, 113-121.
[85] S. H. Park and P. R. Bandaru, *Polymer*, 2010, **51**(22), 5071-5077.
[86] U. Khan, K. Ryan, W. J. Blau, and J. N. Coleman, *Composites Science and Technology*, 2007, **67**(15), 3158-3167.
[87] A. Cortés, A. Cosola, M. Sangermano, M. Campo, S. González Prolongo, C. F. Pirri, A. Jiménez-Suárez, and A. Chiappone, *Advanced Functional Materials*, 2021, **31**(50), 2106774.
[88] J. Xiao, D. Liu, H. Cheng, Y. Jia, S. Zhou, and M. Zu, *Ceramics International*, 2020, **46**(11, Part B), 19393-19400.
[89] M. N. D. Santos, C. V. Opelt, S. H. Pezzin, S. C. Amico, C. E. D. Costa, J. C. Milan, F. H. Lafratta, and L. A. F. Coelho, *Materials Research*, 2012, **16**(2), 367-374.
[90] X. Zhang, D. Lin, Z. Liu, S. Yuan, X. Wang, H. Wang, and J. Wang, *Journal of Alloys and Compounds*, 2021, **886**, 161156.
[91] J. Tong, W. Pan, J. Ma, J. Luo, and R. Liu, *Progress in Organic Coatings*, 2023, **175**, 107366.
[92] L. Xiong, L. L. Kendrick, H. Heusser, J. C. Webb, B. J. Sparks, J. T. Goetz, W. Guo, C. M. Stafford, M. D. Blanton, S. Nazarenko, and D. L. Patton, *ACS Applied Materials & Interfaces*, 2014, **6**(13), 10763-10774.
[93] J. Wang, B. Weng, P. Larson, and Y. Liu, *Surfaces and Interfaces*, 2019, **16**, 188-193.
[94] P. Kardar and R. Amini, *Pigment & Resin Technology*, 2019, **48**(5), 404-408.
[95] W. Zhu, X. Ma, M. Gou, D. Mei, K. Zhang, and S. Chen, *Current Opinion in Biotechnology*, 2016, **40**, 103-112.
[96] J. Zhang, Q. Hu, S. Wang, J. Tao, and M. Gou, *Int J Bioprint*, 2020, **6**(1).
[97] D. K. Patel, A. H. Sakhaei, M. Layani, B. Zhang, Q. Ge, and S. Magdassi, *Advanced Materials*, 2017, **29**(15), 1606000.
[98] X. Kuang, Z. Zhao, K. Chen, D. Fang, G. Kang, and H. J. Qi, *Macromolecular Rapid Communications*, 2018, **39**(7), 1700809.
[99] S. L. Sherman, O. Kadioglu, G. F. Currier, J. P. Kierl, and J. Li, *American Journal of Orthodontics and Dentofacial Orthopedics*, 2020, **157**(3), 422-428.
[100] Anon.
[101] J. Martín-Montal, J. Pernas-Sánchez, and D. Varas, *Polymers*, 2021, **13**(7), 1147.

[102] M. Štaffová, F. Ondreáš, J. Svatík, M. Zbončák, J. Jančář, and P. Lepcio, *Polymer Testing*, 2022, **108**, 107499.
[103] C. S. Ng, A. S. Subramanian, and P.-C. Su, *Additive Manufacturing*, 2022, **59**, 103118.
[104] A. G. Koozekonan, M. R. M. Esmaeilpour, S. Kalantary, A. Karimi, K. Azam, V. A. Moshiran, and F. Golbabaei, *The Journal of The Textile Institute*, 2021, **112**(6), 946-954.
[105] X. Wang, S. Yao, and X. Li, *Chinese Journal of Chemistry*, 2009, **27**(7), 1317-1320.
[106] C.-Y. Chen, P.-W. Cheng, T. Ichibayashi, T.-F. M. Chang, M. Sone, and S. Nishimura, *ACS Applied Nano Materials*, 2023, **6**(6), 4584-4593.
[107] H. Akbari-Aghdam, A. Bagherifard, M. Motififard, J. Parvizi, E. Sheikhbahaei, S. Esmaeili, S. Saber-Samandari, and A. Khandan, *Arch Bone Jt Surg*, 2021, **9**(4), 445-452.
[108] T. Rehbein, A. Lion, M. Johlitz, and A. Constantinescu, *Polymer Testing*, 2020, **83**, 106356.
[109] M. Mahmoudifard and M. Safi, *The Journal of The Textile Institute*, 2012, **103**(8), 893-899.